# Modifications of the chemical and electronic ferroelectric surface structure under water adsorption

Jiale Wang

**THESE DE DOCTORAT DE**
**L'UNIVERSITE PIERRE ET MARIE CURIE**

Spécialité

Physique de la Région Parisienne
(Ecole doctorale 107)

Présentée par

M. Jiale WANG

Pour obtenir le grade de

**DOCTEUR de l'UNIVERSITÉ PIERRE ET MARIE CURIE**

Sujet de la thèse :

# Modifications of the chemical and electronic ferroelectric surface structure under water adsorption

soutenue le 19/09/2013

devant le jury composé de :

M. Nicholas BARRETT Directeur de thèse
M. Bertrand VILQUIN Co-directeur de thèse

M. Andrei KHOLKIN Rapporteurs
M. Mario MAGLIONE Rapporteurs

Mme. Pascale ROY Examinateurs
M. Yves DUMONT Examinateurs
M. William SACKS Examinateurs

# Modifications of the chemical and electronic ferroelectric surface structure under water adsorption

**Jiale Wang**

# Abstract

The main objective of our research is to understand how the ferroelectric polarization affects the chemi/physisorption of water molecules on a ferroelectric surface and how this adsorption may in return affect the chemical and the atomic structure of ferroelectrics and hence the ferroelectric properties.

We present a study of the surface atomic and chemical structure of $TiO_2$-terminated, ferroelectric $BaTiO_3$ (001) epitaxial films on $SrTiO_3$ substrate with different strains, as well as $BaTiO_3$ (001) single crystals, before and after controlled exposure to water. Finally, the surface structures of a $Sr_{0.67}Ba_{0.33}Nb_2O_6$ (001) single crystal are discussed.

The $BaTiO_3$ thin films have a $P^+$ polarization. The initial physisorption of molecular water is enhanced by a high oxygen vacancy surface concentration, creating a more positively charged surface. Quantitative low energy electron diffraction shows that before water adsorption, the polarization discontinuity at the surface reverses the rumpling in the $TiO_2$ termination layer. There are two dissociative adsorption sites, oxygen vacancies and on-top surface Ti. The predominance of dissociative adsorption is confirmed by both X-ray photoelectron spectroscopy and temperature-programed desorption spectroscopy. The on-top $OH^-$-Ti dominates the chemisorption process. After water adsorption, dissociation gives rise to $OH^-$-Ti chemical bonding at 16 to 20% of the surface Ti sites. Adsorbate screening is more efficient than ionic rumpling and switches the ionic rumpling in the $TiO_2$ layer to the same direction as in the bulk $P^+$ state, but the first BaO layer shows polar inversion with respect to the bulk displacements.

The surface of a ferroelectric $BaTiO_3$ (001) single crystal is BaO terminated with a (1 × 1) reconstruction. The rumpling is smaller at the surface than in the bulk, suggesting that both domain ordering and surface structural changes contribute to screening of the polarization. Linear combinations of the X-ray photoelectron diffraction simulations compared with experiment of the surface structure of each polarization state allow determination of the proportion of each domain type. The best agreement with experiment is found for 55% $P^+$, 38% $P^-$, and 7% $P^{in}$.

Low energy electron microscopy was used to directly observe photocarrier and water adsorbate screening effect on a clean, vacuum annealed $BaTiO_3$ (001) surface. Surface potential contrast between $P^+$ and $P^-$ domains is significantly reduced under the ultraviolet illumination by photo-generated carrier screening. Dissociative water adsorption on on-top cation sites is similarly efficient in screening the surface charge. The surface charge dynamics are dominated by drift under ultraviolet illumination and thermal diffusion after the ultraviolet light is switched off. The time constant for screening is longer than that previously measured on unannealed samples in air and suggests that charge dynamics are strongly dependent on the surface chemistry, in particular, on the oxygen vacancy concentration.

Finally, the surface atomic and chemical structures of a $Sr_{0.67}Ba_{0.33}Nb_2O_6$ (001) single crystal are studied. $Sr_{0.67}Ba_{0.33}Nb_2O_6$ has two A-type cation sites, 1/6 of which are voids, regardless of the Sr/Ba stoichiometry. Sharp, well-defined LEED patterns are observed, consisting of the superposition of two surface reconstructions, $(\sqrt{5} \times \sqrt{5})R26.6^\circ$ and $(5\sqrt{2} \times \sqrt{2})R45^\circ$, due to long-range ordering of the alkaline earth metal voids in A1 or A2 sites. The Sr/Ba stoichiometry is determined by high-resolution X-ray photoelectron spectroscopy. The Sr 3d core level has 2 components suggesting two different sites with distinct chemical environments, reflecting the two A-site occupancies.

Although not directly within the scope of the aim of the thesis project, we have also shown that a room-temperature deposited $BaTiO_3$ ultrathin film, subsequently annealed in $O_2$ can produce a quasi-amorphous phase. The absence of long-range order is confirmed by in- and out-of-plane X-ray diffraction as well as Ti 2p photoelectron diffraction. Ferroelectric polarized domains with good retention have been successfully written into the quasi-amorphous film using piezoresponse force microscopy and exhibit a clear polarization versus electric field hysteresis loop. Substrate clamping frustrates volume expansion during annealing leading to a quasi-amorphous film. These results are presented in the appendix.

# Contents

# Glossary

| | |
|---|---|
| $BaTiO_3$ | BTO |
| $SrTiO_3$ | STO |
| $Sr_{1-x}Ba_xNb_2O_6$ | SBN |
| Quasi-amorphous | QA |
| Tetragonal tungsten bronzes | TTBs |
| X-ray photoelectron spectroscopy | XPS |
| X-ray photoelectron diffraction | XPD |
| Low energy electron diffraction | LEED |
| Quantitative low energy electron diffraction | LEED I-V |
| Mirror electron microscopy | MEM |
| low energy electron microscopy | LEEM |
| Scanning probe microscopy | SPM |
| Atomic force microscope | AFM |
| Piezoresponse force microscopy | PFM |
| Molecular beam epitaxy | MBE |
| Temperature-programmed desorption | TPD |
| X-ray diffraction | XRD |

# Chapter 1

# Introduction

## 1.1 Main objective

The main objective of our research is to study how the ferroelectric polarization affects the chemi/physisorption of $H_2O$ molecules on a ferroelectric surface and how this adsorption may in return affect the chemical and the atomic structure of ferroelectrics and hence the ferroelectric properties. In turn, the acquired knowledge is hoped to be useful for a deeper understanding of light enhanced hydrogen production at a ferroelectric surface. Such an understanding may then be used to develop new ferroelectric compounds to promote the water photolysis reaction, by favoring the electron-hole separation and the surface reactivity. The results obtained go far beyond the photocatalysis aspect since they also concern the general behavior of ferroelectric films and of charged surfaces.

We have carried out a systematic study of the atomic, chemical and electronic structure of ferroelectric domains before and after exposure to varying $H_2O$ partial pressures. This thesis concentrates on some special parts of the research, from the molecular beam epitaxy (MBE) growth of thin films, to the different characterization methods such as X-ray photoelectron spectroscopy (XPS), X-ray photoelectron diffraction (XPD), X-ray diffraction (XRD), low energy electron microscopy (LEEM), low energy electron diffraction (LEED), temperature-programed desorption spectroscopy (TPD), Piezoresponse force microscopy (PFM). MBE with full in-situ growth characterization was essential to provide the high quality epitaxial film with good interfaces. Both laboratory and synchrotron light sources have been used for the delicate, spatially resolved electron spectroscopy probes.

## 1.2 Project Surf-FER

The research work of the thesis was carried out in the framework of and funded by a French National Research Agency (ANR) project, Modifications of the chemical and electronic ferroelectric surface structure under water adsorption (Surf-FER), ANR-10-BLAN-1012. Surf-FER brought together 4 major French laboratories, Institut Rayonnement Matière de Saclay (IRAMIS), Institut des Nanotechnologies de Lyon (INL), Institut de Recherches sur la Catalyse et l'Environnement de Lyon (IRCELYON) and Laboratoire Structures, Propriétés, Modélisation des Solides (SPMS), to study the interaction of $H_2O$ with ferroelectric surface. The collaboration of different experts in the project provided successful use of the wide range of experimental techniques.

## 1.3 Thesis outline

Chapter 2 describes the motivation and goal of this thesis. The structures and physical properties of the ferroelectric materials studied in the thesis are also introduced.

Chapter 3 is dedicated to a description of each of different experimental and theoretical tools used in this thesis.

In chapter 4, we have studied the atomic and chemical structure of the surface of a fully strained, ferroelectric $TiO_2$-terminated $BaTiO_3$ (001) epitaxial film on a $SrTiO_3$ substrate after controlled exposure to water. Water undergoes mainly dissociative adsorption on the surface. The Ti on-top site is the dominant site for $OH^-$ chemisorption. One fifth of the surface Ti atoms bind to $OH^-$. The concentration of surface oxygen vacancies acts mainly to favor initial physisorption. Before exposure to water, the outward pointing polarization in the BTO film is stabilized by atomic rumpling in the $TiO_2$ termination layer. After exposure to water, the chemisorbed $OH^-$ species provide the screening, inverting the surface dipole layer and stabilizing the bulk polarization. Molecular adsorption is observed only for high water coverage. The $H_2O$ desorption energy has been measured as a function of in-plane strain.

In chapter 5, the surface of a $BaTiO_3$ (001) single-crystal was studied using synchrotron radiation induced XPD. AFM, XPS and LEED show that the surface is BaO terminated with a (1 × 1) reconstruction. The Ba 4d, Ti 2p and O 1s XPD results were compared with multiple scattering simulations for out of- and in-plane polarizations using a genetic algorithm to determine atomic rumpling and interlayer relaxation. Linear combinations of the XPD simulations of the surface structure determined the proportion of each polarization state at the surface.

In chapter 6, the surface potential contrast between oppositely polarized ferroelectric domains of a $BaTiO_3$ single crystal under ultraviolet (UV) illumination before and after the dissociative adsorption of water is measured using the transition from mirror electron microscopy (MEM) to LEEM. Both photo-generated free charge carriers and dissociative adsorption of water are effective screening mechanisms of the surface polarization charge. We also found that the screening rate is dominated by drift, whereas the relaxation in the absence of UV light is driven by thermal diffusion. Surface chemistry plays an important role in the surface charge dynamics.

Finally, in chapter 7, the surface atomic and chemical structures of a $Sr_{0.67}Ba_{0.33}Nb_2O_6$ (SBN) (001) single crystal are studied using the low energy electron diffraction (LEED) and X-ray photoelectron spectroscopy. SBN has two A-type cation sites, 1/6 of which are voids, regardless of the Sr/Ba stoichiometry. Sharp, well-defined LEED patterns are observed, consisting of the superposition of two surface reconstructions, $(\sqrt{5} \times \sqrt{5})R26.6^\circ$ and $(5\sqrt{2} \times \sqrt{2})R45^\circ$, due to long-range ordering of the alkaline earth metal voids in A1 or A2 sites. The Sr/Ba stoichiometry is determined by high-resolution X-ray photoelectron spectroscopy. The Sr 3d core level has 2 components suggesting two different sites with distinct chemical environments, reflecting the two A-site occupancies.

Although not part of the original thesis project, as defined within the scope of the Surf-FER project. In the course of the growth and characterization of epitaxial $BaTiO_3$ thin films, we discovered the condition required to produce quasi-amorphous $BaTiO_3$. This opens up a new direction for ferroelectric material design no longer limited to crystalline compounds. Until now, the quasi-amorphous phase in $BaTiO_3$, $SrTiO_3$, and $BaZrO_3$ was achieved by pulling a thick film through a

steep temperature gradient. We have shown that a room-temperature deposited ultrathin film, subsequently annealed in $O_2$ can also produce a quasi-amorphous phase, which provides an easier way for potential extensive fabrication and application. This work is presented in the appendix.

# Chapter 2

# Motivations and materials

## 2.1 Context

Energy and environmental issues are nowadays globally important topics. Currently, fossil fuels are the primary energy source, but they are not inexhaustible and produce greenhouse gas emissions to the atmosphere. Renewable energy sources, including hydroelectric, geothermal, tides, etc., are considered as potential alternatives. However, due to their geographical limitation, they only account for a minor percentage of the total present energy production. So we need urgently to construct clean energy systems for a sustainable development. Hydrogen provides an alternative solution because of its ultimate pollution-free property and its potential applications for fuel cells.

Hydrogen would be treated as an alternative energy to the traditional fossil fuels if an appropriate source can be realized.[Esswein2007] The primary hydrogen production method used in industry now is steam reforming of hydrocarbon feedstocks.[Navarro2007, Palo2007, Al-Mazroai2007] In this process, fossil fuels are consumed and $CO_2$ is emitted. Another commercial hydrogen production is primarily via water electrolysis with renewable electrical power source.[Ni2007] The high expense of electrolysis restricts its use to the production of highly pure hydrogen. Therefore, other methods to produce hydrogen from renewable energy sources need to be considered. The huge amount of solar energy falling on the earth's surface every year exceeds our energy consumption, thus solar energy provides an alternative renewable energy that has the capacity to satisfy current energy demands or those predicted for the future. [Cunningham2005] Due to its clean and low-costing advantage, solar hydrogen production has been receiving increased attention because of the environmental and economic benefits. [Kudo2009]

There are several ways for solar hydrogen production.(i) Electrolysis of water using a solar cell, a hydroelectric power generation, etc. (ii) Reforming of the biomass. (iii) Photocatalytic or photoelectrochemical water splitting (artificial photo-synthesis).[Kudo2009] The method of water splitting is the most simple way. For example, if sun light shines at photocatalyst dispersed in a pool of water, then hydrogen is readily obtained. Photocatalyst systems would be advantageous for large-scale application of solar water splitting because of their simplicity. So photocatalytic water splitting is an attractive reaction and may contribute to an ultimate green sustainable chemistry and to the revolution by solving energy and environmental issues.

## 2.2 Photolysis

In photolysis, photon energy is converted to chemical energy accompanied by a positive change in the Gibbs free energy through water splitting as shown in Figure 2-1. This conversion from solar energy to chemical energy is analogous to photosynthesis in green plants, both resulting in an uphill Gibbs free energy change. Therefore, photocatalytic water splitting can also be considered as artificial photosynthesis.[Kudo2009]

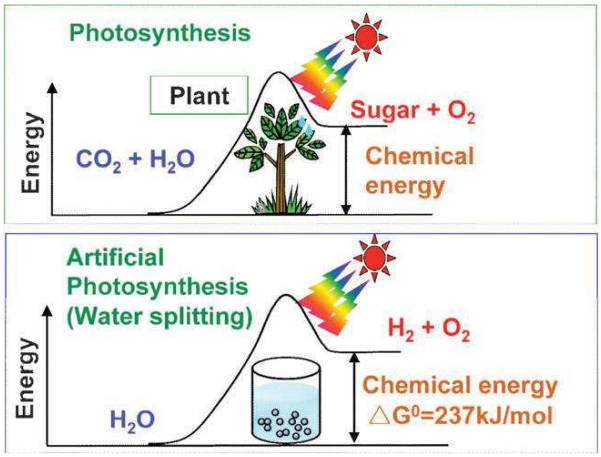


**Figure 2-1.** Photosynthesis by green plants and photocatalytic water splitting as an artificial photosynthesis. (This figure is reproduced from [Kudo2009])

A major breakthrough for solar hydrogen production was made in the early 1970s by Fujishima and Honda.[Fujishima1972] It was observed that hydrogen and oxygen were produced on the surface of Pt and $TiO_2$ electrodes respectively when

ultraviolet light illuminated the $TiO_2$ electrode immersed in an electrolyte aqueous solution as shown in Figure 2-2. When $TiO_2$ was irradiated by photons of energy equivalent to or greater than its band gap, electrons in the valence band were excited to the conduction band, leaving holes in the valence band. These photogenerated electrons and holes can move to the surface of the electrode to participate in redox reactions. The photogenerated electrons reduce water to form $H_2$ on a Pt counter electrode while holes oxidize water to form $O_2$ on the $TiO_2$ electrode with some external bias by a power supply or pH difference between a catholyte and an anolyte.

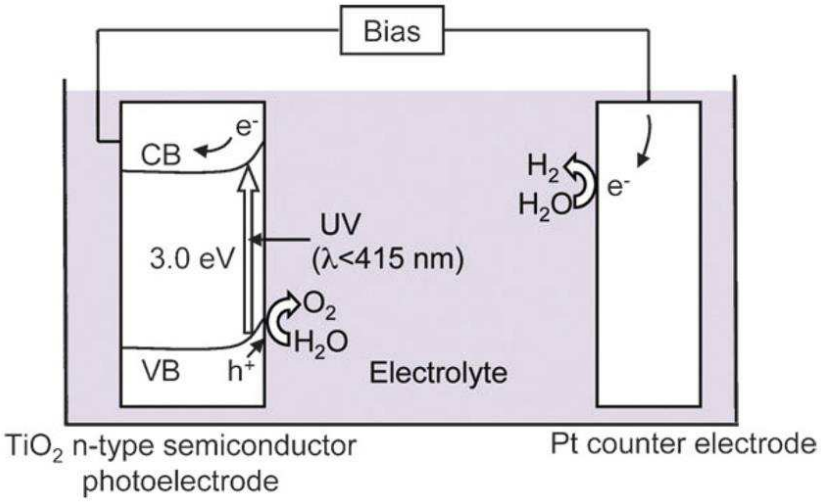


**Figure 2-2.** Honda–Fujishima effect-water splitting using $TiO_2$ and Pt photoelectrode. (This figure is reproduced from [Kudo2009])

In the first step of a photocatalytic reaction, the absorption of a photon creates electron–hole pairs. Since many heterogeneous photocatalysts have semiconductor properties, photocatalytic reactions proceed on semiconductor materials are as schematically shown in Figure 2-3. Semiconductors have a band structure in which the conduction band is separated from the valence band by a energy gap of suitable width. If the energy of incident light is larger than that of a band gap, electrons and holes are generated in the conduction and valence bands, respectively. The photogenerated electrons and holes cause redox reactions similarly to electrolysis. The second step consists of charge separation and migration of photogenerated carriers. Crystal structure, crystallinity and size strongly affect this step. The higher the crystalline quality is, the smaller the amount of defects. This is obvious because

the defects operate as trapping and recombination centers between photogenerated electrons and holes, resulting in a decrease in the photocatalytic activity. The third step is that water molecules are reduced by the electrons to form $H_2$ and are oxidized by the holes to form $O_2$ for overall water splitting.

Photocatalytic water splitting is one of the feasible candidates for hydrogen production due to its simplicity and low cost. Typical ferroelectrics, such as perovskite type oxides can be assimilated to wide band gap semiconductors and many of them are already known to be good photocatalysts. The charged surface state can separate electron-hole pairs more efficiently and it can be renewed under UV illumination, enhancing local photochemical reactions.[Pintilie2001] Therefore, ferroelectrically enhanced dissociation of water could provide a new and efficient mode of hydrogen production, either as non-polluting combustible or in fuel cells.

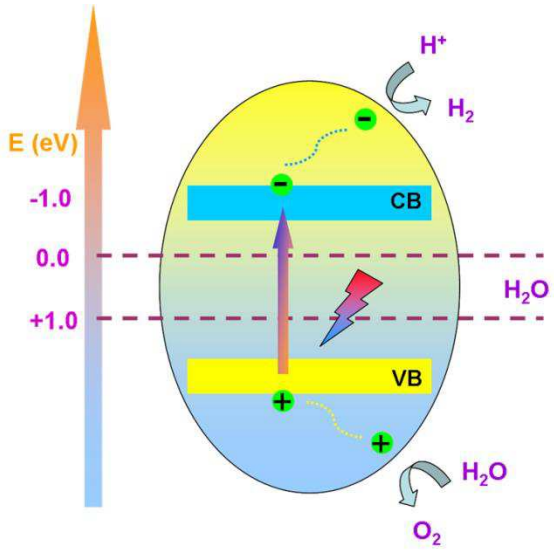


**Figure 2-3.** schematic diagram of photocatalytic water splitting process

At present the efficiency of photocatalysts for water splitting is quite limited. Research for a photocatalyst for pure water splitting under visible light with high quantum efficiency (QE, defined as the ratio between number of produced electron-hole pairs and number of incident photons)[Kudo2009] is under way. The maximum solar energy conversion of water splitting predicted by photoelectrochemical models for a semiconductor with a 2.5 eV band gap is 14 %.[Morrison1980] Now 10 % is the target for commercial application of powdered photocatalysts under visible light.[Osterloh2008] Much work has

focused on photocatalysts, mainly on higher quantum efficiency and less recombination of photogenerated charge carriers. However, it has been shown that the hydrogen yield can be enhanced by over an order of magnitude at the surface of a ferroelectric.[Kim1999, Kim2004] This research provides evidence that the local internal electric fields in ferroelectrics can be used both to separate photogenerated electrons and holes, increasing the e-h pair lifetime, and to control the spatial location of oxidation and reduction processes.

In this thesis, the surface atomic and chemical structures of 2 ferroelectric materials, $BaTiO_3$ (BTO) and $Sr_{1-x}Ba_xNb_2O_6$ (SBN) , have been studied.

## 2.3 A brief introduction to the ferroelectric and structural properties for ferroelectric materials $BaTiO_3$ and $Sr_{1-x}Ba_xNb_2O_6$

### 2.3.1 Ferroelectricity

Ferroelectric material has two or more ground states of different nonzero mesoscopic electric polarization in zero applied electric field, which is referred as spontaneous polarization. Ferroelectrics are non-centrosymmetric with positive and negative charges having different centers of symmetry resulting in a polarized crystal. The polarization vector can be switched between these different orientation states by an applied electric field, which changes the relative energy of the states through the coupling of the field to the polarization.[Rabe2007]

In a ferroelectric (FE) material the polarization induces a surface charge, which creates a depolarizing electric field opposite to the field responsible for the ferroelectric polarization. In some conditions, for example in a thin film, the depolarizing field can be sufficiently strong to reduce or even completely screen the FE state. To minimize the depolarization fields, the direction of the polarization varies from region to region of the crystals. Any region having a locally uniform polarization is called a domain, and the boundary separating two domains is called a domain wall.[Tiwari2009] The size of a domain is determined by minimizing the overall deformation and the electrostatic energies.[Lines1977] Domain walls are often described relative to the angle formed between the polarization vectors on either side of the wall. For example, in tetragonal $BaTiO_3$, where the polarization

directions are along the pseudocubic <100> directions, domain walls can be either 90º or 180º. The 90º and 180º domain walls are shown in Figure 2-4. In this figure, ‘c+’ and ‘c-’ refers to domains with polarization vectors along (+) and (-) z direction (vertical), respectively, while ‘a’ represents domains along the a axis (horizontal). The surface charge may also be partially, fully or in some cases even not at all screened by free charge carriers or defects in the bulk or by external charges from adsorbate species.

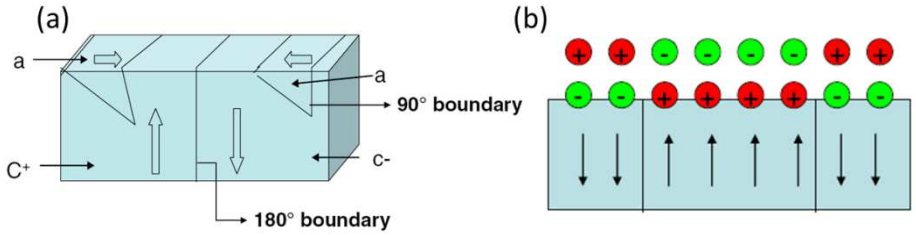


**Figure 2-4.** Schematic of (a) domains in a ferroelectric crystal. (b) Screening of surface charge by the adsorption of polar molecules on a domain structured ferroelectric surface. (This figure is reproduced from reference [Tiwari2009].)

### 2.3.2 Perovskite $BaTiO_3$

Figure 2-5 shows the crystal structure of the different phases of $BaTiO_3$ (BTO) as a function of temperatures. [Kwei1993] At high temperatures (above ~120 °C), the crystal displays a cubic perovskite structure, is centrosymmetric and no spontaneous polarization is observed, it has a paraelectric behaviour. When the temperature is below ~120 °C, but above ~5 °C, the octahedral cages of oxygen distort and the Ti and Ba sublattices are shifted relative to the negatively charged oxygen lattice, which produces the polarization. In the displacive model, the specific shift of atoms (along <100>) leads to a change of crystal structure from cubic to tetragonal. When the temperature is below ~5 °C, the preferred displacement direction of atoms changes (from <100> to <110>) and the structure converts to orthorhombic; below ~ -90 °C it converts to rhombohedral (with <111> displacements). The direction of the relative atomic displacement determines the polarization direction. The critical transformation temperature from ferroelectric to non-ferroelectric is called the Curie temperature (Tc).[Ahn2004] Above the Curie temperature (~120 °C for BTO), it has a centrosymmetric paraelectric cubic

structure with five atoms per unit cell (Pm3m). At lower temperatures, the crystal has three successive FE (non-centrosymmetric) phases.

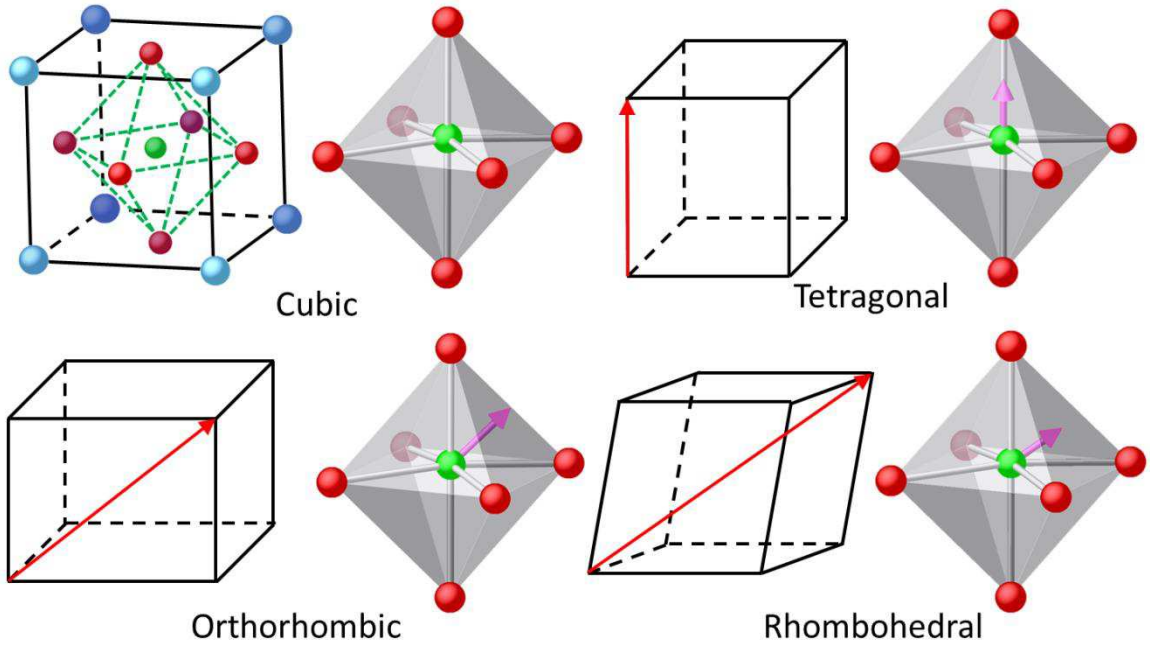


**Figure 2-5.** Schematic of the structure of the different phases of $BaTiO_3$. The Ba ions are located at the corners, the Ti ions at the cell center, and the O ions at the face centers. The deformations in the ferroelectric structures are exaggerated for the sake of clarity.

The room temperature phase is tetragonal with lattice parameters a = 3.996 Å and c = 4.036 Å. In the tetragonal phase there are two FE distortions along the c-axis, parallel and anti-parallel to [001] identified as $P^+$ and $P^-$. The polarization may also be along one of the four equivalent a-axis directions, identified as $P^{in}$, as presented in Figure 2-6. When considering the (001) surface the four in-plane polarizations are equivalent whereas the symmetry breaking due to the surface distinguishes $P^+$ and $P^-$.

As in all $ABO_3$ perovskites, BTO consists of alternating BaO and $TiO_2$ atomic layers along the [001] direction. The ideal BTO(001) surface termination can either be BaO or $TiO_2$. Kolpak et al. [Kolpak2008] investigated the surface phase diagram of BTO as a function of sample preparation and report that after UHV annealing at 700 °C the (1 × 1) surface is mainly BaO terminated. Given the room temperature tetragonal structure, the FE polarization may be out of plane, $P^{\pm}$, with dipole moments pointing exclusively up from or down to the surface along the c-axis or

in-plane along either the a- or b-axes (Figure 2-6). The particular domain ordering is dependent on sample history and can include both 180° (antiparallel) and 90° (top to tail) domain walls.[Merz1954, Forsbergh1949] However, as indicated above, surface rumpling and interplanar relaxation must also be considered for each type of domain for a detailed description of screening.

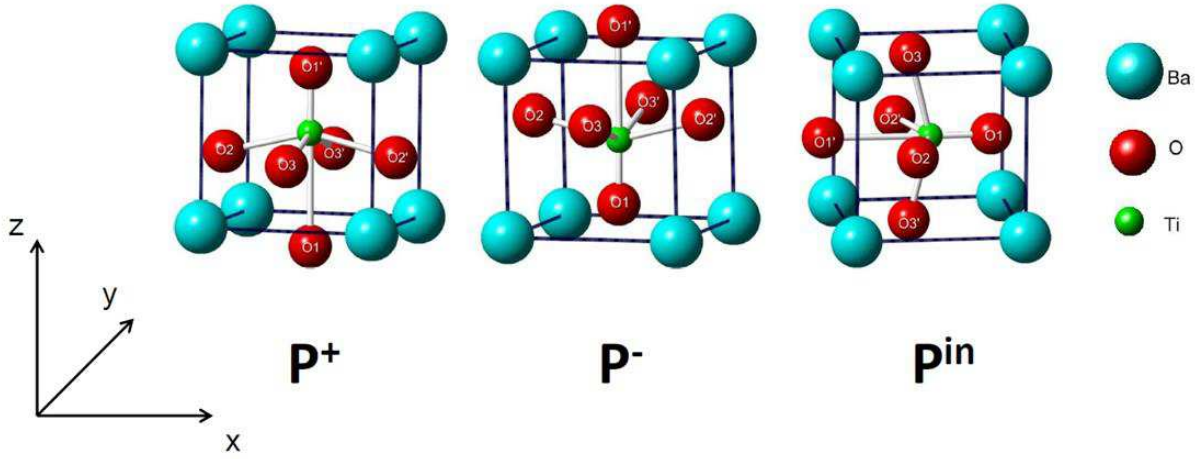


**Figure 2-6.** Schematic of FE distortion following the displacive model in the BTO unit cell for $P^+$, $P^-$ and $P^{in}$ (in this case, $P_x$) polarizations. Displacements are exaggerated for clarity.

BTO belongs to a particular class of oxide surfaces, which can have polar surface in the FE phase. Their specificity comes from the combined effect of orientation and termination which is responsible for the existence of a macroscopic polarization along the surface normal and a surface instability of electrostatic origin.[Goniakowski2008] Polar oxide surfaces are subject to complex stabilization processes that ultimately determine their physical and chemical properties, which can be achieved in many ways: by a deep modification of the surface electronic structure-total or partial filling of surface states, sometimes leading to surface metallization (or by strong changes in the surface stoichiometry) spontaneous desorption of atoms, faceting, large cell reconstructions due to the ordering of surface vacancies, adsorption of foreign species.[Noguera2000, Noguera2004] Special attention should be needed because the ferroelectric and dielectric properties will be strongly influenced by surface effects. For an understanding of the behavior of FE thin films it is therefore important to explore how the FE order couples to the surface.[Meyer2001]

The polar surfaces may also lead to original surface configurations, in which the local environment of the surface atoms is very different from the bulk or from non-polar terminations, and in which peculiar electronic surface states may appear in the gap of the oxide. As a result, surface oxygens and cations may present an enhanced basic or acid character, respectively, with important implications on reactivity.[Finocchi2000]

In relation to polarity, they raise two very new questions. The first one concerns the stabilization of polar nano-objects by the substrate on which they are deposited. The second question is related to the role of electrostatic interactions, which are at the root of polar instability, when going from macroscopic down to the nanometre scale. Actually, as shown below, some nano-systems can sustain a linear component of the electrostatic potential, which never occurs in electrically isolated macroscopic samples. Some polar nano-structures may thus turn out to be stable without depolarization effects from the surface. Others are subject to unusual processes of stabilization that are absent or inefficient in their macroscopic counterparts. Such processes may modify profoundly, and in a size dependent manner, the structural and electronic properties of nano-objects. Thanks to recent advances in the preparation under controlled conditions and to improvements in the experimental techniques for their characterization, it is possible to make high quality BaO and $TiO_2$ terminated BTO nanometric films for further studies. [Schlom2008, Goniakowski2008]

### 2.3.3 Tetragonal tungsten bronzes $Sr_{1-x}Ba_xNb_2O_6$

Ferroelectric strontium barium niobate is expected to be a good water splitting photocatalysts. The ferroelectricity in strontium barium niobate is axial and thus involves only up and down domains. Under UV illumination, the charged surface state can separate electron-hole pairs more efficiently and it can enhance local photochemical reactions. Meanwhile the fairly high energy level of Nb 4d is beneficial for the potential hydrogen production by water splitting.[Chen2009, Kudo2000] Therefore, Strontium barium niobate could provide a new and efficient mode of hydrogen production.

Belonging to the tetragonal tungsten bronzes (TTBs) family, $Sr_{1-x}Ba_xNb_2O_6$ (SBN) is a uniaxial ferroelectric material. It has a spontaneous polarization along c-

axis of TTB structure. [Jamieson1968] The Curie temperature (Tc), dielectric constant, and D-E hysteresis, can be varied by changing the Sr/Ba atomic ratio in the range of $0.25<x<0.75$.[Tanaka1998] For example, the Tc varies from 60 to 250 °C for x values of 0.25 and 0.75, respectively.[Qu2002]

The $Sr_{1-x}Ba_xNb_2O_6$ solid solution is formed in the concentration range of 0.2~0.8 and has an unfilled TTB structure.[Kim2002, Chernaya2000] The SBN unit cell can be described by the general structural formula $[(A1)_2(A2)_4C_4][(B1)_2(B2)_8]O_{30}$. The SBN structure is built up of two types of crystallographically independent $NbO_6$ octahedra joined via oxygen apices into a three-dimensional network. In this network, there are three types of structural channels running along the polar c axis. The narrowest triangle channels (channels C) with 9-coordinate site are empty, the intermediate tetragonal channels A1 with 12-coordinate site are occupied only by the Sr atoms, and the largest pentagonal channels A2 with 15-coordinate site are filled by Ba and Sr atoms.[Chernaya2000, Belous2007] Variation of the [Sr]/[Ba] atomic ratio shifts the temperature of the FE to PE phase transition, changes the permittivity, and modify the relaxor properties of SBN.[Belous2007] Regardless of the [Sr]/[Ba] ratio, 1/6 of the A sites in the SBN structure are empty.

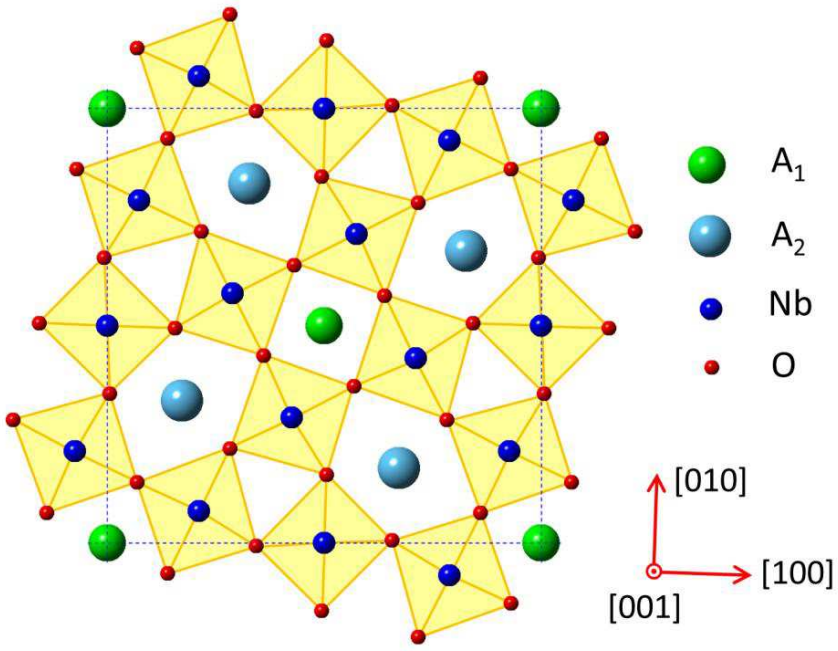


**Figure 2-7.** Crystal structure of the tetragonal tungsten bronze $Sr_{1-x}Ba_xNb_2O_6$

# Chapter 3

# Introduction to experimental methods

## 3.1 X-ray photoelectron spectroscopy (XPS)

The working principle of x-ray photoelectron spectroscopy is based on the photoelectric effect discovered more than one century ago. In the early 1880's, H. Hertz first noticed that the metal contacts in an electrical system exhibit an enhanced ability to spark when exposed to light. In 1899, J. J. Thompson found that electrons could be emitted from a zinc plate exposed to light. This photoelectric effect had puzzled scientists for years until 1905 when Einstein correctly explained these observations by using Planck's concept of energy quantization, i.e., the photons of light transfer their energies directly to the electrons within an atom, resulting in the emission of the electrons from the atom.[Einstein1905]

About half a century after the discovery of the photoelectric effect, Steinhardt and Serfass applied photoelectron emission as an analytical tool in 1951. Throughout 1950's and 1960's, K. Siegbahn and coworkers at the University of Uppsala, Sweden made dramatic improvements in the energy resolution and sensitivity of the electron spectrometer, enabling a determination of the binding energies of electrons for a wide range of materials. As we will see, from an analysis of the electronic binding energies it is possible to build up a chemical "fingerprint" of the solid. Thus it is commonly referred to as electron spectroscopy for chemical analysis (ESCA). The photon source used by K. Siegbahn was X-rays, so the technique is also called the X-ray photoelectron spectroscopy (XPS). Siegbahn's pioneering work earned him the Nobel prize for chemistry in 1981.

XPS is one of the most powerful surface analytical tools. XPS analysis of a surface provides qualitative and quantitative information on almost all the elements in the periodic table (except hydrogen and helium). The photons irradiate a sample, and produce photoelectrons from the surface by energy transfer to the electrons of the surface and near surface atoms. The energy of the photoelectrons leaving the

sample is measured by using an energy analyzer and this gives a spectrum with a series of photoelectron peaks. The core level peak positions can be used to determine the near surface elemental composition while the peak intensities are used to analyze the surface composition in a quantitative manner. The combination provides the basis of surface composition analysis.

The peak shape and the binding energy of a specific element can be altered by the chemical environment of the corresponding atom. Hence XPS can provide chemical bonding information as well. Compared to AES, only one electron energy level needs to be considered in XPS, and the core level peaks are quite narrow reflecting their localized nature, making the XPS more useful to analyze the chemical states of atoms.

### 3.1.1 Process of Photoemission

When a photon of energy hν is incident on a sample, all of the electrons whose binding energy is smaller than hν can be excited from their initial state. Energy transfers the electron, leads to photoemission from the solid within the simple but useful 3-step model.[Hüfner2003]

The first step is the photo-excitation process. The impinging photons excite the electrons in the occupied states, such as the core levels or the valence band, into the empty states above the Fermi level $E_F$ of the solid. These excited electrons are distributed from the surface to the deeper parts in the sample. The second step is the transport process towards the surface. The excited electrons in the inner part of the sample may undergo scattering in their paths towards the surface. Only those electrons which are not inelastically scattered can reach the surface without losing the information they carry on their initial state. The third step is the emission or escape of the excited electrons. Since there is a potential barrier at the surface, which is equal to the energy difference between $E_F$ and the vacuum level $E_0$, called the work function of the solid, only those excited electrons which reach the surface with kinetic energy (KE) larger than the work function can escape from the sample becoming the photoelectrons. Those electrons, which have suffered inelastic scattering and lost energy, will contribute to the secondary electron background if they reach the surface and surmount the surface barrier.[Ding2004]

### 3.1.2 Binding Energy

XPS detects the photoelectrons, which carry the information of the initial electron state in the sample via an energy difference. The kinetic energy of the emitted electrons is expressed by the Einstein equation:

$$E_k = h\nu - E_B - \phi_s$$

where $E_B$ is the binding energy of an electron in its initial state in the atom, $h\nu$ is the energy of the x-ray photon, $E_k$ is the kinetic energy of the emitted electron, and $\phi_s$ is the work function of the sample.

In practical XPS, electron kinetic energy is measured with respect to the work function of the spectrometer, which might be different from that of the sample. Therefore, the equation can be written as

$$E_k = h\nu - E_B - \phi_{sp}$$

where $\Phi_{sp}$ is the work function of the instrument. Actually, for convenience commercial equipment has usually already calibrated the kinetic energy of the photoelectron relative to the Fermi level, which is set to the same value for both the spectrometer and the sample under the equilibrium. Therefore a simple relation holds for the binding energy of the core level and its corresponding kinetic energy of photoelectron:

$$E_k = h\nu - E_B$$

Thus, from the known $h\nu$ and the measured $E_k$, the binding energy of the element $E_B$ is easily obtained.

The core-level binding energy is representative of the atomic species. XPS thus provides a chemical "fingerprint" of the surface and near-surface region. Although the binding energy will vary depending on the chemical environment of the atom in the solid, these energy differences are generally small enough so that the presence of a particular element may be unequivocally identified from an XPS spectrum.

The photoemission process is represented schematically in Figure 3-1. To know the electronic and chemical structure of a material one has to deduce the initial state of the electron (left side of Figure 3-1) from the measured photoemission spectrum

(right side of Figure 3-1). In the solid, electrons occupy discrete, localized states (core levels) or more delocalized states (valence band, and for metals, the conduction band). The binding energy is specific to the emitting atom and is therefore a sensitive signature of the local chemical and electronic environment. The valence electrons are responsible for the electronic structure and reflect the insulating, semiconducting or metallic nature of the material. It is also the valence electrons, and for conducting samples, the states at the Fermi level, which determine many key properties for technological applications, such as electron transport, magnetization, spin polarization, or electron-electron correlation. Thus, from a photoelectron spectrum, knowledge of the work function $\phi$ ($\phi = E_F - E_0$, where $E_F$ is the Fermi level and $E_0$ the vacuum level) and the photon energy allows deduction of the initial states of the analyzed electrons. From the beginning of the 1950s,[Nordling1957] XPS has evolved into a standard technique for acquiring elemental, chemical and electronic information of surfaces.[Hüfner2005, Briggs2003]

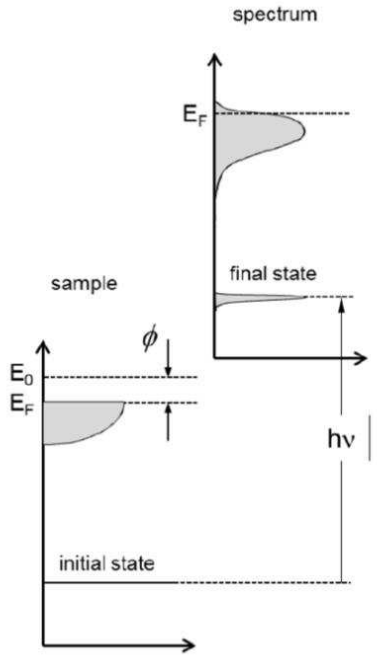


**Figure 3-1.** Schematic energy levels in a photoemission experiment. The initial state (left) is excited by a photon hν, giving the final state as measured by the spectrometer (right). The work function, $\phi$, is the difference between the local vacuum level and the sample Fermi energy, $E_0$ - $E_F$. (This figure is reproduced from reference[Barrett2013].)

### 3.1.3 Quantitative analysis

For a sample that is homogenous in the analysis volume, the intensity of a XPS peak $\alpha$ can be written as:

$$I_\alpha = Af N_\alpha \sigma_\alpha \gamma \lambda \theta TD$$

where A is the detection area, $f$ is the x-ray photon flux, $N_\alpha$ is the number of atom per $cm^3$, $\sigma_\alpha$ is the photo-ionized cross section of the corresponding core level, $\gamma$ is the efficiency of photoemission process, $\lambda$ is the inelastic mean free path, $\theta$ is the accept solid angle of the analyzer, T is the transmission of analyzer, and D is the efficiency of detector.[Briggs1996] In principle, the atomic concentration $N_\alpha$ can be determined by measuring the peak intensity $I_{\alpha.}$ As in the case of quantitative analysis by AES, the atomic sensitivity factor method is also commonly used in XPS. Defining the relative atomic sensitivity factor S as:

$$S = \sigma_\alpha \gamma \lambda T$$

the parameters A, $f$, $\theta$, D are the same for all the elements in the sample, the atomic percentages for an unknown element can be calculated as:

$$n_x = \frac{I_x / S_x}{\sum_i I_i / S_i}$$

In principle, the relative atomic sensitivity factors can be determined using the known values of $\sigma_\alpha$, $\gamma$, $\lambda$, and T. But in practice, similar to the case of AES, the values of relative atomic sensitivity factors are determined by measuring the XPS peak intensities of a series of pure elements under the same experimental conditions, and their sensitivity factors are derived with respect to that of the F 1s peak. Then one can find them in the instrument handbook as well. However, care must be taken because the listings are valid only for the specific instrument because the relative atomic sensitivity factors change with energy of incident X-rays[NIST].

XPS is surface sensitive because photoelectrons may be inelastically scattered as they escape across the surface and to be detected by the spectrometer [Corcoran2010, owell2009]. Thus photoelectrons that are created at or near the

surface will have a smaller probability of undergoing inelastic collisions before they exit the material while electrons that are created deep within the material have a much greater probability of being scattered. The important parameter to determine the depth that is detected by XPS is the inelastic mean free path (IMFP), which is the distance where 1/e of the electrons have undergone an inelastic collision [Tanuma2005].

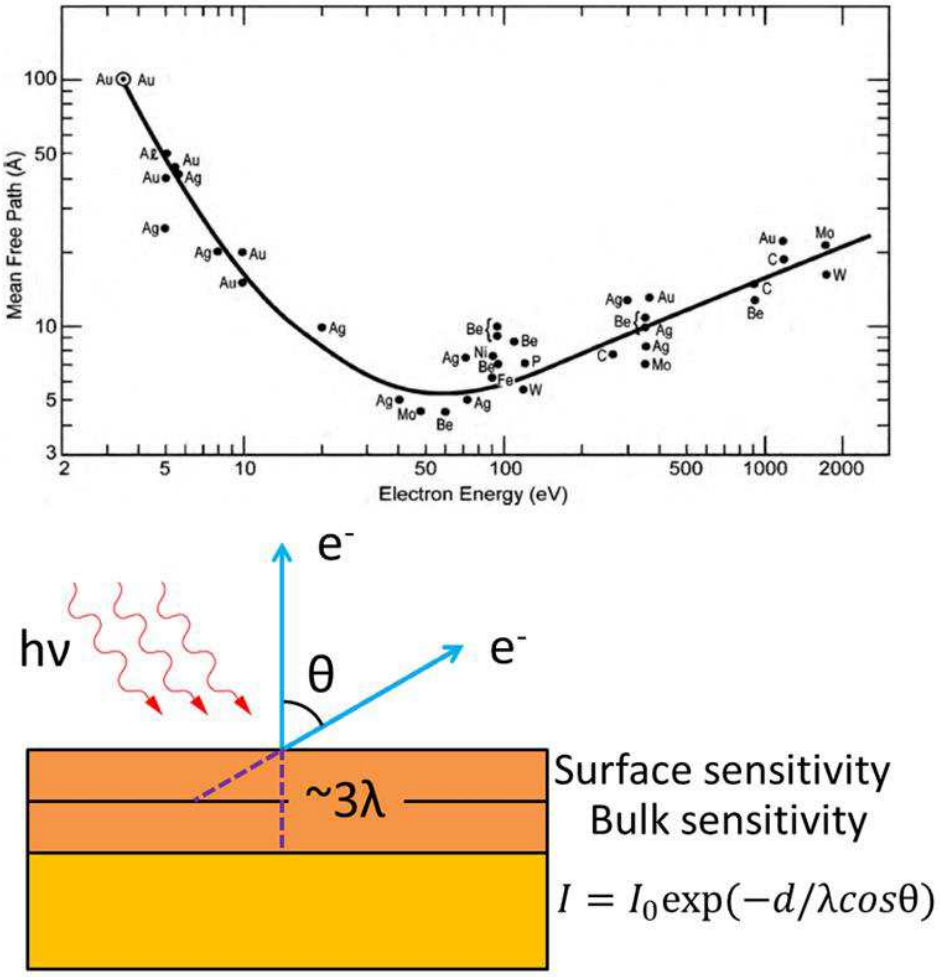


**Figure 3-2.** (top) The mean free path of electrons in different solids as a function of the kinetic energy of the electrons. (bottom) Schematic of angle-resolved photoelectron spectroscopy. (These figures are reproduced from reference [Corcoran2010] and [Brundle1975], respectively.)

The empirical curve of IMFP as a function of the electron energy for several different metals are presented in Figure 3-2, which shows that the mean free path is not strongly dependent on the material, but that it is strongly dependent on the electron energy, and with the shortest IMFP of ~5Å at ~50-100 eV electron energy.

[Corcoran2010] Thus, it is possible to optimize the surface sensitivity of a measurement by using photon energies of 50-100 eV above the BE of a given core-level [Nyholm1991]; however, this tuning requires the use of synchrotron radiation. Further, to probe more of the surface in XPS experiments, one may vary the angle with respect to the surface at which the electrons are detected; electrons exiting along the surface normal may come from a deeper distance within the bulk, while electrons at grazing emission angles come mostly from the upper surface layers [Fadley1984].

### 3.1.4 Electron energy analyzer

The most common type of energy analyzer used for XPS measurements is the electrostatic hemispherical analyzer.[Kevan1980] Two hemispheres of radii R1 (inner) and R2 (outer) are positioned concentrically, as shown in Figure 3-3. Voltages $V_1$ and $V_2$ are applied to the inner and outer spheres, respectively, with $V_2$ lower than $V_1$ (usually $V_1$ is positive or zero and $V_2$ is negative), so the electrons repulsed by the outer sphere moving along on an average, dually elliptical trajectory. The potential at the midpoint of two radii $(R_1+R_2)/2$ corresponds to the pass energy $E_0$. The analyzer possesses slits at the entrance and exit with widths of $W_1$ and $W_2$, respectively. Before entering the analyzer, the photoelectrons are collected by a lens system. The whole analyzer is shielded by a mu-metal screen to prevent the influence of the stray electric and magnetic fields on the electron trajectories. The pass energy $\Delta V$ is given by

$$e\Delta V = E(\frac{R_2}{R_1} - \frac{R_1}{R_2})$$

Mostly, XPS measurements are done in the constant pass energy mode. Electrons entering the entrance slit with their energy equal to the pass energy $E_0$ can be focused at the exit slit. A variable retarding voltage is applied on the analyzer to change the energy of selected photoelectrons to the pass energy. By scanning the retarding voltage, photoelectrons with different kinetic energies are collected and displayed in a spectrum. Actually, the analyzer collects the electrons entering the slit with a divergence of their paths from the ideal tangential path in a solid angle $\delta_\alpha$. If two slits are with width $W_1$ and $W_2$, the energy resolution of the analyzer is

$$\frac{\Delta E}{E_0} = \frac{W_1 + W_2}{2R_0} + (\delta_\alpha)^2$$

which is a constant for a given analyzer. The resolution of a spectrum is determined by the bandwidth of the X-ray source, the temperature and the analyzer. If $E_0$ is fixed (constant analyzer energy), ΔE will be fixed too, and the broadening of the measured peak widths at different energies will be the same. Thus the lower the pass energy, the smaller the ΔE. However, the signal intensity will also decrease at smaller pass energies.[Ding2004]

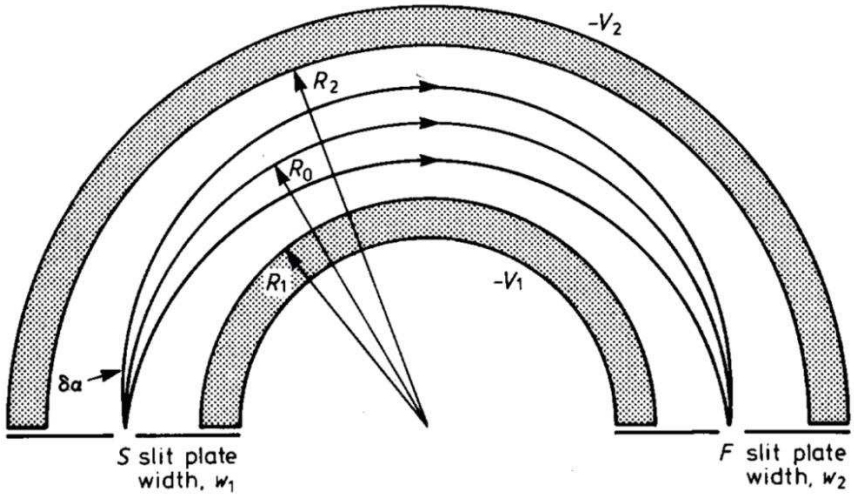


**Figure 3-3.** Schematic of electrostatic hemispherical analyzer. (This figure is reproduced from reference [Ding2004].)

Two analyzers were used in this thesis, one in our laboratory and the other one in the Soleil Synchrotron, respectively. In our laboratory, XPS was carried out using an Omicron EA125 hemispherical analyzer with a 128-channel Argus strip anode detector and a monochromatic Al Kα (1486.7 eV) X-ray source (Omicron Nanotechnology). The analyzer pass energy of 20 eV gave an overall energy resolution (photons and spectrometer) of 0.35 eV. A 128 channel stripe anode detector provides parallel detection. Detector channels at the exit of the hemisphere are orientated along the dispersive plane so that they record 128 different energies in parallel while integrating incoming signal along the non-dispersive plane. As a result, "Snapshot" mode of the analyzer offers outstanding sensitivity, simplified handling and maximum convenience during operation.

At the Antares beamline of Synchrotron Soleil, an electro-static VG Scienta EW4000 hemispherical analyzer was used allowing simultaneous detection of emitted electrons over a wide angular range without tilting of the sample. The VG Scienta EW4000 analyzer uses a new extreme wide angle lens technology, which can provide parallel angular detection. So data in a large polar angle range can be acquired at the same time without turning the sample. It gives great convenience for XPD experiments not only in acquisition speed but also by reducing the risk of surface contamination for long exposure times.

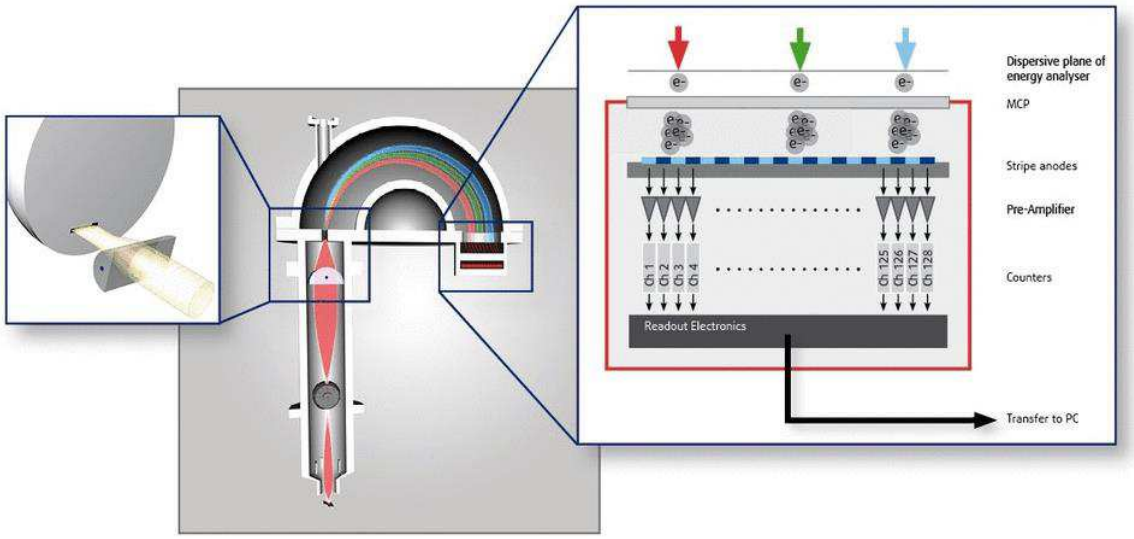


**Figure 3-4.** Detector scheme of Omicron EA125 analyzer: each electron impact starts a cascade of electrons propagating through the MCP stack. (This figure is reproduced from reference [Omicron].)

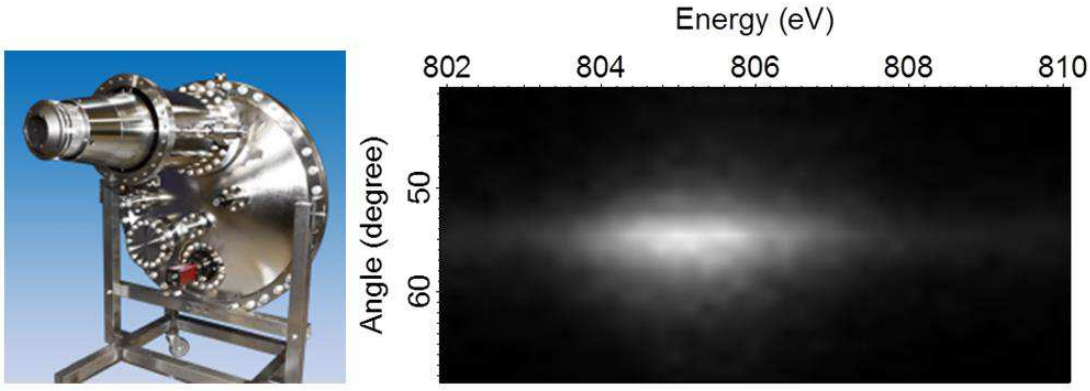


**Figure 3-5.** Photographs of VG Scienta EW4000 analyzer and its wide range swept mode measurement of Ba 4d core level.

## 3.2 X-ray photoelectron diffraction (XPD)

### 3.2.1 XPD experiment

X-ray photoelectron diffraction (XPD) is used for surface structure determination on the atomic scale.[Fadley1995] This local diffraction technique probes short-range order around the emitting atom. A broad variety of surfaces have been successfully studied, including metals, semiconductors, oxides, systems exhibiting surface core-level shifts, adsorbed atoms and molecules, epitaxial overlayers, and atoms at buried interfaces. A number of research groups have performed photoelectron diffraction experiments to study surface and interface structures, using both laboratory x-ray and synchrotron radiation sources, and doing the measurements in both scanned-angle and scanned energy modes. [Fadley1993, Fadley1994, Bonzel1993, Shirley1994, Osterwalder1995]

In XPD, the angular dependence of the collected electron intensity originates from the interference of the directly emitted photoelectron wave and the scattered electron waves. XPD is sensitive on an atomic scale; it can be used to analyze local atomic structure down to the monolayer and surface relaxation. At high kinetic energy, electron undergoes forward scattering, the process can be adequately described by the plane wave approximation; while at low kinetic energy, electron undergoes multiple scattering, the process should be described by spherical wave approximation.

The sample is mounted on a high precision manipulator with polar and azimuthal rotations. To determine the surface structure, the XPD anisotropy of the elemental emission is measured over a wide range of polar and azimuthal angles with a typical angular resolution of 1°. For each ($\theta$, $\phi$) point both the core level and the background intensities are recorded. The intensities of the photoelectron peak versus direction are plotted and show strong diffraction effects. The crystal is rotated around the surface normal, changing the azimuthal angle $\phi$ for a given polar angle $\theta$, the polar angle is then incremented, and the azimuthal scan repeated with the appropriate $\phi$ step. Thus the two-dimensional diffraction maps are measured by concatenating the different azimuthal scans. As $\theta$ is reduced toward normal emission, the $\phi$ step is adjusted in order to give uniform solid angle sampling density above the sample surface.[Mitchell2000] The raw data of the Sr 3d XPD

from a $SrTiO_3$(001) single crystal are shown in Figure 3-6(c) where the angular coordinates are projected using the following transformations: $x=2\tan(\theta/2)\cos\phi$ and $y=2\tan(\theta/2)\sin\phi$. The positions of the high-density crystal planes and axes are indicated in Figure 3-6(d). The <100>-, <110>-, and <111>- like directions are visible in the experimental data, as are structures corresponding to the {111} set of planes. The full ($\theta$, $\phi$) space can be explored.[Pancotti2009]

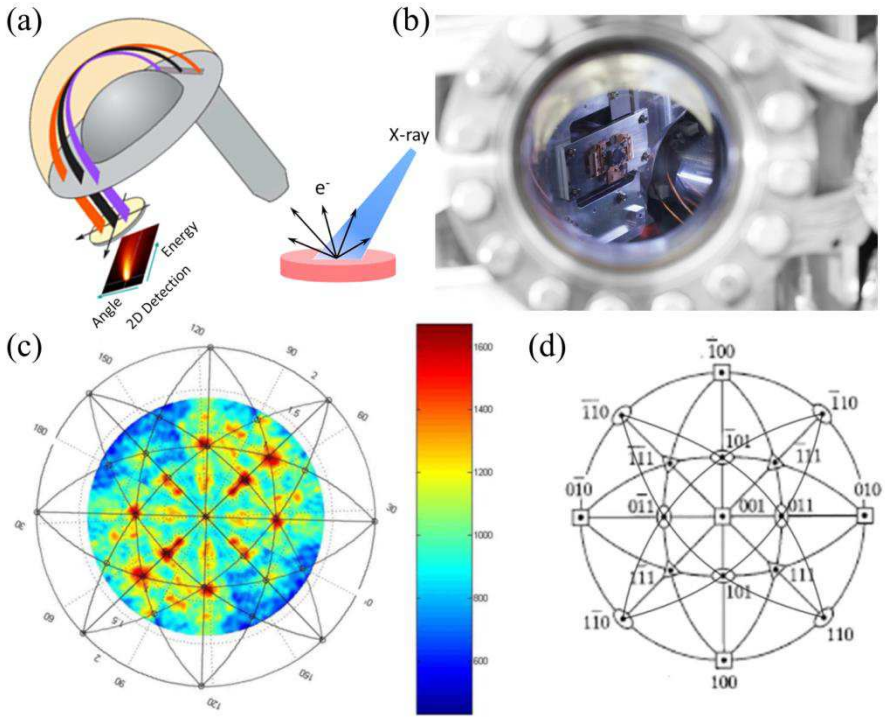


**Figure 3-6.** (a) Schematic diagram of XPD. (b) XPD chamber at the ANTARES beamline, Soleil. (c) Experimental photoelectron intensity map of $SrTiO_3$, showing 4-fold symmetry. (d) Location of high-density crystal axes and planes in the projection of (c) (Figure (c) and (d) are reproduced from [Pancotti2009])

### 3.2.2 Multiple scattering simulations

Quantitative information may be obtained using electron scattering simulations, however, when compared to experimental results, the "forward focusing" intensity is overemphasized in single scattering calculations. Scattering at the first few atoms along a row of atoms focuses the emission in the emitter-scatterer direction, but subsequent atoms tend to defocus the signal. The defocusing is linked to the development of the conventional Kikuchi bands which become more intense when

the forward-scattering peak intensity diminishes. The large number of elastic scattering events make it is necessary to use multiple scattering calculations (MSCs).[Chen1998] In all calculations, we used six multiple scattering events and expansions up to the fourth order Rehr–Albers. [Chen1998]

In an XPD experiment, the emitting atom core-level is the source of photoelectron within the material. The amplitude of the electronic wave emitted is proportional to 1/r, where r is the distance from the emitting atom. The mean free path of photoelectrons is a determining factor in the survey of photoelectron diffraction. These two factors explain why the photoelectron diffraction is sensitive to local structure. According to the different energy of the emitted photoelectron, it can provide information from different depth. Meanwhile, the short-range order must also be uniform over the volume analyzed by the experiment.

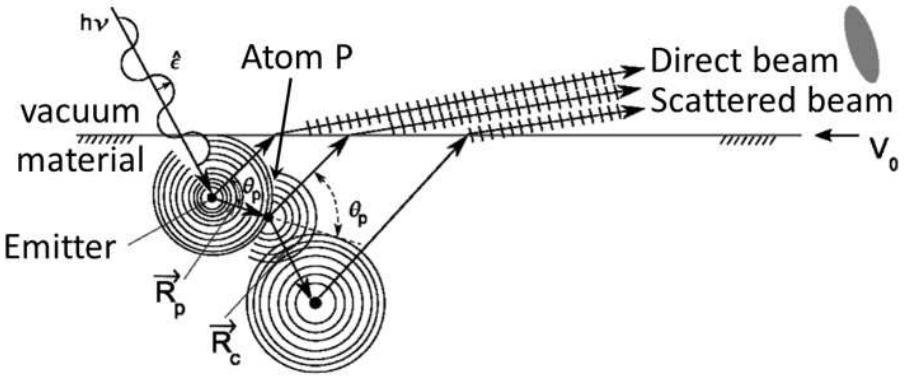


**Figure 3-7.** Illustration of the basic processes involved in photoelectron diffraction, for going straight to the electron detector and through other possible paths.[PancottiA2009]

Figure 3-7 shows a schematic of the process of photoelectron diffraction. When a core level electron is excited by an X-ray photon, it propagates as a spherical wave around the emitting atom and can go straight to the detector or be elastically scattered by the coulomb potential of neighboring atoms, where we now have a secondary wave, from the neighboring atom. The waves arriving directly from the emitting atom and elastically scattered from neighboring atoms, propagate and interfere at the detector outside the sample. These waves have the same wavelength, but due to the scattering processes, have different phase. Intensity variations due to their interference pattern are recorded as a function of the emission angle and/or as

a function of the kinetic energy of the electron. This interference pattern can be generated by a single or multiple scattering, and both differ much from one another.

The photoemission intensity I(**k**) at the detector can be written in general as

$$\mathrm{I}(\mathbf{k}) \propto |\Psi(\boldsymbol{k})|^2$$

Where k is the wave vector of the electron observed. The final wave function Ψ(**k**) is a sum of direct emitted waves and the waves scattered by surrounding atoms, where the contributions due to multiple scatterings are also contained in the final wave function:

$$\mathrm{I}(\mathbf{k}) \propto \left|\Psi_0(\boldsymbol{k}) + \sum_l \Psi_l(\boldsymbol{k})\right|^2$$

$\Psi_0$(k) denotes the direct wave component propagating along a path directly to the detector without being scattered by another atom, and $\Psi_l$(k) is the wave component representing travel via paths involving single or multiple elastic scattering by one or more atoms. The multiple-scattering order is defined as the number of scattering atoms in a path: j=1 is single, 2 is double, etc. Higher-order scattering processes are less important because of the roughly 1/r fall off of the outgoing distorted spherical wave represented by $\Psi_0$, damping and due to inelastic processes and loss of diffraction modulation due to thermal vibrations (Debye-Waller effects).[Chen1998] The explicit sum in this equation includes all possible scattering paths inside the solid. After developing, the intensity equation can be written as:

$$\mathrm{I}(\mathbf{k}) \propto |\Psi_0(\boldsymbol{k})|^2 + \sum_l \left(\Psi_0^*(\boldsymbol{k})\Psi_l(\boldsymbol{k}) + \Psi_0(\boldsymbol{k})\Psi_l^*(\boldsymbol{k})\right) + \sum_l \sum_m \Psi_l(\boldsymbol{k})\Psi_m^*(\boldsymbol{k})$$

Where the amplitude of the final state in the detector is described, and the selection rules are implicitly contained. The second term in the above equation with the subscript of 'l' describes interference between the direct wave $\Psi_0$(k) and the scattered wave $\Psi_l$(k) by a neighboring atom.

The effect of the mean free path of photoelectrons is introduced by a damping factor on $\Psi_l$(k). The mean free path can be found from theory and certain types of experiments. Tanuma, Powell and Penn[Tanuma2011] developed an empirical

formula to calculate the mean free path in the valid range from 50 to 2000 eV, which is given by:

$$\lambda = \frac{E}{E_P^2[\beta \log(\gamma E) - \frac{C}{E} + \frac{D}{E^2}]}$$

Where $\lambda$ is the mean free path in Å, E is the electron energy in eV, $E_P = 28.821 (N_v\rho/M)^{1/2}$ is the plasmon energy of the free electron (eV), $N_v$ is the number of valence electrons of atom, M is the atomic or molecular mass, and B, $\gamma$, C and D are given by:

$\beta = -0.10 + 0.994/(E_P^2 + E_g^2)^{0.5} + 0.069\rho^{0.1}$

$\gamma = 0.191\rho^{-0.5}$

$C = 1.97 - 0.91E_P^2/829.4$

$D = 53.4 - 20.8E_P^2/829.4$

Where $E_g$ is the energy gap of the material (eV), and ρ is the bulk density ($g/cm^3$).

Another factor that contributes to dampen the intensity of diffraction signal is the thermal vibrations of the atoms, which is introduced by the Debye-Waller factor [Yoo2003], $W_l$, which is expressed by:

$$W_l = \exp[-k^2(1 - cos\beta)\sigma_c^2]$$

In the above equation $\sigma_c^2$ is the mean square displacement atom[Hirata1994]:

$$\sigma_c^2 = \frac{9(h/2\pi)^2}{M_s k_B \Theta_D}[\frac{1}{4} + (\frac{T}{\Theta_D})^2 \int_0^{\Theta_D/T} \frac{xe^x}{e^x - 1} dx]$$

Where $M_S$ is the average atomic mass, $k_B$ is the Boltzmann constant, $\Theta_D$ is the Debye temperature, and T is the sample temperature in Kelvin, respectively. $x=h\omega/2\pi k_B T$, with ω being the vibrational frequency.[Ouyang2010]

If the distance between the emitting atom and the scattering center is large compared to the wavelength we can use plane wave theory. We assume the

wavefront at the scattering atom can be described as a plane wave, and write the interference term as[81]:

$$\Psi_m^*(\boldsymbol{k})\Psi_l(\boldsymbol{k}) = e^{+i\boldsymbol{k}\cdot\boldsymbol{r}_m}e^{-i\boldsymbol{k}\cdot\boldsymbol{r}_l} = e^{-i|\boldsymbol{k}||\boldsymbol{R}_P|cos\theta_P}$$

where **k** is the wave vector of the electron and this varies with the photon energy incident on the sample, $\mathbf{r}_m$ and $\mathbf{r}_l$ are the position vectors of the direct wave and scattering wave suffered once and $\theta_P$ is the angle between these two vectors.

In order to compare the simulations directly with the experimental data, the XPD intensities are presented in the form of anisotropy maps. The anisotropy $\chi$ is defined as

$$\chi = \frac{\mathrm{I}\left(\theta, \phi, \vec{k}\right) - \mathrm{I}_0(\theta, \phi, \vec{k})}{\mathrm{I}_0(\theta, \phi, \vec{k})}$$

where $\mathrm{I}(\theta, \phi, \vec{k})$is the measured or calculated photoemission intensity and $\mathrm{I}_0(\theta, \phi, \vec{k})$ is the photoelectron intensity in the absence of diffraction free atom.

As a further measure of the quality of the analysis beyond the numerical value of the R-factor, uncertainties can be estimated using the steepness of the R-factor space assigned to a parameter in the vicinity of its absolute minimum and the maximum number of separable diffraction information N with an experimental data set,

$$Var(R_{min}) = R_{min}\sqrt{2/N}$$

where $\mathrm{Var}(R_{min})$ denotes the variance of R at its minimum. This procedure was introduced by Pendry[Pendry1980] for quantitative LEED analysis and was adapted to XPD.[Bondino2002] A study of the uncertainties in this context has been done by Van Hove et al.[VanHove1993]

### 3.2.3 Genetic algorithm global optimization method

Structural determination by XPD requires a fitting procedure between the experimental intensities and theoretical results obtained through simulations. Multiple scattering has been shown to be an effective approach for making such simulations. The quality of the fit can be quantified through the R-factor. Therefore,

the fitting procedure is, indeed, an R-factor minimization problem. However, the topography of the R-factor as a function of the structural and non-structural surface parameters to be determined is complex, and the task of finding the global minimum becomes tough, particularly for complex structures in which many parameters have to be adjusted. The genetic algorithm (GA) global optimization method is a good solution to this problem, which is based on the evolution of species, and makes use of concepts such as crossover, elitism and mutation to perform the search.[Viana2007]

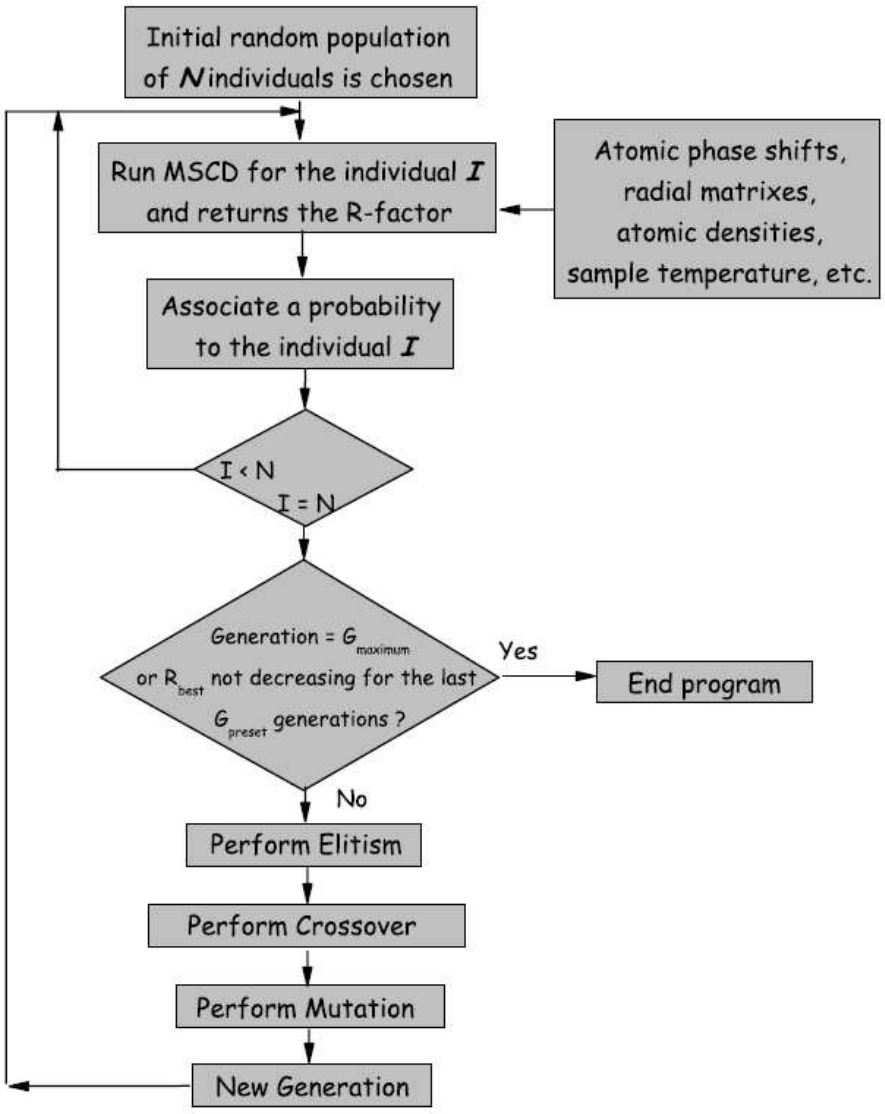


**Figure 3-8.** Schematic flow chart of the genetic algorithm implemented for photoelectron diffraction structural determination using the MSCD code. (This figure is reproduced from reference [Viana2007].)

Many optimization methods are based on some form of 'steepest descent' [Scales1992]: they typically start from a unique trial solution, and use function derivatives to decide on the search direction. Numerical algorithms of this type usually converge to the nearest local minimum, and there is no guarantee that the reached minimum is the global minimum of the function. By contrast, a GA works with populations of solutions, starting the search from many different trial solutions, comparing their function values and then generating new trial solutions that may exist in very different parts of parameter space. Thus, it is able to roam throughout parameter space and look for the global minimum.

A given surface structure is defined by a set of particular parameters and is treated as an individual. The implementation of the GA method for the photoelectron diffraction problem in the MSCD code follows the general steps described below to determine the structural and non-structural surface parameters, and is illustrated by the flow diagram in Figure 3-8.[Viana2007]

(i) An initial population of N individuals is chosen (N is an even number). Each individual is a vector containing the P parameters to be optimized in the surface analysis of the system. The value of each parameter is randomly chosen within a physically acceptable range for that system. Each individual is coded and its binary or real string contains the displacements to be added to the parameters of a reference initial surface structure.

(ii) The MSCD code calculates the theoretical photoelectron intensity curves for one individual, which we call individual I. It starts from general information available about the system, such as atomic phase shifts, radial matrices for the emitter atoms, atomic densities, sample temperature, etc., but modifies the coordinates according to the displacements related to individual I. It makes the comparison to the experimental curves, and returns the R-factor value associated to individual I.

(iii) The probability of being selected for crossover is calculated based on the R-factor of the individual. An individual with a lower R-factor has a higher chance to be selected for the crossover process.

(iv) The steps (ii), and (iii) are repeated for all other individuals in the population.

(v) The search stops here if the best R-factor has not decreased after a preset number of generations or if a preset maximum number of generations is reached: the best individual in the last generation is selected as the best solution. Otherwise, the best individual is cloned to the next generation (by elitism) and the process continues.

(vi) N/2 pairs of individuals are chosen according to probabilities based on their R-factors obtained in step (iii). The crossover process then creates N new individuals for the next generation. The worst one is discarded, being replaced by the clone obtained in the previous step.

(vii) A number between 0 and 1 is chosen randomly. If this number is smaller than a previously chosen mutation rate, then a randomly chosen individual is subjected to the mutation process.

(viii) The new generation is ready, and the process restarts at step (ii) for the new generation.

For complex surface structures, in which many structural parameters are needed to describe the complete surface structure global optimization methods are useful to fit the theoretical to the experimental curves and in the determination of surface structures from photoelectron diffraction experimental data.

## 3.3 Quantitative low energy electron diffraction (LEED I-V)

### 3.3.1 LEED principle

The ordered array of atoms in the crystal makes the crystal act as a grating. Long range atomic order at the surface can be detected low energy electron diffraction (LEED). LEED with wavelength shorter than the lattice constant and penetration depth in the range of several Å, can be used as a quantitative means of surface structure determination.

According to the de Broglie relation, the wavelength of the electrons is given by:

$\lambda = h / p,$

where h is the Planck's constant, and p is the electron momentum. When the electrons are accelerated by a voltage V, the kinetic energy of electrons is eV, and the electron momentum can be expressed by

$$p = (2\ m\ e\ V)^{1/2},$$

where e is the electron charge, and m is the mass of electron. Thus the electron wavelength is determined by:

$$\lambda = h / (2\ m\ e\ V)^{1/2} = 12.4/V^{1/2}.$$

the unit of V is volt, and is in Å. Accordingly the wavelength of electron in the energy range of 10 ~ 500 eV is 0.4 ~ 0.05 nm, which is comparable with the atomic spacing. So the low energy electron beam interacting with the ordered surface atomic structures can create diffraction patterns.

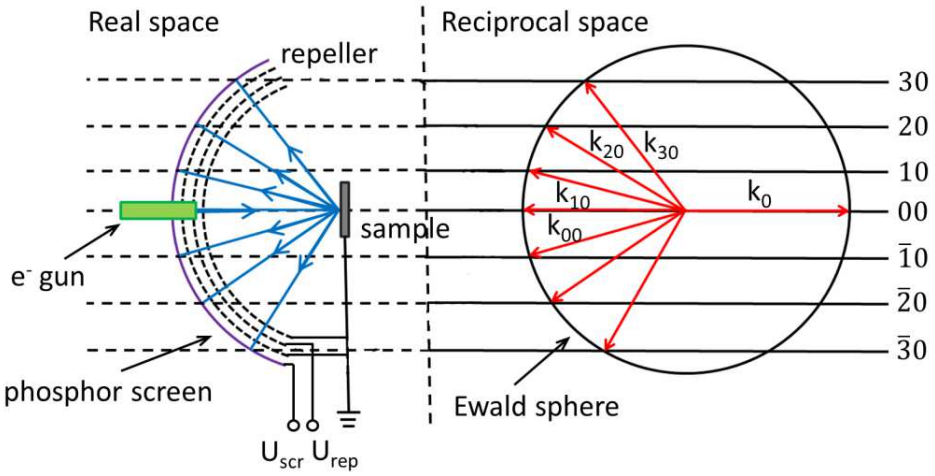


**Figure 3-9.** Schematic of LEED.

Electrons have a limited coherence length at the surface, typically about 5 ~ 10 nm. Electrons scattered from regions of the surface separated by more than a coherence length cannot interfere to produce a diffraction pattern (because the incoming electrons are not coherent). If the size of the ordered region at the surface is greater than the coherence length, then the LEED pattern will have a greater intensity. However, if the size of the ordered regions at the surface is smaller than the coherence length, then the intensity of the Bragg diffraction will be weaker and there will be a large background in the LEED pattern due to the incoherent scattering. Since the probability for the excitation of plasmons and other forms of

electron-electron interactions by the low energy electrons is relatively large, the inelastic mean free path of low energy electrons is only a few atomic layers. LEED thus detects only the topmost several atom layers of the surface. This means that the information from deeper part of the crystal is effectively filtered out. The surface sensitivity of LEED is therefore inherently high.[Ding2004]

The schematic of LEED is shown in Figure 3-9. The $\mathbf{k}_i$-vector of the incoming electrons is normally perpendicular to the sample surface. The elastically scattered (diffracted) electrons come off the sample with $\mathbf{k}_f$-vectors of the same length as $\mathbf{k}_i$, since the electron energy remains constant in elastic scattering. Diffraction intensity occurs when the diffraction condition is fulfilled, i.e., if $\mathbf{k}_f - \mathbf{k}_i$ equals a reciprocal space vector of the lattice. The reciprocal space of a surface consists of lattice rods.

### 3.3.2 LEED I-V

A LEED pattern provides information on the symmetry and periodicity of the surface unit cell. It does not directly give any quantitative knowledge of the exact atomic arrangement of the topmost several atomic layers of a surface. A full understanding of the surface atomic structures also needs the details of the atomic positions with respect to that of the bulk atoms, such as the vertical and lateral displacements of atoms, the positions of atoms in a Bravais lattice, etc. To solve this problem, measurements and calculations of the LEED spot intensity as a function of electron energy are necessary.

The intensity of a certain diffraction beam as a function of the incident electron beam energy is called the LEED I-V curve or LEED spectrum. A quantitative analysis of LEED intensities may provide accurate information on atomic positions. The method to determine positions of the surface and subsurface atoms within each surface unit mesh is to measure the intensities of the diffracted beams in the LEED pattern and compare that with the theoretical I-V curves based on the assuming models.

Quantitative calculations need to take account of multiple scattering effects as used by XPD. The formation used is exactly the same as for XPD. The basic idea of dynamic theory is to divide the atomic structure into several atomic layers, then the multiple scatterings of electrons by the atoms in individual layers are calculated

followed by the calculation of the multiple scatterings of electrons between different layers. The fundamental scattering process is identical to XPD, the major difference is that for LEED the origin of the electron comes from the e-gun outside the sample, while for XPD the electron is from the appropriate core-level of the emitting atom.

The procedure of LEED analysis is as follows. First, a model surface structure is proposed, which is chosen to be consistent with the symmetry of the LEED pattern. Then the computer calculations applying multiple-scattering theory produce theoretical I-V curves, which are compared to the experimental results. Usually, the model needs to have several structural and non-structural parameters systematically varied in order to minimize the differences between calculated and experimental spectra; this is the process of refinement. For example, the spacing between the surface planes is a structural parameter which needs to be varied about the bulk inter-planar spacing in order to minimize the differences between calculated and experimental spectra. The optical-potential, which attenuates the electrons, and the Debye temperature of the model surface are two non-structural parameters that are varied to get the 'best-fit' between calculated and experimental spectra. The process is repeated by adjusting the parameters of the model until satisfactory agreement is obtained. The surface structure is finally determined when the set of theoretical and experimental curves 'match'.[Ding2004]

## 3.4 Mirror electron microscopy - low energy electron microscopy (MEM-LEEM)

Low energy electron microscopy (LEEM), is a full field electron spectroscopy technique invented by Ernst Bauer in 1962, however, not fully developed (by Ernst Bauer and Wolfgang Telieps) until the 1980s with the use of more sophisticated, low energy electron lenses in ultra-high vacuum.[Telieps1985] Nowadays, even attempts at aberration correction LEEM have been made, notably for electron optics systems based on magnetic lenses, which allow ultra lateral resolusion of 2-3 nm.[Tromp2010] LEEM is a technique used to image atomically clean surfaces, atom-surface interactions, and thin films.

In LEEM, high-energy electrons (~20 keV) are emitted from an electron gun, focused using a set of electron optics, and sent through a magnetic beam deflector. There is a high retarding field between the sample and the objective lens. Due to this field, the "fast" electrons travel through the objective lens and are decelerated to low energies of a few eV, the start voltage, near the sample surface, where they are either reflected or backscattered at or on the sample surface. As a result of low kinetic energy with the sample, high electron take-off angles from the sample surface can be collected and imaged through the electron optics. The electrons are surface-sensitive. The incident electron energy can be tuned by varying the difference between the sample and the work functions of the e-gun. The low energy elastically backscattered electrons travel back through the condenser lens, reaccelerate to the LEEM column voltage, because the condenser lens is grounded. A sector field produced by magnetic lenses uses the Lorentz force to separate the incident electron beam formed in an illumination column from the reflected or backscattered beam. Thus, the optical axes of both the incident beam and the backscattered electrons are perpendicular to the sample surface. The sector angles are either 120° or 180°. TL, FL, and IL are the transfer, field, and intermediate lens of the imaging column. Finally, projective lens magnify the image onto the detector.[Barrett2013] A photograph of the LEEM at CEA-Saclay is shown in Figure 3-10.

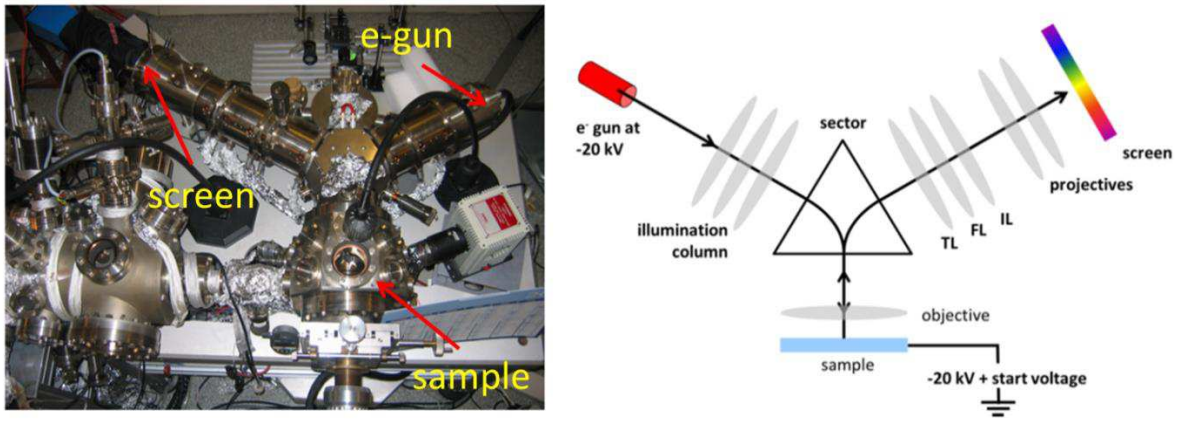


**Figure 3-10.** (a)Photograph of typical instruments (LEEM III, Elmitec GmbH) (b) Layout of the LEEM instrument with magnetic lenses

### 3.4.1 MEM

In Mirror electron microscopy (MEM) the incident electrons are retarded to sufficiently low energy to be reflected by the electrostatic potential above the surface (MEM), whereas at higher SV they penetrate the sample and are backscattered (LEEM). MEM allows non-contact, full-field imaging of the surface topography and potential with 12-15 nm spatial resolution. The transition from the reflection of the electrons to the back scattering regime, the MEM-LEEM transition, is a measure of the electrostatic surface potential. MEM contrast is therefore related to work function differences and it is an ideal tool to probe, for example, surface charge differences in domains with a polarization component perpendicular to the surface, pointing either inwards ($P^-$) or outwards ($P^+$). [Barrett2013]

At the surface, an in-plane electric field will be created at the boundary between oppositely polarized domains due to the fixed charge. Depending on the width of the space charge region around the domain wall, this field can attain values significant with respect to the extractor field, deviating the reflected electrons in a direction parallel to the surface. Thus MEM could be used to study the full surface electrical topography.

The first demonstration of MEM to probe the surface potential of differently polarized ferroelectric domains was reported by Spivak et al. using an extremely simple electron lens and single crystal $BaTiO_3$.[Spivak1959] Cherifi et al. reported polarization induced contrast in thin, epitaxial $BiFeO_3$ films with piezoresponse force microscopy (PFM) written domains.[Cherifi2010] One of the main challenges is the quantification of the surface charge from the measurement of the surface potential, since the latter decreases away from the surface.

### 3.4.2 LEEM

LEEM images surfaces using elastically backscattered low energy electrons. For single crystal systems both real and reciprocal space information is available. The low kinetic energy makes LEEM, like photoemission, intrinsically sensitive to the surface and near surface region. LEEM gives information not only on the surface morphology, but it is also sensitive to the electronic and crystal structure (μ-LEED). In-situ crystal growth or even surface diffusion processes can be monitored.

Furthermore, by scanning the start voltage, the empty states in the conduction band are probed. This has been used to explore quantum oscillations in the back-scattered electron signal for 2D systems. If the focal or diffraction plane is imaged in LEEM, then one obtains a μ-LEED image of the sample surface.[Altman2010] The datasets are in the form of 3D stacks: I(x, y, SV ) for LEEM and MEM; I($k_x$, $k_y$, SV ) for μ-LEED.

## 3.5 Scanning probe microscopy (SPM)

Scanning probe microscopy (SPM) is a family of scanning probe techniques, including many kinds of microscopies. Depending on the different type of SPM, different characteristics of a contact are monitored, such as the tunnel current between tip and surface (STM), the mechanical interaction (AFM), the piezoelectric interaction (PFM), etc. Despite these differences, all SPMs have certain common features. The two basic common features are: (a) a sharp, tiny probe gets very close to the sample and feels the surface by monitoring some kind of interaction between the probe and the surface which is very sensitive to distance. (b) The sample or the probe is scanned in a raster fashion with near atomic accuracy and the variation in the interaction is translated into a map of the surface. The use of precise piezo-ceramic scanners permits probe to be moved over the surface with an accuracy of hundredth of nanometer. The sensitivity of probes and precision of scanners have enabled SPM surface images with highest horizontal resolution of about 0.05 nm and vertical resolution up to 0.01 nm. Here 2 kinds of SPM are used, which is atomic force microscope (AFM) and piezoresponse force microscopy (PFM).

### 3.5.1 Atomic force microscope (AFM)

Firstly introduced in 1986,[Binnig1986] the atomic force microscope (AFM) has turned out to be a unique tool to detect topography and forces on the atomic dimensions. In AFM a sharp tip as shown in Figure 3-11 is brought into contact the surface of the sample when it works under contact mode, and the scan tube is moved by the piezoelectric element below the sample. The cantilever supporting the tip will deform both vertical and lateral directions. To detect the deformations of the cantilever, a four-quadrant photodetector is used with laser beam as in Figure

3-12.[Gnecco2001] The displacement and the torsion of the cantilever is recorded by detecting the changes in angle of deflection.[Morita1996].

The 4-quadrant photodetector defines the deformation by calculating the difference of light densities in the 4 quadrants. The deformation in the vertical direction is given by $\frac{(A+B)-(C+D)}{A+B+C+D}$, and the counterpart in the lateral direction is given by $\frac{(A+C)-(B+D)}{A+B+C+D}$.

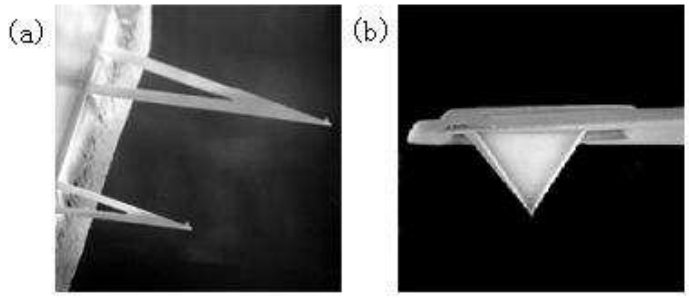


**Figure 3-11.** SEM image of the tip/cantilever used in AFM. (This figure is reproduced from reference [Veeco].)

In addition to the contact mode, the AFM can also operate in tapping mode. Tapping mode is used to measure the surface of the sample which might easily be damaged if measured by contact mode. Moreover, an important function of tapping mode is to study the phase-separation of the sample by a phase image, which is widely used in macromolecule and pharmaceutics samples.

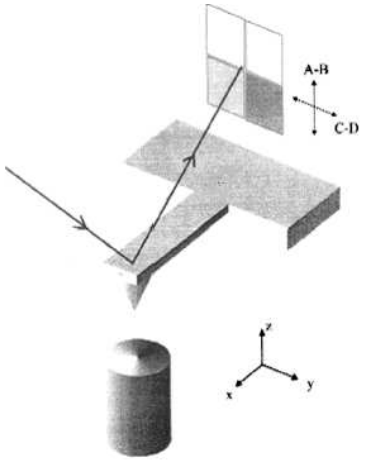


**Figure 3-12.** Schematic of the detection of AFM using a 4-quadrants detector.

### 3.5.2 Piezoresponse force microscopy (PFM)

Piezoresponse force microscopy (PFM) is another technique in the SPM family, particularly useful for ferroelectric surface because all ferroelectric materials are also piezoelectric. PFM measures the mechanical response when an electrical voltage is applied between the sample and an electrode on the bottom face of the sample in contact with a conductive tip of AFM. In response to the electrical stimulus, the sample then locally expands or contracts as shown in Figure 3-13.

When the tip is in contact with the surface, the local piezoelectric response is detected as the first harmonic component of the tip deflection. The phase φ, of the electromechanical response of the surface with respect to the applied voltage yields information on the polarization direction below the tip. For $c^-$ domains (polarization vector oriented normal to the surface and pointing downward), the application of a positive tip bias results in the expansion of the sample, and surface oscillations are in phase with the tip voltage, $\varphi = 0$. For $c^+$ domains, the response is opposite and $\varphi = 180°$.[Vilquin2009, Kalinin2002, Kalinin2004, Proksch]

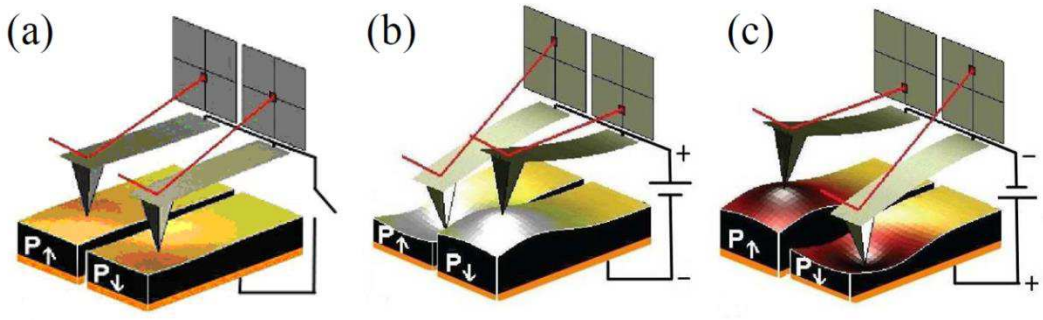


**Figure 3-13.** The principle of PFM imaging. (a) no voltage (b) positive voltage and (c) negative voltage is applied to the tip. (This figure is reproduced from reference [Proksch].)

Detection of the lateral components of tip vibrations provides information on the in-plane surface displacement, known as lateral PFM. A third component of the displacement vector can be determined by imaging the same region of the sample after rotation by 90°.[Eng1999] Provided that the vertical and lateral PFM signals are properly calibrated, the complete electromechanical response vector can be determined, an approach referred to as vector PFM.[Kalinin2006] Finally, electromechanical response can be probed as a function of DC bias of the tip, providing information on polarization switching in ferroelectrics, as well as more

complex electrochemical and electrocapillary processes.[Verdaguer2006, Sacha2006]

## 3.6 Molecular beam epitaxy (MBE)

The technique of Molecular beam epitaxy (MBE) was first used successful by A. Y. Cho and J. R. Arthur to fabricate GaAs epilayers[Cho1971, Cho1975]. Now it has been developed to a versatile tool for growing many epitaxial structures of high crystalline quality, i.e. semiconductors, metal, insulators etc. MBE has several unique advantages compared with other epitaxial growth techniques.

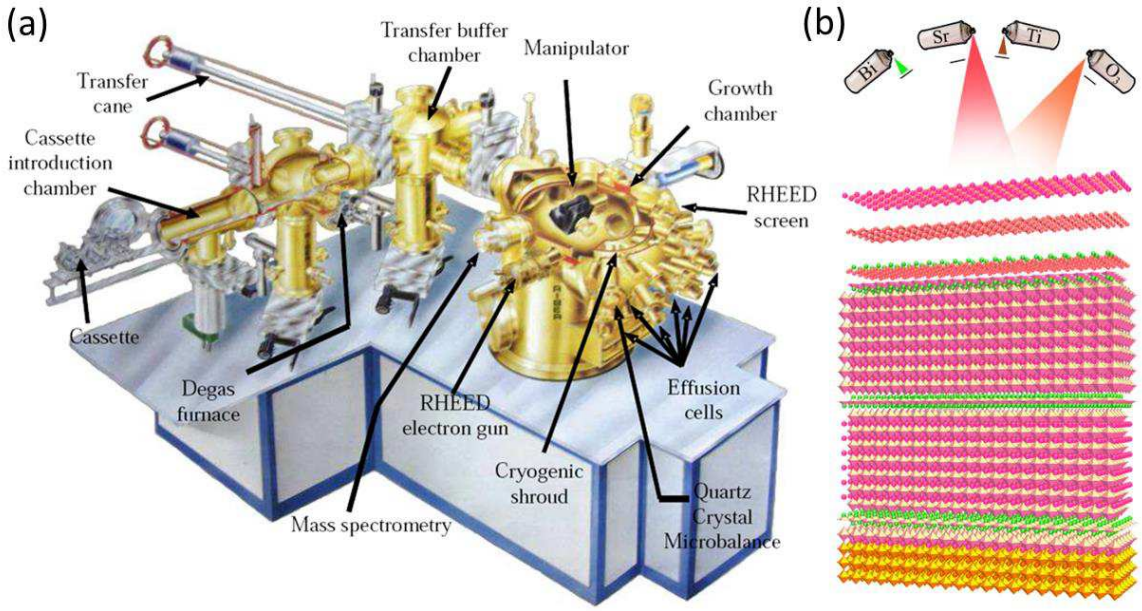


**Figure 3-14.** Schematic of (a) the main block building of Riber 2300 oxide reactor MBE and (b) representation of the MBE growth, in this case, a $Sr_4Bi_4Ti_7O_{24}$(001) film on a $LaAlO_3$–$Sr_2AlTaO_6$ (LSAT) (001) substrate. (These figures are reproduced from reference [Niu2010] and [Schlom2008], respectively.)

The MBE method of thin film growth may be thought of as atomic spray painting, as shown in Figure 3-14(b) in which an oxide ferroelectric structure, e.g., $Sr_4Bi_4Ti_7O_{24}$ is schematically assembled layer by layer. The flux of spray from each atomic or molecular beam is controlled by the temperature (and thus vapor pressure) of the effusion cell in which each species is contained. The duration of spray is individually controlled for each beam by shutters, which control not only the open time (and thus dose), but also the sequence in which species reach the growth

surface. By controlling the shutters and temperature of the evaporant (which control dose and flux, respectively), the layering sequence of the desired structure can be customized. This technique is capable of controlling the layering of oxides on a unit cell level.[Schlom2008]

Since MBE growth is carried out in an ultra high vacuum chamber with pressure lower than $10^{-9}$ Torr, it can ensure the high purity of the deposited material. At the same time, the vacuum conditions enable mass transport towards the substrate with a large mean free path. In MBE, the typical growth rate can therefore be quite slow, ~1 monolayer/s, which is low enough to ensure surface migration of the impinging species on the growing surface, leading to a smooth surface of the grown film.

For MBE equipped with in-situ surface sensitive diagnostic methods such as reflection high energy electron (RHEED), X-ray photoelectron spectroscopy (XPS), Scanning tunneling microscopy (STM), we can have controllable fabrication of sophisticated device structures.

Here all the thin film samples were realized in a Riber 2300 oxide reactor MBE at Lyon Nanotechnology Institute (INL). The main building blocks of this machine are schematically presented in Figure 3-14.

The MBE growth chamber is equiped with an ion pump, a turbo pump, a titanium sublimation pump and a liquid nitrogen cooling trap, which help to achieve a vacuum down to $1\times10^{-10}$ Torr. Knudsen effusion cells made of Pyrolytic Boron Nitride (PBN) are used for Ba and Ti growth. Associated with each cell, there is a separate refractory metal shutter. The shutters can interrupt the beams between the sources and substrate to shield the substrate from each individual beam when closed. The RHEED system is used for in-situ monitoring the surface structure of film on the substrate. A high energy beam of electrons (30 keV) is incident on the substrate at a glancing angle of 1°~3°. Therefore the penetration of the beam into the surface is restricted to the outermost few atomic layers and reveals the surface structure information of the film from the intersection of the reciprocal lattice rods with the Ewald's sphere, projected onto the phosphor screen, as shown in Figure 3-15. Oxygen is introduced into the reactor via a pressure-regulated plasma chamber, which permits to precisely control the oxygen partial pressure in the chamber, particularly at the first stage of the oxides growth. Both

atomic and molecular oxygen can be chosen. In our experiment, the atomic oxygen is produced by a radio frequency plasma generator with frequency of 13.56 MHz and maximum power output of 600W.

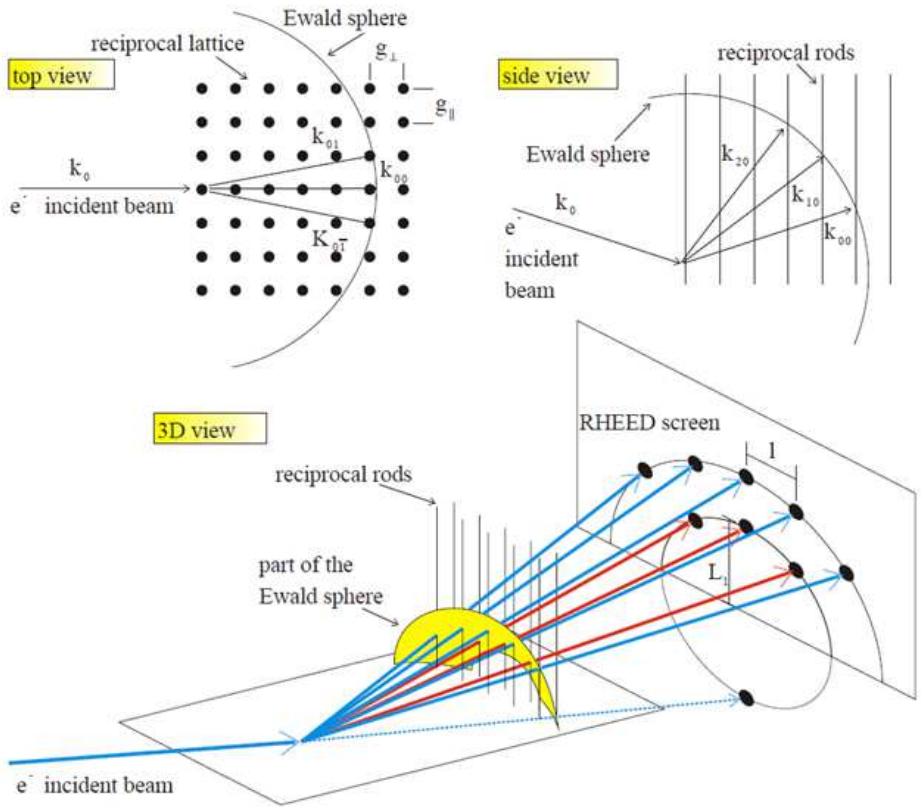


**Figure 3-15.** Schematic of RHEED construction. (This figure is reproduced from reference [Klein2001].)

## 3.7 Temperature-programmed desorption (TPD)

Temperature-programmed desorption (TPD) is a well-known technique which consists of analyzing by mass spectrometry the desorption flux of gas from a surface during heating.[Peillex1995, Ehrlich1963，Readhead1962，Carter1962，Smutek1975] From the temperature dependence of the desorption curve for a given m/e ratios, it is possible to deduce the species and gain quantitative information on chemical bond and population of adsorbed species.[Joly2000]

The set-up is shown in Figure 3-16. All TPD measurement were carried out at the Institute of Researches on Catalysis and Environment in Lyon (IRCELYON).

The sample is placed in a glass reactor (~$10^{-8}$ Torr) and is supported by a K-type capillary thermocouple spot welded on the sample holder. Therefore, the sample is virtually isolated mechanically and thermally from both the reactor and the heating device. Heating is achieved by a high frequency (1.1 MHz, maximal power 6 kW, manufactured by EFD Induction S.A.) system, with an inductive coil placed outside the reactor allowing heating rates ranging from 10 to 200 K/min with a small temperature gradient at the sample surface. The reactor is fitted with a line used to introduce treatment gases ($O_2$, for instance) or probe molecules at selected pressures. Analysis of compounds released during the TPD experiment is carried out by means of a quadrupole mass spectometer (VGgas Smart-$IQ^+$). A peak selector enables the user to collect the data of several masses simultaneously. Both spectrometer and thermocouple are interfaced to a computer and data processing is performed by home-made, dedicated program.

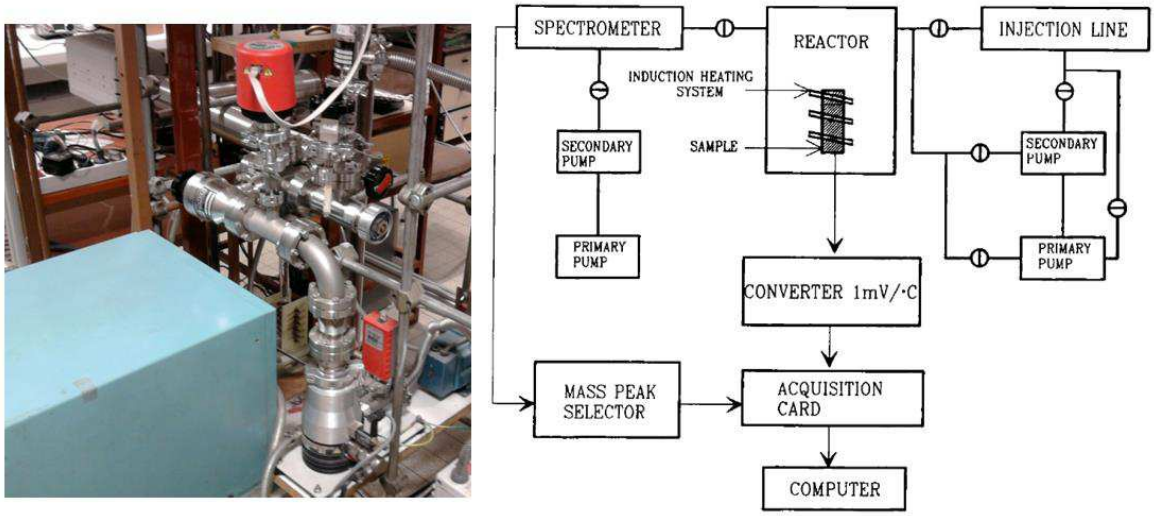


**Figure 3-16.** Schematic and block diagram of the TPD system. (This figure is reproduced from reference [Peillex1995].)

The rate of desorption from unit surface area may be written as

$$\mathrm{N(t)} = -\frac{d\sigma}{dt} = \nu_n \sigma^n exp(-E/RT)$$

where n is the order of the desorption reaction, σis the surface coverage (molecules/$cm^2$), $\upsilon_n$ is the rate constant, and E is the activation energy of desorption (cal/mole).[Readhead1962]

Normally, first-order desorption kinetics are often associated with molecules adsorbed in a molecular state, whereas second order kinetics are more consistent with molecules that have undergone dissociative chemisorption.[Garra2009]

## 3.8 Synchrotron radiation

The radiation emitted by a charged particle moving with constant, relativistic velocity on a circular arc, is called synchrotron radiation. It was first discovered by Frank Elder, Anatole Gurewitsch, Robert Langmuir, and Herb Pollock in a General Electric synchrotron accelerator built in 1946.[Elder1947]

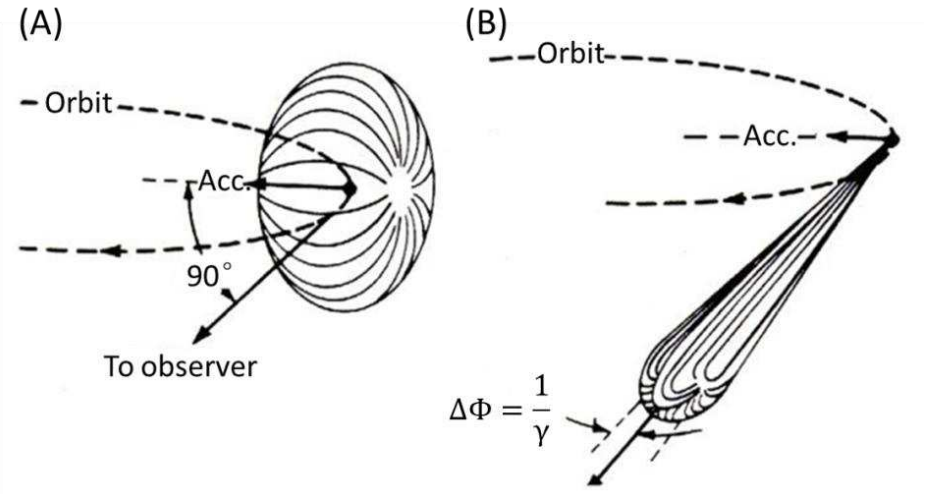


**Figure 3-17.** The radiation pattern for a charged particle traversing a circular trajectory (a) with non-relativistic velocity, and (b) moving at relativistic speed. (This figure is reproduced from reference [Juarez-Reyes2001].)

When high-energy charged particles are in rapid motion, forced to travel in a curved path by a magnetic field, synchrotron radiation is produced, since a charged particle constrained to move in curved path experiences a centripetal acceleration. Due to this acceleration, the particle radiates energy according to Maxwell equations. A non-relativistic particle emits radiation primarily at its frequency of revolution, with the characteristic pattern shown in Figure 3-17(a). However, as the speed of the particle approaches the speed of light, the radiation pattern is distorted by relativistic effects and changes to a narrow cone of radiation with angular spread$\Delta\ \phi \approx\ 1/\ \gamma$ , where $\gamma = 1/\sqrt{1-(v/c)^2}$, and v is the velocity of the particle.[Hofmann2007]

Therefore, for high values of γ, a well-collimated fan of radiation is produced. For an observer located in the laboratory frame of reference, the radiation emitted by the charged particle consists of a series of short pulses of light. Each pulse is separated from each other by a period equal to the transit time of the electron in the circular path. It can be shown, using Fourier analysis, that the spectrum of synchrotron radiation produced by the charged particle extends from the frequency of revolution, ω, to frequencies of higher harmonics. In practice, however, the electron orbit frequency is not precisely given, because a charged particle confined to follow a circular orbit oscillates in position and energy about its equilibrium orbit. Thus, the spectrum of even a single particle will be smeared out into a continuum. This implies that synchrotron radiation sources produce photons with a continuum of energies(or colors), from the infrared, to the X-Ray region. Monochromatic radiation of the desired wavelength can be obtained by locating a monochromator at a tangential point of the circular orbit, where the radiation is emitted.[Juarez-Reyes2001]

The general layout of a modern synchrotron light source is sketched in Figure 3-18. The synchrotron radiation from electron storage rings of the 3rd generation is essentially produced by wiggler and undulator magnets. The bending magnets only guide the beam along the circular orbit.

Good beam quality and significantly high brilliance is provided by wiggler and undulator magnets (W/U magnets) installed in special straight sections in electron storage rings. These types of magnets often are summarized under the name “insertion devices”. The general arrangement of such magnets is sketched in Figure 3-19. It consists of a sequence of short bending magnets of constant length. The design principal of wiggler magnets is basically the same as of undulator magnets. The difference comes from the field strength. Wigglers use a strong field resulting in a wide horizontal opening angle of the emitted radiation. The wide photon spectrum provides light of shorter wavelength without changing the apparatus of electron storage rings. The opposite are undulators with rather weak fields and correspondingly small opening angles of synchrotron light. In this case the photons can interfere and the emitted radiation is mainly coherent with a wavelength determined by the period length of the undulator and the beam energy.[Turner1998]

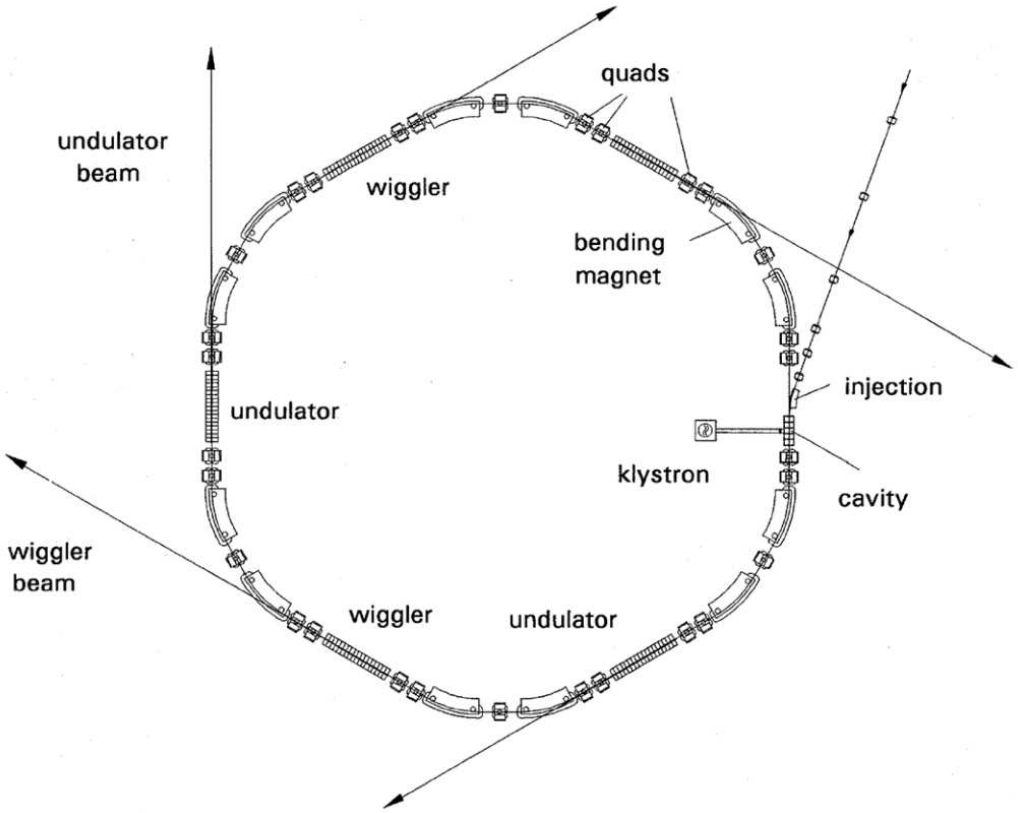


**Figure 3-18.** General layout of a modern synchrotron light source of the 3rd generation. (This figure is reproduced from reference [Turner1998].)

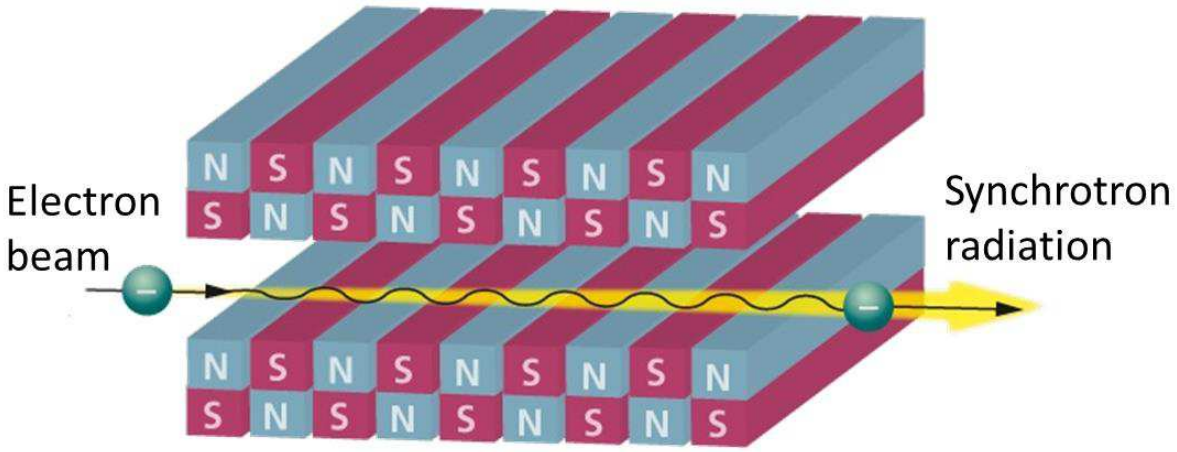


**Figure 3-19.** General layout of a wiggler or undulator magnet.

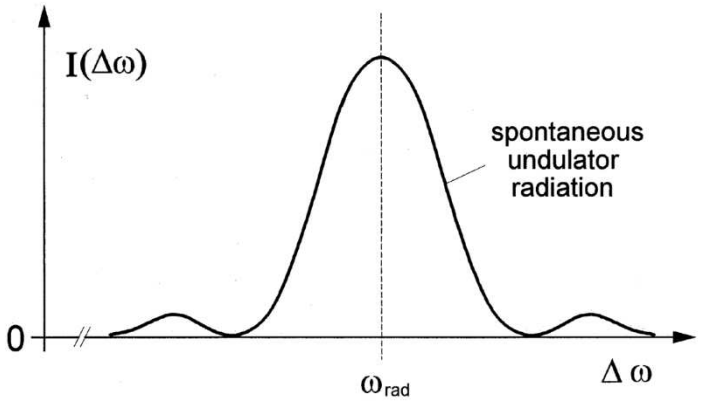


**Figure 3-20.** General layout of a modern synchrotron light source of the 3rd generation. (This figure is reproduced from reference [Turner1998].)

For many experiments with synchrotron radiation the width of the spectrum lines emitted from an undulator is an important parameter. After passing an undulator of $N_u$ periode, the intensity (Figure 3-20)

$$I(\Delta\omega) \propto \left[\frac{\sin\left(\pi N_u \frac{\Delta\omega}{\omega_{rad}}\right)}{\pi N_u \frac{\Delta\omega}{\omega_{rad}}}\right]^2$$

The resolution of the undulator radiation is simply determined by the number of undulator periods. High resolution requires a sufficient large number $N_u$.

Thus the developments of modern synchrotron radiation sources provide some unique properties: high brightness and coherence, energy tunability and high energy resolution, polarization control, and pulsed time structure.

Our XPD experiments were carried out at the Antares beamline of Synchrotron Soleil. This beamline has been designed for a complete electronic structure determination using spinand-helicity angle-resolved photoemission spectroscopy combined with a local structural characterization by means of photoelectron diffraction (PED) through its both modes, forward scattering and backscattering energy regimes. Also the beamline satisfies the conditions of a high-energy resolution and high-flux source of photons at the focal point, where a 5-axis high precision programmed manipulator can control the sample's azimuthal and polar position with high precision.

# Chapter 4

# Chemistry and atomic distortion at the surface of an epitaxial $BaTiO_3$ thin film after dissociative adsorption of water

## 4.1 Introduction

The adsorption and dissociation of water on transition metal oxides(TMO) surfaces has been widely studied.[Henderson2002, Hodgson2009, Henderson2011] Water can bond to a surface via molecular ($H_2O$) or dissociative (an $OH^-$ ion and a proton, $H^+$) adsorption. Both types of adsorption can give rise to mobile species. Physisorbed molecules can subsequently dissociate and bond chemically to surface atoms; chemisorbed ions can undergo recombination to form molecular species. The chemistry of the TMO can strongly influence the adsorption mechanism. For example, the SrO-terminated perovskite oxide $SrTiO_3$ (STO) favors dissociative adsorption, whereas on the $TiO_2$-terminated surface, molecular adsorption is more stable.[Evarestov2007] Chemisorption occurs through bond formation. One way of enhancing this can be direct collisional activation; [Lohokare1998] however, more importantly, chemisorption can be enhanced by precursor-mediated adsorption, where the molecule is first trapped in a weakly bound physisorbed state, which is a precursor for the formation of chemical bonds.[Brown1998, Li2008] In this case, impinging water molecules get trapped into a shallow physisorption well, dominated by van der Waals interactions and static charge on the surface. These interactions are not sufficiently strong to fix the water molecule at the initial adsorption sites and the trapped precursor can migrate over the surface. Many trapped molecules spend a short time on the surface and then desorb. However, if a molecule encounters a more active site, for example, an oxygen vacancy (Vo), the precursor may react to form a chemisorbed species, in which chemical bonds are formed.[Wendt2006]

The interaction of water with ferroelectric oxide surfaces is less well-known, yet it is of considerable importance.[Shin2009, Garra2009] As mentioned in chapter 1, one of the motivations of this thesis is that the hydrogen yield can be enhanced by over an order of magnitude at the surface of a ferroelectric.[Kim1999, Kim2004] The polar nature of water means that it can interact strongly with the ferroelectric polarization changing the electrical boundary conditions. Geneste and Dkhil[Geneste2009] have shown that on the (001) surface of $BaTiO_3$ (BTO) with in-plane polarization there are competing molecular and dissociative adsorption mechanisms. The static charge on the surface changes the depth of the physisorption well,[Zhao2008] which determines the average residence time of the precursor on the surface, leading to a greater chance of finding a chemisorption defect site. Typical molecular and dissociative adsorption energies are ~0.1 to 0.2 eV and ~1.0 eV, respectively. Another important aspect of dissociative adsorption is the production of $H^+$ capable of bonding to lattice oxygen. The presence of hydrogen in ferroelectrics is known to be a factor that increases imprint, potentially inhibiting switching of the polarization.[Park2000] In $PbTiO_3$, $OH^-$ adsorption favors an upward pointing polarization state, whereas $H^+$ adsorption stabilizes downward pointing polarization.[Fong2006] Therefore, the interaction of water with the surface of a ferroelectric is of primary importance whether it is for applications in electronics or catalysis.

In this chapter, we study water adsorption on the $TiO_2$-terminated BTO(001) surface. The surface structure is obtained using XRD, AFM, and quantitative LEED I−V.[VanHove1986] Recording the intensity variations in the LEED spots as a function of electron primary energy, LEED I−V is the equivalent of probing the structure factor. The penetration depth of the low energy electrons is limited to the first few atomic layers of the surface, providing quantitative information on the local atomic structure around each emitting atom with a precision of approximately ±0.1 Å. XPS is used to reveal the presence of hydroxyl groups rather than molecular $H_2O$ on BTO surface, which demonstrate dissociative adsorption of $H_2O$. TPD measures one additional feature at low desorption temperature on reduced BTO surface, which corresponds to molecular dissociative adsorption. By combining the structural, chemical and energetic information, we show that: (i) $H_2O$ undergoes mainly dissociative adsorption on the polarized BTO(001) surface; (ii) there are two competing sites for dissociative adsorption (Vo and on-top Ti

lattice atoms); (iii) adsorption oxidizes surface $Ti^{3+}$ ions; (iv) the on-top surface Ti is the dominant $OH^-$ chemisorption site; and (v) the concentration of Vo favors initial physisorption.

## 4.2 Experiment

The commercial SurfaceNet $SrTiO_3$ (001) substrate with an optical mirror surface finish was etched with buffered $NH_4$−HF solution (BHF) and then annealed in $O_2$ at 950 °C with a flow rate of 5 l/min for 10 h to obtain a $TiO_2$-terminated surface composed of steps and atomically flat terraces following the established protocol.[Kawasaki1994] After heating the substrate to 650 °C for 1 h under an oxygen partial pressure of $\sim 10^{-6}$ Torr to remove carbon contamination on the surface, 8-nm-thick $TiO_2$-terminated BTO films were grown on this substrate by molecular beam epitaxy (MBE) with a growth rate of ∼1 mono-layer per minute (ML/min). The metallic Ba and Ti were put in the Knudsen cells heated by resistance coils to produce the vapor flux. During growth, the oxygen partial pressure was kept at $2 \times 10^{-6}$ Torr, and the substrates were maintained at 630 °C to get an atomically flat surface. The growth of the BTO was monitored by in situ RHEED, which allowed a precise control of the number of atomic layers. At 8 nm, the Ba source was switched off, ensuring deposition of a $TiO_2$ last layer. Figure 4-1(a) shows the RHEED pattern in the [100] direction of the BTO film. The intense lines correspond to the BTO film, whereas the faint half-order lines reflect the (2 × 2) reconstruction of the $TiO_2$ termination layer.[Niu2011] An XRD of an identical 8 nm BTO film is shown in Figure 4-1(b); the in-plane lattice constant is 3.911 Å, giving an in-plane compressive strain of 2.2 %.

Water exposure was performed in a dedicated, third chamber. Pure $H_2O$ was obtained by freeze−pump−thaw cycles and then introduced into the chamber at $1 \times 10^{-4}$ Torr for 1 h, equal to $3.6 \times 10^5$ L.

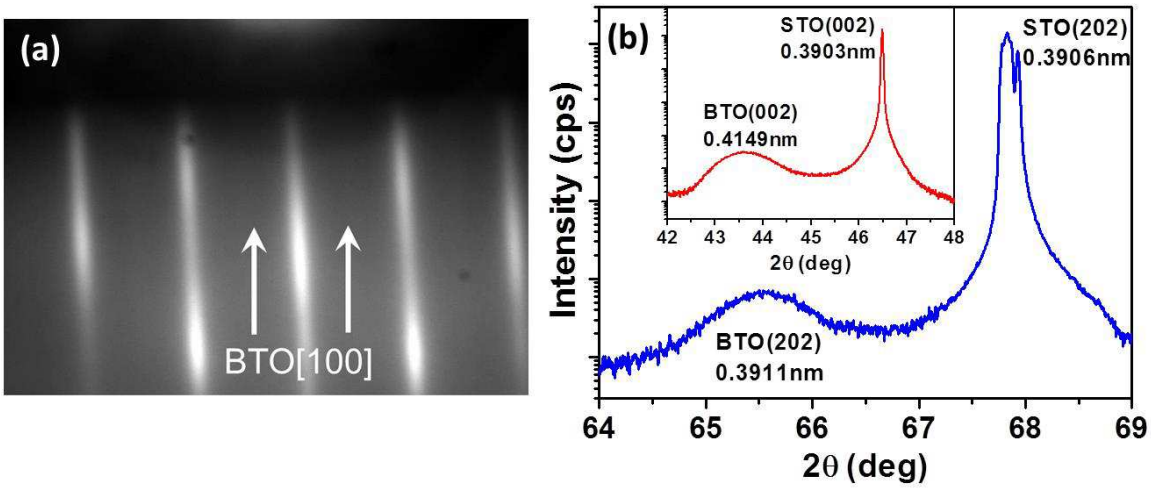


**Figure 4-1.** (a) RHEED pattern along [100] showing intense lines due to BTO(001) and fainter lines reflecting the (2 × 2) as-deposited $TiO_2$ reconstruction. (b) In- and out-of-plane (inset) XRD on 8 nm BTO/STO showing compressive in-plane strain of 2.2 %.

The freeze-pump-thaw process for degassing of liquids is as follows.

1) Less than 50 % volume of the flask is filled with water, because overfilled flasks can shatter the flask on freezing.

2) Hook up the flask to a line connected with mechanic pump and freeze the water by liquid nitrogen.

3) When the water is frozen, the valve to pump is open and the system is pumped off for around 10 minutes

4) close the valve to pump.

5) Thaw the solvent until it just melts using a tepid water bath. Gas bubbles can be seen from the solution. Let the frozen water thaw by itself.

6) Replace the water bath with liquid nitrogen and refreeze the solvent.

7) Repeat steps (3) – (7) until we no longer see the evolution of gas as the solution thaws. The water should be put through a minimum of three cycles.

8) Slowly turn on the micro-valve to intro-chamber (base pressure ~$10^{-7}$ Torr) until the pressure in the intro-chamber arriving at $1 \times 10^{-4}$ Torr.

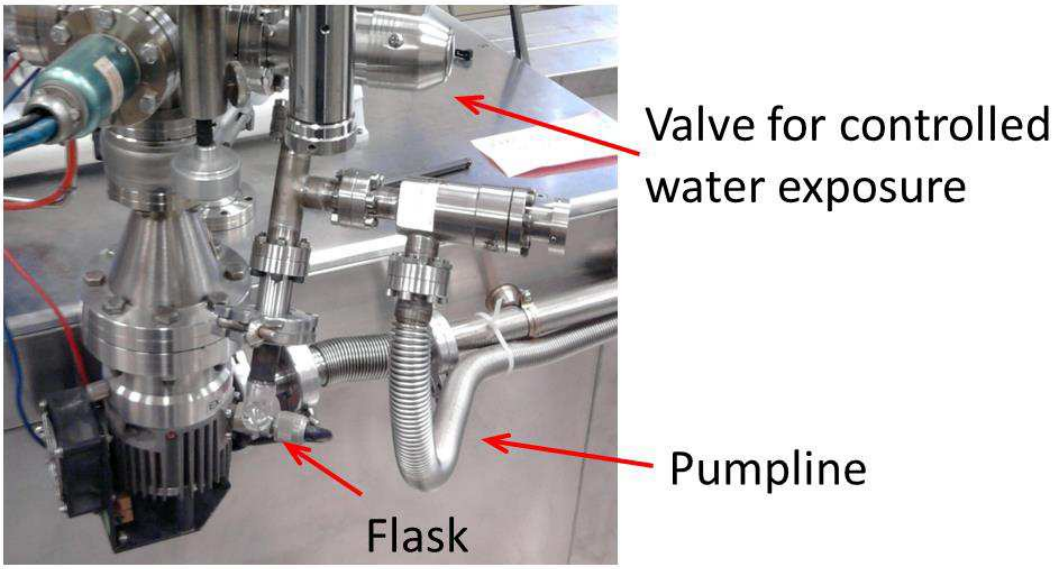


**Figure 4-2.** Schematic of the chamber for water exposure.

After the controlled exposure of water, the sample was transferred back to the main chamber for the LEED and XPS analysis. The LEED patterns of the film were taken at room temperature in energy steps of 2 eV between 40 and 260 eV with a high-resolution chargecoupled device (CCD) camera. Experimental I−V curves were extracted from digitized diffraction patterns; after averaging the symmetrically equivalent beams, they were smoothed using a five-point least-squares cubic polynomial algorithm and normalized to the electron gun current.

XPS was carried out using an Argus analyzer with pass energy of 20 eV, which gave an overall energy resolution (photons and spectrometer) of 0.35 eV. The binding energy (BE) scale was calibrated using the C 1s line at 284.6 eV as a reference. A 30° takeoff angle was used to increase the surface sensitivity of the core level peaks. The data were analyzed using the CasaXPS software,[CasaXPS] which employs a linear least-squares optimization with a peak-fitting algorithm. Shirley backgrounds were subtracted from the data as part of the curve-fitting process.

The TPD measurement were carried out in a separate chamber requiring a transfer in air. Before starting the TPD measurement, samples were annealed in the reactor to remove the surface contamination, confirmed by a quadrupole mass spectrometer signal from $CO_2$ and $H_2O$ near the baseline level.

## 4.3 Results on 8-nm $BaTiO_3$ on $SrTiO_3$

### 4.3.1 AFM

Figure 4-3(a) is the AFM topography image of the STO substrate after treatment, showing wide, flat terraces with a single unit-cell step height of 0.4 nm, as marked in Figure 4-3(c). Figure 4-3(b) is the AFM image after growth of 8 nm BTO film, demonstrating that the morphology of single unit cell step height between terraces has been maintained in the BTO film. This is strong evidence for near-perfect layer by layer growth.

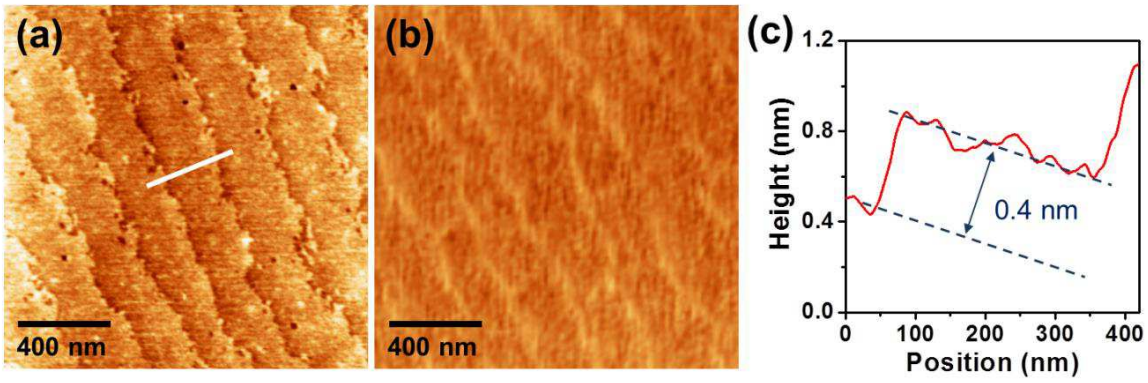


**Figure 4-3.** AFM topography image of STO substrate (a) after treatment and (b) after growth of BTO thin film. (c) Line profile showing the one unit cell terrace step height.

### 4.3.2 LEED

The LEED patterns for the clean BTO(001) and after exposed to $H_2O$ vapor up to $3.6 \times 10^5$ L are presented in Figure 4-4(a)-(f) with different energies. The well-defined (1 × 1) LEED patterns show square symmetry characteristic of the BTO(001) surface and indicate a good crystal quality of the film. After exposition to $H_2O$ vapor, LEED patterns like that shown in Figure 4-4(a')-(f') were obtained.

The symmetry is the same as before $H_2O$ adsorption, but the spot and background intensities change. However, if more than one $H_2O$ layer was present, then a c(2 × 2) ice structure should be formed as in Figure 4-5, which is not consistent with the symmetry of our observations.[Henderson2002, Thiel1987] Multiple disordered water layers can also be ruled out because these should more

significantly reduce the LEED intensities and increase the background level compared with those obtained before adsorption. We deduce that at most a single-ordered $H_2O$ layer is adsorbed epitaxially on the clean BTO surface. Therefore, the observation of sharp, ordered LEED patterns after $H_2O$ adsorption indicates that the surface retains the same symmetry without the formation of superstructures and rules out growth of disordered multilayers of water on the surface.

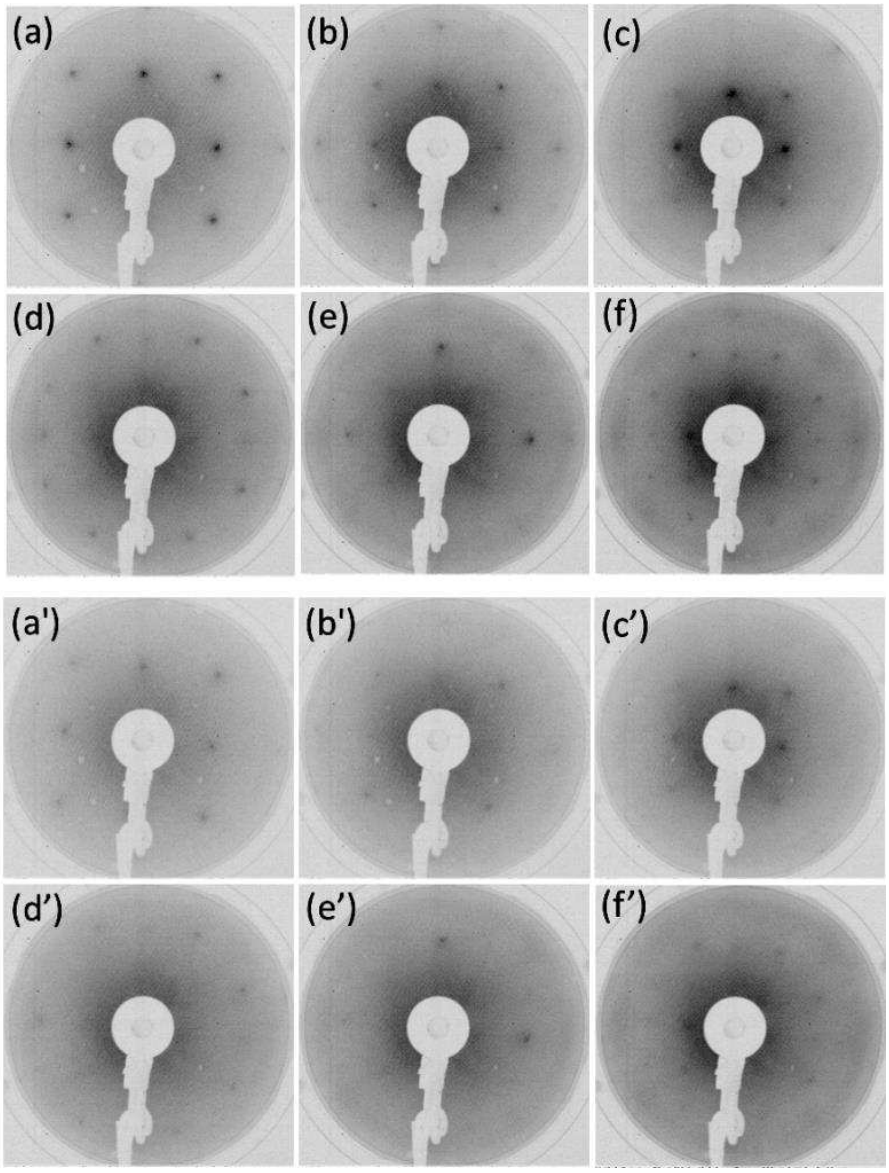


**Figure 4-4.** LEED images of BTO surface for electron energies of (a) 70 (b) 100 (c) 130 (d) 150 (e) 180 and (f) 220 eV before (top) and after (bottom) water exposure.

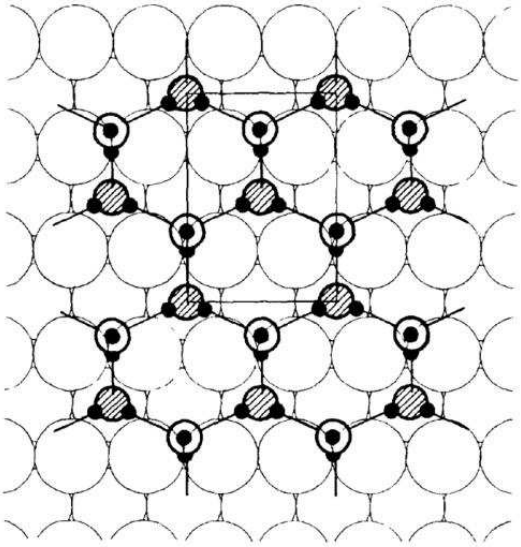

**Figure 4-5.** Schematic diagram of a compressed $H_2O$ bilayer giving a c(2 × 2) LEED pattern on an fcc(110) surface. (This figure is reproduced from reference [Thiel1987].)

### 4.3.3 LEED simulations

The LEED I−V simulations were carried out by Dr. A. Pancotti using a symmetrized automated tensor method implemented with the SATLEED code.[Barbieri] A muffin-tin (MT) potential is employed in the multiplescattering calculations to describe the individual atoms. Debye temperatures obtained from X-ray and neutron diffraction results for tetragonal bulk $BaTiO_3$ were 250, 760, and 490 K for the Ba, O, and Ti, respectively.[Harada1970] The imaginary part of the inner potential was fixed to −6.0 eV. Ten relativistic phase shifts were employed in the calculations. The simulated LEED I−V curves were compared with the experimental data using the Pendry reliability R factor.[ Pendry1980]

To determine the surface structure, LEED I−V analysis was performed on the first and second order diffraction spots. A quantitative analysis of the I−V dependence should provide information on the surface structure before and after water adsorption. The blue curves in Figure 4-6 illustrate the quite different experimental diffraction intensities as a function of energy for samples before and after $H_2O$ exposure, pointing to significant changes in surface structure. The low electron energies used mean that these changes occur over the first one to three unit cells. Two structural models for the $TiO_2$-terminated surface were used in the simulations, corresponding to $P^+$ and $P^-$ polarization states. The initial parameters

are given in Table 4-I. We have also tested the two models for a BaO surface termination, but, as expected for a $TiO_2$-terminated surface, the R factors are much worse. A positive value for the rumpling ($\Delta Z$) indicates that the cation is higher, that is, closer to the surface, than the oxygen anion. Conversely, a negative value means that the oxygen ion is closer to the surface. The in-plane lattice constant was fixed at 0.391 nm, corresponding to the XRD experimentally measured value of compressively strained BTO on the STO substrate. Then, the out-of-plane atomic positions were relaxed for both models until a minimum in the R factor was obtained for both $P^+$ and $P^-$ initial structures. The simulated LEED I−V curves are shown in Figure 4-6 in red. The results are also given in Table 4-I.

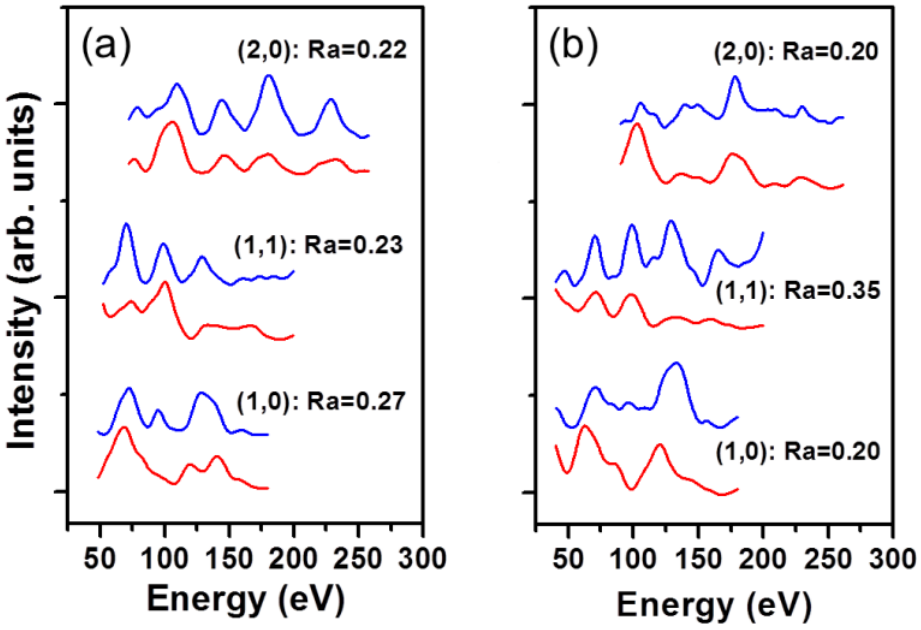


**Figure 4-6.** Experimental (blue) and simulated (red) LEED I−V curves for BTO thin film (a) before and (b) after water exposure.

The best R factor before water adsorption for the optimized $P^+$ structure is 0.25, twice as good as that obtained for the $P^-$ structure. Figure 4-7(a) shows a schematic cut of the best optimized $P^+$ structure over the first two unit cells. The average polarization over the first two unit cells is still $P^+$, pointing vertically toward the surface. However, the rumpling of the top $TiO_2$ layer has produced a downward pointing electric dipole, opposite to that of $TiO_2$ in the bulk.

| Structure | Bulk | | Before | | After | |
|---|---|---|---|---|---|---|
| | $P^+$ | $P^-$ | $P^+$ (R=0.25) | $P^-$ (R=0.49) | $P^+$ (R=0.25) | $P^-$ (R=0.59) |
| $\Delta Z_{TiO-1}$ | +0.197 | -0.197 | -0.109 | +0.120 | +0.102 | +0.090 |
| $\Delta Z_{BaO-2}$ | +0.044 | -0.044 | +0.060 | -0.030 | -0.188 | -0.022 |
| $\Delta Z_{TiO-3}$ | +0.197 | -0.197 | +0.006 | +0.067 | +0.062 | +0.060 |
| $\Delta Z_{BaO-4}$ | +0.044 | -0.044 | +0.076 | +0.080 | +0.079 | +0.078 |
| $d_{12}$ | 2.12 | 2.09 | 2.06 | 2.09 | 2.03 | 2.06 |
| $d_{23}$ | 2.09 | 2.12 | 2.11 | 2.02 | 2.06 | 2.02 |
| $d_{34}$ | 2.12 | 2.09 | 2.01 | 2.01 | 2.05 | 2.01 |

**Table 4-I.** Initial $P^+$ and $P^-$ structures used for the LEED I−V simulations together with the optimized structures before and after water adsorption obtained by refinement of simulations and their R-factors (Ionic rumpling on the first four atomic layers is denoted by $\Delta Z$; the average interplane separation between planes i and j is denoted by $d_{ij}$ (all units in Å).)

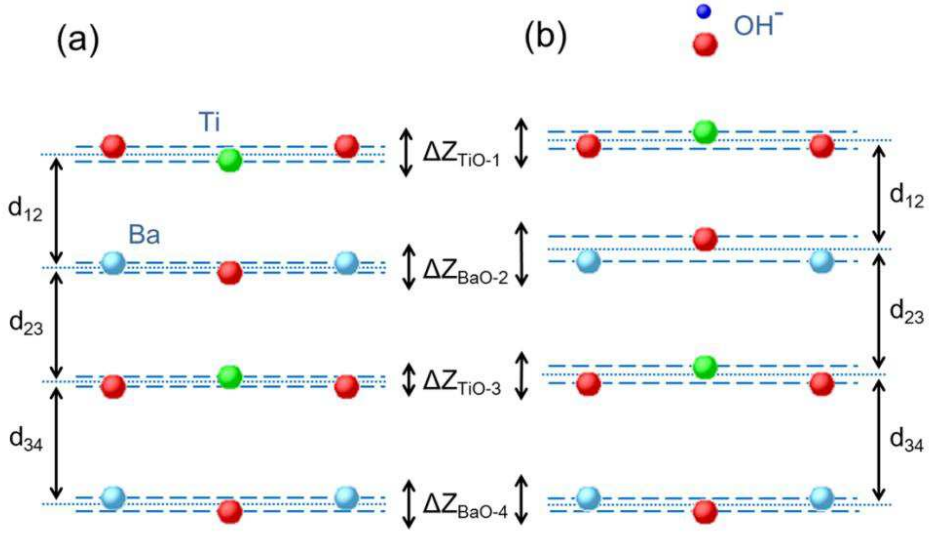


**Figure 4-7.** Schematic sections of the optimized surface structure of BTO(001) (a) before and (b) after water adsorption, as determined from minimization of the R factor by out-of-plane relaxation and in (b) $OH^-$ on-top Ti coverage. The interlayer spacings $d_{12}$, $d_{23}$, and $d_{34}$ are defined as the distances between two midpoints of consecutive layers. Ba atoms are blue, Ti atoms are green, and O atoms are red spheres.

The LEED I−V simulations after water exposure were also performed using the same two initial models, $P^+$ and $P^-$. The unchanged symmetry of the LEED patterns means that there is no long-range ordered surface reconstruction. In the simulations, the contribution of the hydrogen atom to the LEED intensities is assumed to be negligible, and only the position of the oxygen of the $OH^-$ is taken into account. The XPS analysis (see below) strongly suggests the dissociated desorption and that

the dominant chemisorption site for $OH^-$ is the on-top Ti site. The simulations have therefore optimized the out-of-plane atomic relaxation with a random distribution of $OH^-$ radicals banded to on-top Ti sites. The best agreement between experimental and theoretical LEED I−V curves is presented in Figure 4-6. The $P^+$ and $P^-$ structures with the R-factor after relaxation are reported in Table 4-I. The optimized $P^+$ structure is clearly in better agreement with the experimental results. A schematic vertical cut over the first two unit cells with an $OH^-$ adsorbed at an on-top Ti site is shown in Figure 4-7(b). The main result is that the adsorption of $OH^-$ at on-top Ti surface atom sites has switched the dipole of the surface $TiO_2$ layer back to the direction of the bulk polarization.

### 4.3.4 TPD

TPD spectra for $H_2O$ desorption, using a mass-tocharge ratio (m/e) of 18, are presented in Figure 4-8(a). The relative intensities of the m/e signal are directly related to the quantity of desorbed water. The spectra are acquired from room temperature to 700 °C on the as-received BTO thin film. The sample is maintained at 700 °C for 30 min prior to starting a new TPD ramp. Thus, successive TPD spectra measure the effect of an increasing concentration of oxygen vacancies on the desorption. The spectrum for the as-grown BTO sample exhibits a broad thermal desorption peak starting at ~350 °C.

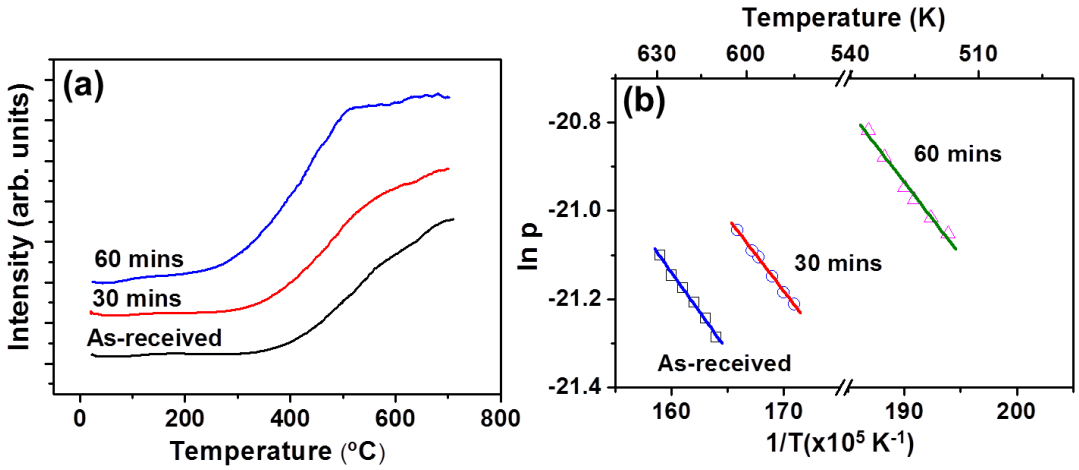


**Figure 4-8.** TPD curves on BTO thin film (a) stoichiometric, after 30 min annealing in vacuum, and after 60 min annealing in vacuum. (b) Plot of ln p versus 1/T corresponding to the onsets of desorption at the low temperature tail of desorption spectra in panel a.

In contrast, after the first anneal of 30 min, the desorption temperature onset decreases to ~320 °C. After a further anneal for 30 min, the desorption onset is ~265 °C, and an additional feature appears just below ~100 °C. The latter can be associated with molecular adsorption of $H_2O$.[Du2012] The intensity of the molecular adsorption of $H_2O$ increases with time presumably occurs after most or all of the chemisorption sites have been saturated. This interesting aspect due to lack of time were not able to further study here.

### 4.3.5 XPS

Figure 4-9(a) shows an XPS survey spectrum for the clean BTO surface. There is a very small amount of surface C contamination. As described in the previous section, the C1s peak was useful to provide an independent calibration of the binding energy scale. The Ba 3d, Ti 2p, and O 1s core-level XPS spectra are shown in Figure 4-9(b)-(d). The high-resolution XPS spectra of Ba $3d_{5/2}$ are shown in Figure 4-9(b). The BEs of the Ba $3d_{5/2}$ components do not shift after exposure to water. The main peak, labeled I, is from the bulk-coordinated Ba. Each spectrum also has a high binding energy (HBE) component labeled II, which is thought to be due to a surface component; however, the exact origin of this peak is a matter of debate. Given the known $TiO_2$ surface termination, it cannot be simply due to under-coordinated surface Ba. As shown in the LEED simulation, the discontinuity in the polarization at the surface creates a surface dipole, giving rise to an effective core level shift. The HBE peaks are very similar before and after water exposure, although the intensity increases a little after water adsorption. This may be correlated to the structural changes observed by LEED I−V and is discussed below.

The XPS spectra of Ti $2p_{3/2}$ are presented in Figure 4-9(c). The spectra before and after exposure to water both have a main component due to Ti with a formal valency of 4+ as in the perovskite structure and a weak, low binding energy (LBE) component corresponding to reduced Ti, often described as $Ti^{3+}$. The latter is known to occur as a result of the formation of oxygen vacancies, Vo. In a simple charge-transfer model, one Vo results in the reduction of two $Ti^{4+}$ ions to $Ti^{3+}$ following the reaction $2Ti^{4+} + O_L \rightarrow Vo + 2Ti^{3+} + 1/2O_2$, where $O_L$ is a lattice oxygen.

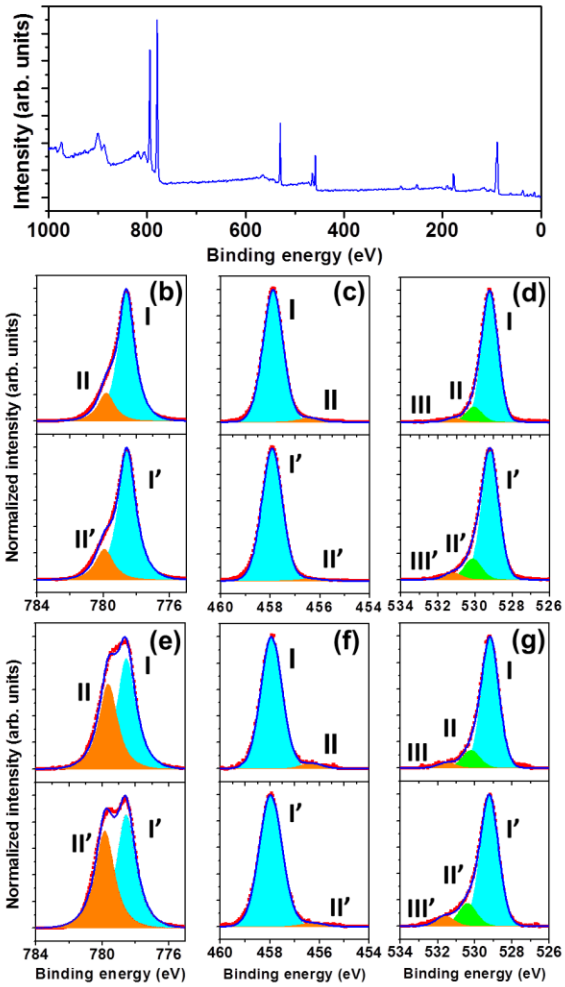


**Figure 4-9.** (a) Survey XPS scan of clean BTO thin film. Core-level spectra for BTO thin film before (top) and after (bottom) water exposure: (b) Ba $3d_{5/2}$, (c) Ti $2p_{3/2}$, and (d) O 1s at normal emission and (e) Ba $3d_{5/2}$, (f) Ti $2p_{3/2}$, and (g) O 1s with a 30° takeoff angle.

Figure 4-9(d) shows the O 1s spectra. The spectrum has three components: peak I with a BE of 529.1 eV, corresponding to oxygen in the perovskite structure,[Baniecki2006] and peaks II (BE 530.3 eV) and III (BE 531.6 eV), hereafter referred to as $O_{II}$ and $O_{III}$. $O_{II}$ is shifted by 1.0 eV with respect to peak I, whereas $O_{III}$ is shifted by 2.4 eV. $O_{III}$ has been ascribed to carbonate or hydroxyl groups chemically bound to surface cations.[Baniecki2006] In our case, the low level of C in the XPS spectra rather leads us to attribute it to $OH^-$ adsorbate species bound to Ti, mainly at the surface. The Pauling electronegativities of hydrogen and Ti are 2.2 and 1.54, respectively, and thus $O_{II}$ may be attributed to a lattice oxygen coordinated with a proton. We note that the expected O 1s shift for molecular water

is greater than 3 eV, which comes from the O atoms of water. [Fuenzalida1999] and thus we do not think that $O_{II}$ and $O_{III}$ are due to molecular $H_2O$.

# 4.4 Discussion

### 4.4.1 Surface chemistry

A careful examination of the Ti and O core level intensities at two takeoff angles before and after exposure to water should allow us to quantify the different adsorption sites. The relative intensities of the Ti $2p_{3/2}$ and O 1s core-level components are given in Table 4-II. Those of $O_{II}$ and $O_{III}$ increase from 11.5 and 3.0 % to 14.0 and 6.1 %, respectively, after water adsorption. If all surface oxygen atoms were involved in adsorption, then, based on a reasonable estimate of the photoelectron inelastic mean free path[NIST] and the layer-by-layer attenuation (see below), we would expect the surface related peaks to account for 38% of the total O 1s intensity. This is clearly not the case and is further evidence of sub-monolayer adsorbate coverage. However, the surface-related oxygen environment is not uniform and has at least two distinct chemical sites. A quantitative analysis of the core-level intensities gives further insight into the changes in surface chemistry on water adsorption.

| | Before | | After | |
|---|---|---|---|---|
| Component | Normal | 30°takeoff angle | Normal | 30°takeoff angle |
| $Ti^{4+}$ | 97.2 | 96.7 | 98.1 | 97.7 |
| $Ti^{3+}$ | 2.8 | 3.3 | 1.9 | 2.3 |
| $O_I$ | 87.1 | 85.5 | 82.4 | 79.9 |
| $O_{II}$ | 10.4 | 11.5 | 13.3 | 14 |
| $O_{III}$ | 2.5 | 3 | 4.3 | 6.1 |

**Table 4-II.** Relative Intensities of the Ti 2p and O 1s Core Level Components before and after Water Adsorption at Normal and 30° Emission

We consider each layer as a homogeneous medium but take into account the layer-by-layer stoichiometry $TiO_2{-}BaO{-}TiO_2{-}$, Letting $I^O$ and $I^{Ti}$ denote the O 1s and Ti 2p intensities from an O and a Ti atom, respectively; this leads to the following expressions for the total O 1s and Ti 2p intensities

$$I_{TOT}(O1s) = I^O \cdot (k + 2)/(1 - k^2)$$

$I_{TOT}(Ti2p) = I^{Ti} /(1 – k^2 )$

where the layer attenuation factor is given by $k = \exp(-c/\lambda \cdot \sin\theta)$, $\lambda$ is the inelastic mean free path, and $\theta$ is the takeoff angle with respect to the sample surface. The $\lambda$ is 1.1 nm calculated using the National Institute of Standards and Technology (NIST) database,[Powell1999]. If the $O_{II}$ and $O_{III}$ peaks were only of surface origin, then the 30° takeoff angle results suggest that 38% of the surface oxygen atoms are coordinated with protons before water adsorption. This estimation rises to 67 % for 90° (normal emission) takeoff angle, which is clearly inconsistent with the 30° takeoff angle results; therefore, we must assume that there are $OH^-$ species already present both at the surface and in the film before water adsorption. Therefore, the film shows evidence of hydroxyl uptake before the adsorption experiment. This agrees with the observations of Wendt et al., [Wendt2005, Wendt2006] who point out the difficulty in obtaining, for example, a pristine $TiO_2$ surface without $OH^-$ species, even under very clean UHV. First-principles results also support high $OH^-$ uptake in BTO.[Geneste2009] Rather than analyzing the absolute values of $O_{II}$ and $O_{III}$ intensities, we have therefore analyzed only the changes in the $O_{II}$ and $O_{III}$ peaks after water adsorption. The underlying assumption is that the changes after water adsorption occur wholly at the surface. The $O_{II}$ intensity as a fraction of the total O 1s signal increases from 11.5 to 14.0 %, whereas the $O_{III}$ intensity doubles from 3.0 to 6.1 % at the 30° takeoff angle, surface sensitive spectra. In the normal emission, bulk-sensitive spectra, the $O_{II}$ and $O_{III}$ increases are 2.9 and 1.8 %, respectively.

Similar considerations can be applied to the $Ti^{4+}/Ti^{3+}$ intensities: the surface-sensitive spectrum has more $Ti^{3+}$ (3.3 %) than the bulk spectrum (2.8 %) and shows a 1.0 % decrease in water adsorption. Water can dissociates at an oxygen vacancy into two hydroxyl species, which are about 0.4 to 0.5 eV lower in energy; that is, $H_2O/BTO + Vo = 2OH^-/BTO + 0.5$ eV.[Wendt2005, Wendt2006] Dissociation near an oxygen vacancy transfers a proton to an adjacent O atom, forming two $OH^-$ pairs, one of which can fill the Vo, the other appearing at an adjacent lattice oxygen site. However, a different process, $OH^-$ on-top bonding at a surface Ti site is also energetically favorable.[Geneste2009] We must therefore consider two possible dissociative adsorption processes: filling a lattice oxygen vacancy giving rise to $O_{II}$ and bonding to on-top lattice Ti ($O_{III}$), as shown in Figure 4-10.

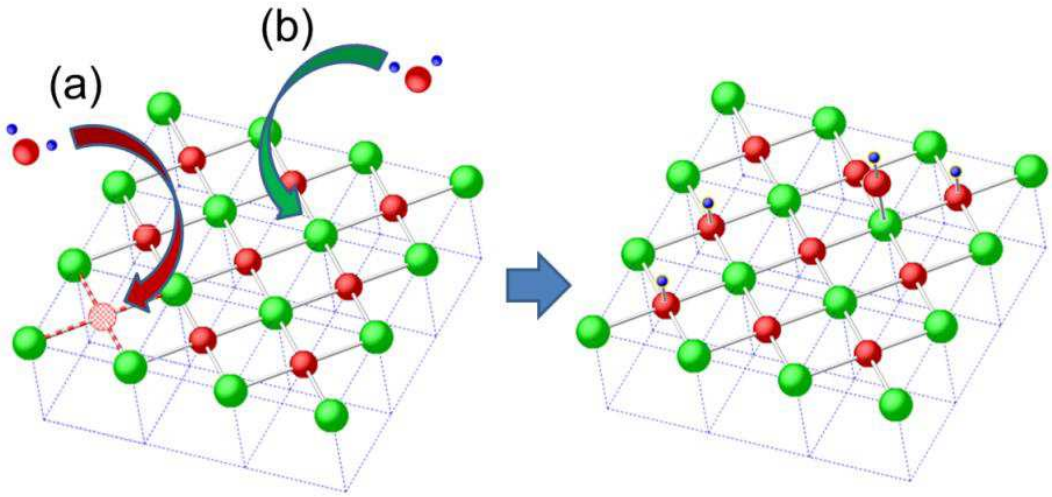


**Figure 4-10.** Schematic diagram showing the two adsorption processes leading to chemisorbed $OH^-$ at the surface of $TiO_2$-terminated BTO, either at a vacant lattice oxygen site or on-top of a surface Ti. The smaller (red) atoms are O, and the larger (green) atoms are Ti.

To quantify the relative importance of the two sites in the present experiment, we assume that the intensity changes observed after exposure to $H_2O$ occur only at the surface. The change in the $Ti^{3+}$ intensity in the 30° takeoff angle spectrum corresponds to 2.0 % of the surface Ti signal. This implies that a surface Vo concentration of 0.5 % (calculated with respect to the number of surface oxygens) is filled by the water adsorption. From the change in the $O_{II}$ intensity, the proportion of proton coordinated surface lattice oxygen due to water adsorption is 6.6 %, which, following the dissociative model of Wendt,[Wendt2006] corresponds to a 3.3 % Vo concentration filled by adsorption, more than six times that estimated from the $Ti^{3+}$ intensity change. The $O_{III}$ increase, ascribed to Ti-$OH^-$ adsorption, corresponds to 8.2 % of the total surface oxygen signal, suggesting that 16.4 % of the surface Ti atoms are coordinated to $OH^-$ groups after water adsorption.

The same analysis of the bulk-sensitive spectra puts this figure at 16.7 % which is remarkable close to the surface-sensitive figure. For each $OH^-$-Ti, there can also be one extra lattice oxygen bound to a proton if all $H^+$ bond to the surface, that is, up to 8.2 % more surface lattice oxygen in an $OH^-$ environment. This figure is much closer to the 6.6 % lattice oxygen in an $OH^-$ environment deduced from the change in the $O_{II}$ peak intensity. The difference could be due to possible hydride diffusion, which transfers two electrons to the neighboring titanium atoms and then

diffuses as a proton.[Kobayashi2012] Thus, both the bulk and surface-sensitive spectra give the same estimation of $OH^-$-Ti and a consistent number of surface lattice oxygen atoms in an $OH^-$ environment.

Some of the absolute intensity changes are, of course, very small and they are obscure with respect to a high background; however, they do fit with a model of a dominant dissociative process giving rise to $OH^-$ chemically bonded on top to surface Ti atoms.

### 4.4.2 Adsorption/Desorption process

Annealing at the end of each TPD cycle creates more Vo, therefore, the marked differences in TPD spectra give a further indication of the importance of Vo for $H_2O$ adsorption on the BTO surface. A continuous decrease in desorption temperature with increasing Vo concentration (and hence $OH^-$ coverage) can be interpreted as second-order desorption kinetics with a constant activation energy, or as first-order or second-order kinetics with a coverage-dependent activation energy.[Redhead1962] To distinguish these cases, we present a plot of ln p (pressure) versus 1/T extracted from the low-temperature onset of desorption in Figure 4-8(b). Following the method of ref [Habenschaden1984], where a linear heating $T=T_0+\beta t$ is assumed. Then one has

$$\frac{d\ln p}{d\ (1/T)} = -\frac{E}{R} + \frac{d\ln(\upsilon/\beta)}{d\ (1/T)} + \frac{d\ln n_{ad}}{d\ (1/T)}$$

where p is the pressure measured in the desoption experiment and υ is the preexponential. If υ is independent of coverage, there is a linear relation beween ln p and 1/T.

In Figure 4-8(b), the linear relation holds for all cases, and the lines are parallel to each other, indicating a constant desorption energy. The slope of the ln p versus 1/T is $E_{des}/R$, where $E_{des}$ is the desorption energy and R is the ideal gas constant. The activation/desorption energy deduced from the main TPD onset the same for all surfaces, suggesting that the chemisorption sites are the same. First-order desorption kinetics are often associated with molecules adsorbed in a molecular state, whereas second order kinetics are more consistent with molecules that have undergone dissociative chemisorption.[Garra2009] Therefore, a likely scenario is

that the main desorption is second-order with a constant activation energy. The decrease in the desorption onset with Vo concentration could be due to the higher probability of recombination of $OH^-$ and a neighboring proton. Vo creation makes the surface more positively charged for physisorption, and thus a higher concentration of $OH^-$ ions may chemically bond to the surface releasing $H^+$, which can also bond to surface lattice oxygen. The probability of surface recombination should therefore increase.

### 4.4.3 Surface structure

As shown in Figure 4-7(a), the average polarization over the first two unit cells before water adsorption is $P^+$, pointing vertically toward the surface. However, the rumpled top $TiO_2$ layer has a downward pointing electric dipole, opposite to that of the bulk polarization. This is evidence that to stabilize polarization in the thin film, the first $TiO_2$ atomic layer corrugates and creates a dipole opposite to the bulk polarization to compensate the ionic surface polarization charge. Such an inversion of the electric dipole at the surface has already been observed using LEED I−V for an ultrathin, BaO-terminated $P^+$ polarized BTO film grown on $SrRuO_3$.[Shin2009] After water exposure, the adsorption of $OH^-$ at on-top Ti surface atom sites appears to switch the dipole of the surface $TiO_2$ layer back in the direction of the bulk polarization. Thus, similar to the case of PTO, $OH^-$ stabilizes the $P^+$ polarization state.[Fong2006]

Figure 4-11 is a plot of the R factor as a function of $OH^-$ (considered as on-top oxygen) coverage in the top layer adsorption sites. The best fit (R factor of 0.25) is obtained for an $OH^-$ coverage of 0.2; that is, one in five surface Ti atoms form chemical bonds with on-top $OH^-$. This agrees very well with the 16.4−16.7 % $OH^-$-Ti coverage deduced from the XPS intensities. The LEED I−V simulation in Figure 4-6(b) was, in fact, done for 0.2 oxygen coverage at on-top Ti sites. The Ti-$OH^-$ distance obtained in the simulation is 1.88 Å, which is virtually identical to the GGA and LDA predicted distance.[Geneste2009]

In the structure presented in Figure 4-7(b), polar inversion is observed in both the first and the second atomic layers, with Ti moving outward and Ba inward with respect to the ionic rumpling observed before water adsorption. From the surface

structure parameters in Table 4-I, the polar inversion is accompanied by significant distortion of the third (TiO-3) atomic layer, with Ti moving outward and O inward.

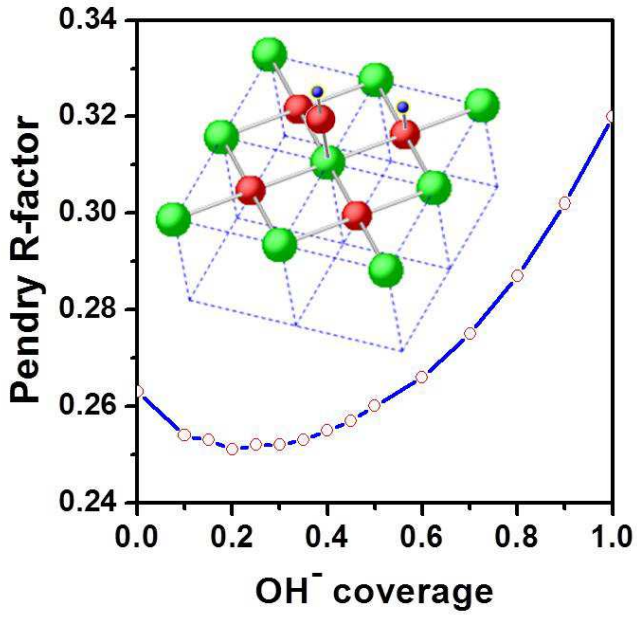


**Figure 4-11.** Pendry R-factor as a function of $OH^-$ coverage of the surface at on-top chemisorption on surface Ti atoms (center of inset). Atoms coded as in Figure 4-7.

Thus, water adsorption on the surface modifies the ionic positions of the surface and subsurface layers. The presence of extra negative charge from the $OH^-$ groups allows the $TiO_2$ top layer to switch its dipole back in the same direction as the bulk $P^+$ state. The screening due to the dissociative adsorption of water and the chemisorption of $OH^-$ therefore appears to be more efficient than the ionic rumpling of the dry surface. The rumpling inversion observed for the second atomic layer (BaO-2) creates a downward pointing subsurface dipole and may be the way the system completes screening of the positive surface charge in the $P^+$ polarization state. If this is the case, then one would expect that higher $OH^-$ surface coverage would reduce or switch back the dipole in the direction of the bulk polarization. By the third layer, the direction of polar distortion is the same as that of the bulk $P^+$ state. A high concentration of $OH^-$ can even provoke a cubic phase in BTO;[Choi1999] however, from our simulation of LEED I−V, this is not the case. Rather the $OH^-$ chemisorption from dissociative water screens the surface polarization charge rather than changing the bulk film structure. The optimized

structures obtained from the LEED I−V simulations also shed light on the nature of the HBE peak in the $Ba3d_{5/2}$ XPS spectra.

The polar inversion of the BaO-2 rumpling after $H_2O$ adsorption will necessarily modify the electronic environment of the near surface, second-layer Ba ions with respect to the bulk, and this may be responsible for the observed core level shift, even though the Ba ions remain fully coordinated. It has been shown that dynamical charge transfer is more relevant for deformed polar materials like ferroelectrics,[Ghosez1998, Wang2011] and given the modifications observed in the surface structure, we expect this to play an important role in determining the surface related BEs. However, this is, for the moment, only speculation and needs to be confined by, for example, first principle calculation.

The structural, chemical and energetic analysis has shown that: (i) $H_2O$ undergoes mainly dissociative adsorption on the polarized BTO(001) surface; (ii) there are two competing sites for dissociative adsorption (Vo and on-top Ti lattice atoms); (iii) adsorption oxidizes surface $Ti^{3+}$ ions; (iv) the on-top surface Ti is the dominant $OH^-$ chemisorption site; and (v) the concentration of Vo favors initial physisorption. Some open questions remain. Our analysis is based on the differences between a slightly defective single domain, epitaxially strained BTO film before and after a controlled water adsorption experiment. The presence of adsorbate-related $O_{II}$ and $O_{III}$ components in the XPS spectra of the as-received sample show that $OH^-$ units are already present, either at the surface or in the bulk of the film. This $OH^-$ incorporation could occur during film growth but may also be due to uptake of residual hydrogen in UHV. More efforts are certainly needed to optimize the control of growth and analysis conditions, for example, the as grown films still show signal from $Ti^{3+}$. Notwithstanding these problems, we have demonstrated the extreme sensitivity of the surface polarization state to controlled water exposure. Physisorption is enhanced by higher Vo concentration, whereas preferential $OH^-$ chemisorption occurs at on-top surface Ti sites. The $H_2$ yield of the dissociation process also needs to be quantified. Similar experiments on a single $P^-$ domain, known to be favored by Vo,[Fong2006] should also be carried out.

## 4.5 $BaTiO_3$ thin films with different strains

### 4.5.1 Surface structure and surface chemistry

In order to understand the influence of strain on water adsorption, 3 BTO samples with differents thickness (8, 15 and 30 nm) were fabricated by MBE. The growth of the BTO films were monitored by in situ RHEED, which allowed a precise control of the number of atomic layers. At the desired thickness (8, 15 and 30 nm), the Ba source was switched off, ensuring deposition of a $TiO_2$ last layer. The BTO lattice constants measured by XRD as a function of thickness are shown in Figure 4-12. For the 8 nm film the in-plane lattice constant is the same as that of the STO substrate indicating that the film is fully strained (2.2 %) whereas the in-plane lattice constant for the 30 nm is close to that of bulk BTO with a residual strain of only 0.2 %. The out-of-plane tensile strain is also a maximum for the 8 nm film (3.6 %), again approaching 0.2 % for the 30 nm film. These results are consistent with previous studies on epitaxial BTO films which start to relax above 8 nm.[Niu2012] Figure 4-12 also shows the tetragonality, c/a as calculated from the XRD results.

The average film ferroelectric polarization can be estimated using the data of Kim et al.[Kim2005] to be 30, 40, 45 $\mu C/cm^2$ as shown in Figure 4-13 for the 8, 15 and 30 nm films, respectively.

LEED patterns for the 30-nm-thick and 15-nm-thick BTO(001) before and after $3.6 \times 10^5$ L $H_2O$ exposure are presented in Figure 4-14(a)(c) and (b)(d), respectively. The sharp (1 × 1) LEED pattern in Figure 4-14(a) and (c) shows the square structure of the BTO surface. After $H_2O$ exposition, LEED patterns like that shown in Figure 4-14(b) and (d) were obtained. The symmetry is the same but spot and background intensities change as on 8 nm film. We can therefore rule out the formation of an ice structure or multiple disordered water layers for all thicknesses,[Henderson2002, Thiel1987] and we deduce that at most a single-ordered $H_2O$ layer is adsorbed epitaxially on the clean BTO surface as shown for the 8 nm BTO film in section 4.3.

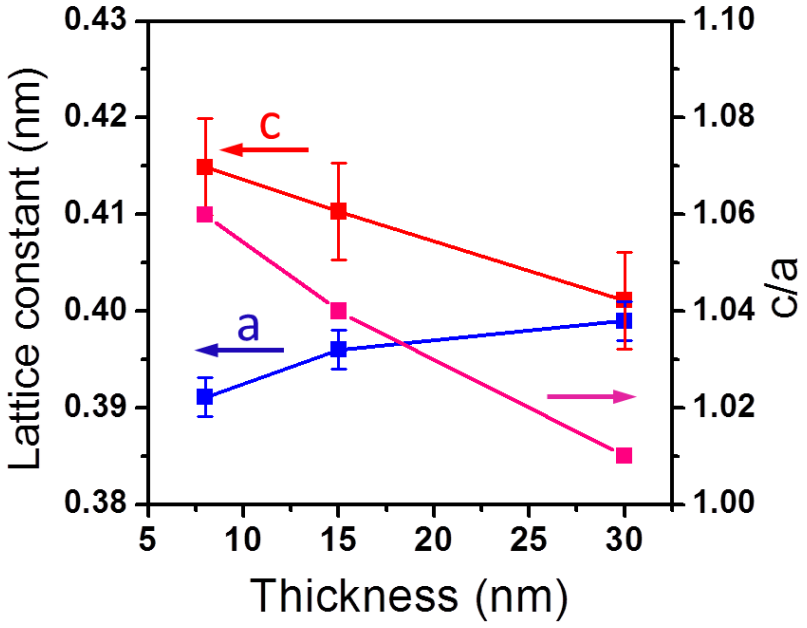


**Figure 4-12.** Lattice constants of a (blue), c (red) and c/a ratios (pink) on BTO films with different thicknesses measured by XRD.

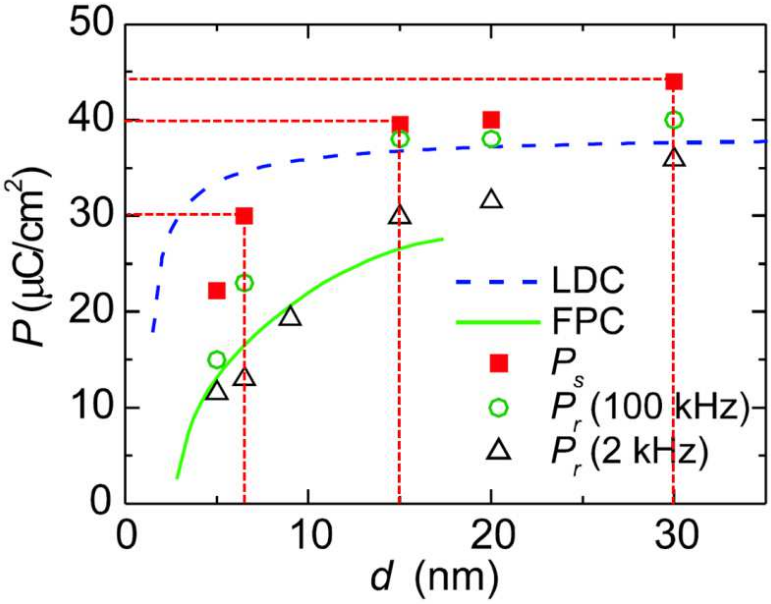


**Figure 4-13.** The remnant polarization ($P_r$) and spontaneous polarization ($P_s$) values obtained from pulse measurements, first principles calculation (FPC), and Landau-Devonshire calculation (LDC). (This figure is reproduced from reference [Kim2005].)

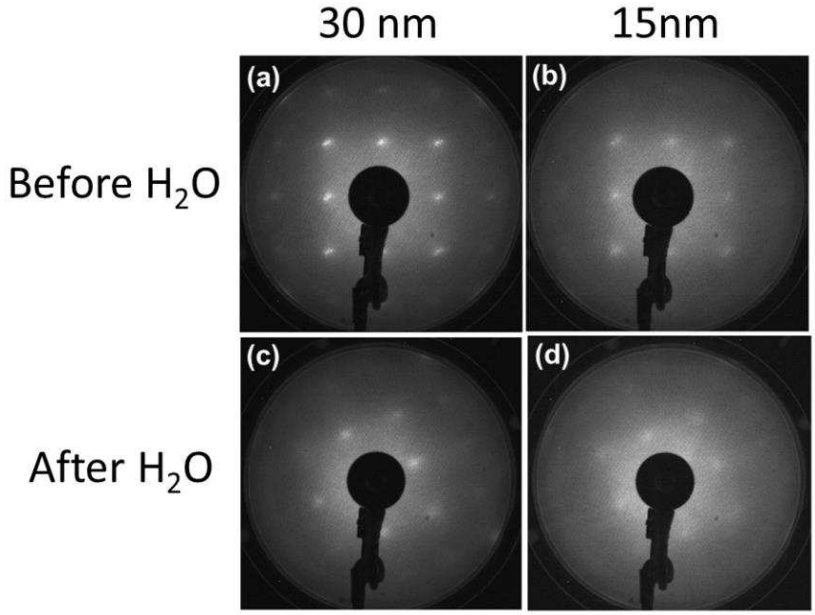


**Figure 4-14.** LEED image on 30-nm-thick and 15-nm-thick BTO surfaces at 130 eV (a) (c) before and (b) (d) after water exposure.

Figure 4-15 shows the normal emission XPS spectra on the surfaces of BTO thin films with different thickness before and after exposure to water. As the case of the 8 nm BTO film, the binding energies (BE) of the Ba $3d_{5/2}$ components do not shift after exposure to water. This is not surprising since the film is $TiO_2$ terminated. The main peak, labeled I, is from the bulk-coordinated barium. Each spectrum also has a high binding energy (HBE) component labeled II, which from the angle-resolved measurements is a surface related component although not certainly due to atom at the surface layer.

Although we have not done LEED I-V on the 15 and 30 nm BTO film, the quantitative LEED I-V on the 8 nm BTO film suggests that it can be interpreted as the result of the electrical boundary conditions induced by the surface rumpling of the $TiO_2$ termination layer as described in section 3.3. In other words, this surface component is not due to Ba with lower O coordination nor to Ba with different chemistry but rather to the different electronic environment due mainly to the increased rumpling in the surface $TiO_2$ layer, i.e. the 2nd and 3rd nearest neighbours of the subsurface Ba atoms.

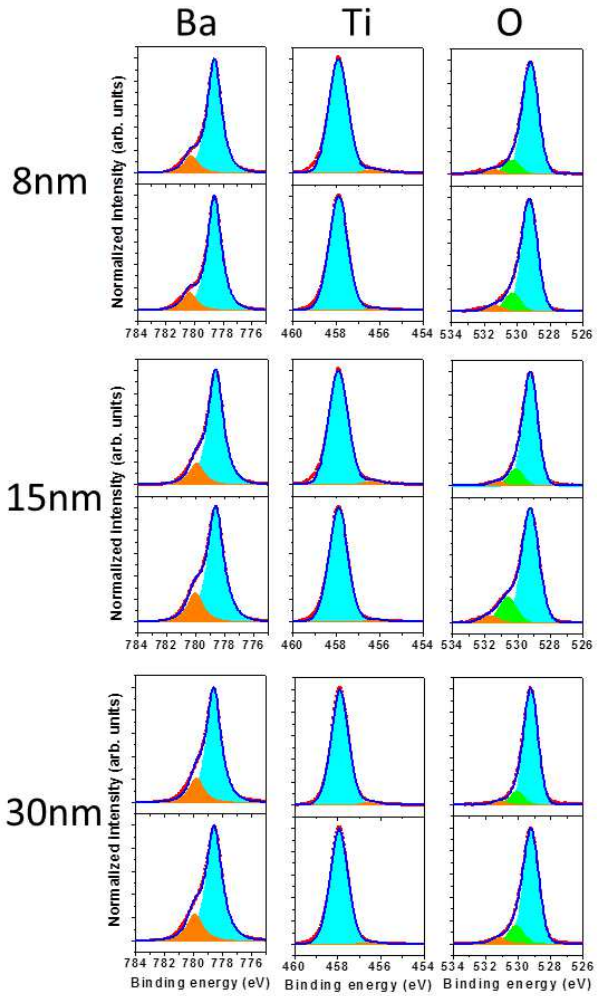


**Figure 4-15.** XPS core level spectra on BTO thin film with different thickness before (top) and after (bottom) water exposure.

The O 1s spectra have three components, peak I has a BE of 529.1 eV, corresponding to oxygen in the bulk perovskite structure[Baniecki2006], as well as peaks II (BE 530.3 eV) and III (BE 531.6 eV) referred to as $O_{II}$ and $O_{III}$. XPS has shown that the $O_{II}$ component is due to a lattice oxygen coordinated with a proton and the $O_{III}$ component is due to an $OH^-$ group bonding.

The XPS spectra of Ti $2p_{3/2}$ for all the three films are also presented in Figure 4-15. The three films before exposure to water have identical spectra, a main component due to Ti with a formal valency of 4+ as in the perovskite structure, and a weak, low binding energy (LBE) component corresponding to reduced Ti. Using the attenuation model presented in section 3.3, the intensity of this peak is far too

low to be associated with the surface environment of all the surface Ti atoms. Instead, it is due to charge transfer from an oxygen vacancy, reducing two $Ti^{4+}$ ions to $Ti^{3+}$. 3.5 % of the Ti ions are in the $Ti^{3+}$ state for all films, decreasing to 2.5 % after water adsorption. We therefore conclude that the $OH^-$ groups bond mainly on-top to surface Ti atoms as predicted by theory.[Geneste2009] The similarity between the three films excludes significant stoichiometry effects on chemisorption, therefore we conclude that any variation in adsorption energies is likely to be due to strain induced atomic distortion and bulk film polarization.

### 4.5.2 Adsorption/Desorption process

TPD spectra of the three films, using mass-to-charge ratio (m/e) =18, are presented in Figure 4-16. The backgrounds have been removed corresponding to the zero $H_2O$ desorption rate, and then we can get the desorption energy from a plot of ln p (pressure) versus 1/T extracted from the low-temperature onset of desorption. The instrument was calibrated by sending $O_2$ and $H_2O$ pulses of known volume (6.05 $cm^3$) and pressure (continuously controlled using a MKS Baratron capacitance manometer, 10 Torr full scale) through a variable micro-leak (Edwards LV10K). This system allowed to check for MS response linearity and to calibrate directly in $H_2O$ or $O_2$ rate (µmol/s). After each experiment, the MS sensitivity was checked by using $O_2$ pulses and corrected if necessary. Signal originating from residual water in the system was determined after pressure equilibrium between MS and TPD reactor at room temperature. The corresponding value, supposed as constant, was subtracted to the $H_2O$ signal over the whole TPD range. The spectra are acquired from room temperature to 700 °C.

From the TPD measurements we can conclude that the desorption energies of water on BTO(001) are affected by the strain state. The high strain-induced distortion of the thinnest sample also has the lowest film polarization.[Kim2005] the magnitude of the film polarization depends on the strain, thus film thickness. The desorption energy may therefore also be related to differences in film polarization.[Jo2006] The mechanism behind this effect can be considered from either an atomistic or a continuum perspective.[Garra2009] From the atomistic perspective, differences in the surface atomic structure of different strains must be considered. As we have shown for the 8 nm BTO film, in order to stabilize

polarization in the thin film, the first $TiO_2$ atomic layer corrugates and creates a dipole opposite to the bulk polarization to compensate the surface polarization charge. It has been shown that this dipole varies with strain.[Fechner2008] From the continuum perspective, the BTO samples can be seen as polarized dielectric slab in which the surface polarization charge may be screened by electrons and holes or by structural changes, in this case, surface rumpling. Thus, the electrostatic fields caused by different strains at the surface may influence the geometry and strength of adsorbate-surface interactions. The experimental strain dependence of the desorption energy is reported in Table 4-III together with the corresponding film polarization estimated from Ref.[Kim2005] as in Figure 4-13.

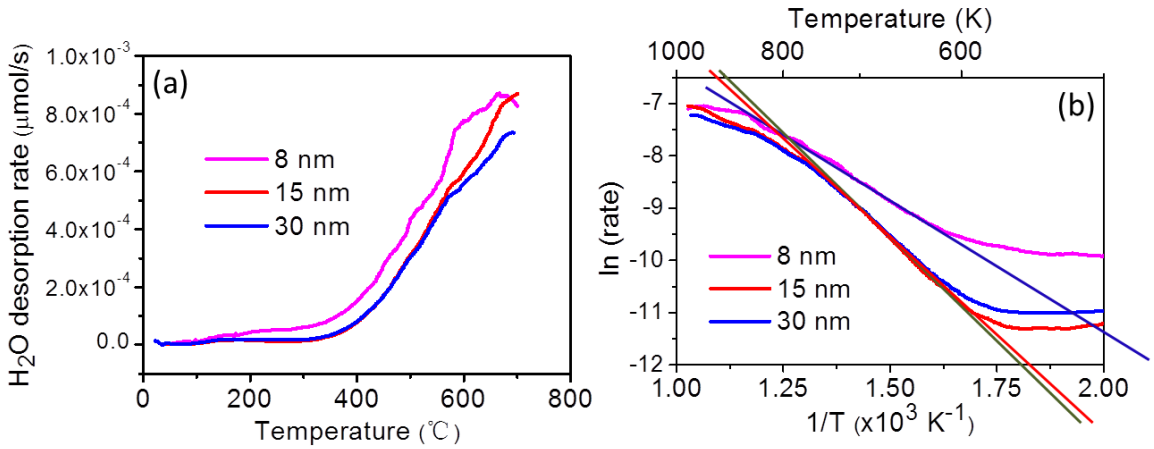


**Figure 4-16.** TPD spectra on (a) BTO thin films with different thickness, and (b) Plot of ln (rate) versus 1/T corresponding to the onsets of desorption at the low temperature tail of desorption spectra in (a)

In section 3.3, using low energy electron diffraction intensity versus voltage (LEED I-V), we have characterized 8-nm-thick $BaTiO_3$ films, grown using MBE with fully compressive strain on a $SrTiO_3$ substrate. LEED I-V reveals a monodomain vertically polarized along [001] direction. As mentioned before, the signal in the low temperature range is higher for the desorption spectrum of 8 nm BTO. The higher bulk film polarization in the thicker films favours water adsorption because it screens more efficiently the depolarizing field. The higher film polarization provides a deeper initial potential well for physisorbed molecular water, increasing the probability of dissociation and chemical bonding. The lower ferroelectric polarization on 8-nm-thick BTO (30 $\mu C/cm^2$) produces a weaker interaction between $H_2O$ and 8-nm-thick BTO surface. Thus $H_2O$ desorption starts

at lower temperature, where a small increase in the TPD is observed for the whole spectrum of 8 nm BTO.

| **Thickness (nm)** | **In-plane strain (%)** | **Apparent Desorption Energy (eV)** | **Estimated polarization ($\mu C/cm^2$)** |
|---|---|---|---|
| **8** | **2.2** | **0.46** | **30** |
| **15** | **0.9** | **0.67** | **40** |
| **30** | **0.2** | **0.63** | **45** |

**Table 4-III.** Measured in-plane strain and water desorption energy, and estimated film polarization, as a function of film thickness.

TPD spectra of the 15 and 30 nm films, are presented as a function of annealing time in vacuum in Figure 4-17 and Figure 4-18, respectively. The linear parts of the spectra are parallel to each other, as in the case of 8-nm-thick BTO for short annealing time (0 and 30 minutes). However, the slope of the spectra decreases with long annealing time (60 and 90 minutes), indicating a decrease in desorption energy. Since $H_2O$ prefers to dissociate at oxygen vacancy site, more vacancies result in more $OH^-$ and $H^+$ on BTO surface, which makes a $OH^-$ meets a $H^+$ more easily. A decrease in desorption temperature with increasing Vo concentration and hence $OH^-$ coverage can indeed be interpreted as second-order desorption kinetics with a changing activation energy.[Redhead1962]

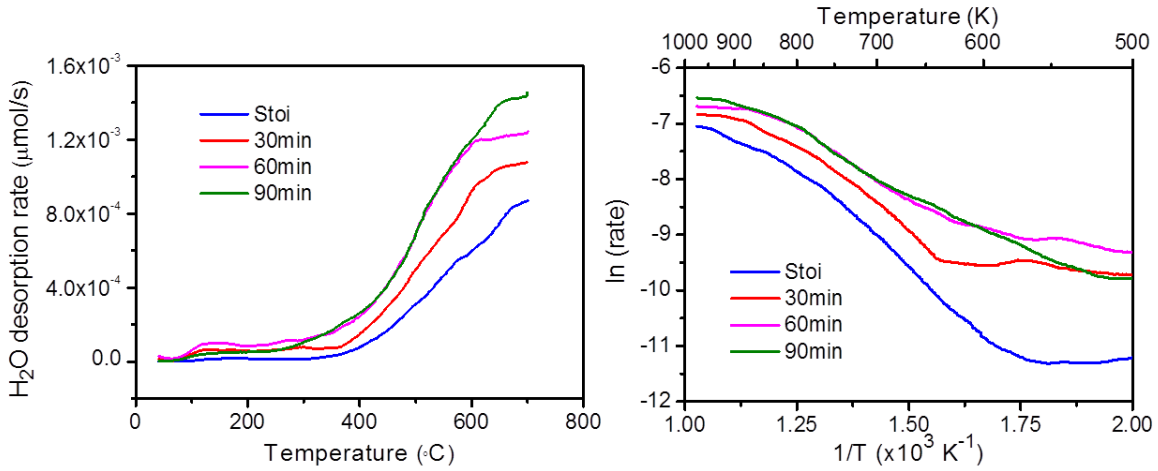


**Figure 4-17.** TPD spectra on 15nm BTO (a) annealed with different time (b) Plot of ln (rate) versus 1/T corresponding to the onsets of desorption at the low temperature tail of desorption spectra in (a)

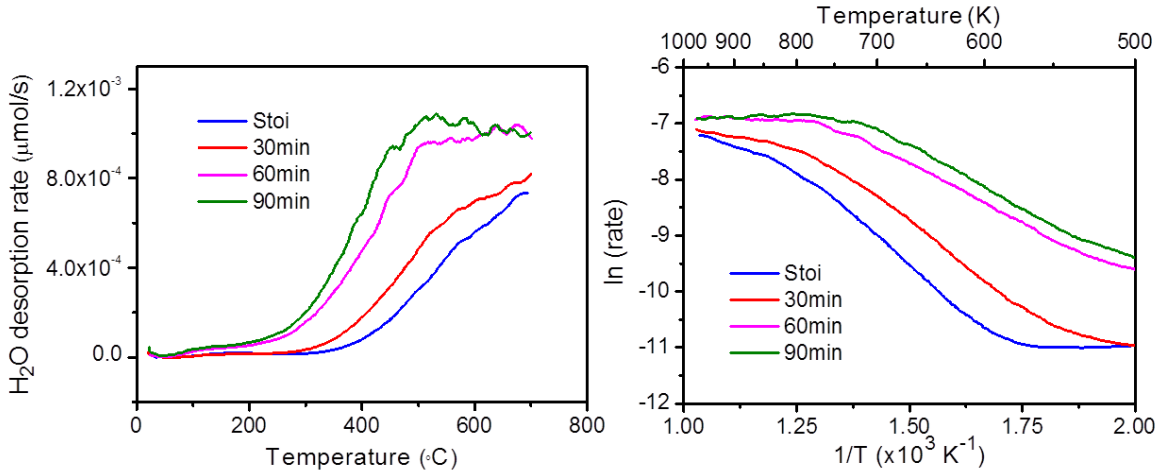


**Figure 4-18.** TPD spectra on 30nm BTO (a) annealed with different time (b) Plot of ln (rate) versus 1/T corresponding to the onsets of desorption at the low temperature tail of desorption spectra in (a)

## 4.6 Conclusions

We have firstly studied the surface structure of a compressively strained BTO(001) thin film before and after exposure to $H_2O$ by using XPS, temperature-programed desorption spectroscopy, and low energy electron diffraction intensity versus voltage analysis. The BTO film as-received has a $P^+$ polarization. The initial physisorption of molecular water is enhanced by a high Vo surface concentration,

creating a more positively charged surface. There are two dissociative adsorption sites, oxygen vacancies and on-top surface Ti. The predominance of dissociative adsorption is confirmed by both XPS and TPD. The on-top $OH^{-}$-Ti dominates the chemisorption process. Before water adsorption, the polarization discontinuity at the surface reverses the rumpling in the $TiO_2$ termination layer. After water adsorption, dissociation gives rise to $OH^{-}$-Ti chemical bonding at 16 to 20 % of the surface Ti sites. Adsorbate screening is more efficient than ionic rumpling and switches the ionic rumpling in the $TiO_2$ layer to the same direction as in the bulk $P^{+}$ state, but the first BaO layer shows polar inversion with respect to the bulk displacements.

Then we have studied the adsorption of $H_2O$ on $TiO_2$-terminated $BaTiO_3$ (001) epitaxially strained films of different thickness. The predominance of dissociative adsorption is confirmed by both XPS and TPD. The on-top $OH^{-}$-Ti dominates the chemisorption process. The desorption energy of water increases with the increasing film thickness. The thickness dependence of the desorption energy is discussed in terms of both strain and bulk film polarization.

Finally, the desorption energy of water are presented as a function of oxygen vacancy concentration (annealing time in vacuum). The desorption energy increases with the increasing film thickness due to film polarization.

# Chapter 5

# X-ray photoelectron diffraction study of relaxation and rumpling of ferroelectric domains in $BaTiO_3$ (001)

## 5.1 Introduction

The surface of a ferroelectric (FE) may show a net fixed polarization charge which is intrinsically unstable due to the well-known polar catastrophe. [Goniakowski2008] The presence of unscreened surface charge creates an internal electric field, the depolarizing field, which can partially or wholly cancel the polarization inside the material. Thus, the electrical boundary conditions can determine the ferroelectric state. The surface polarization charge can be screened by a variety of mechanisms including adsorbate species,[Spanier2006, Krug2010] intrinsic defects,[Jia2004] free charge carriers, surface and near surface structural changes (rumpling, relaxation and reconstruction) and domain ordering.[Merz1954] The latter reduces the energy of the system by screening the depolarizing field through ordering of the FE domains with antiparallel dipole moments. [Shimada2010] The depolarizing field in one domain is screened by the electric fields of adjacent domains. However, such screening is usually imperfect. In the absence of significant adsorbates or free charge carriers, intrinsic defects and structural changes may combine with domain ordering to minimize the energy of the system and strongly influence its FE properties.[Cai2005]

In this chapter we study how the microscopic screening mechanisms may combine with domain ordering to determine ferroelectric stability.

Surface structural modifications have been the subject of theoretical studies. [Padilla1997, Fechner2008, Meyer2001] Following Meyer and Vanderbilt [Meyer2001] relaxation is given by the average atomic displacement, $\beta = [\delta_z(M) + \delta_z(O)] /2$, where $\delta_z$ (M) and $\delta_z$ (O) are the displacements of the Ba or Ti ions and the oxygen ions, respectively, from the bulk positions. The change in the interlayer

spacing, $\Delta d_{ij}$, is the difference in the average atomic displacements for two adjacent layers $\beta_i$ and $\beta_j$. The intra-layer corrugation or rumpling is defined as $\eta = [\delta_z (M) - \delta_z (O)] /2$. The surface plane is indexed i=1.

Experimentally probing such surfaces requires a structural tool sensitive to local atomic positions and to surface chemistry. One experimental study of the atomic rumpling and relaxation for $P^+$ polarization in a thin film has been published using low energy electron diffraction (LEED).[Shin2008] As descried in chapter 3, XPD combines such chemical sensitivity with quantitative information on the local atomic structure around each emitting atom (Figure 5-2).[Osterwalder1991] In comparison to LEED, XPD has the elemental sensitivity of photoemission. However, few XPD studies of FE oxides have appeared in the literature. Schneider et al. performed an early study of perovskite oxides using forward focusing [Schneider1998]. Berlich et al. have investigated the surface chemistry of paraelectric BTO,[Berlich2011] while Despont et al. have published a high resolution XPD and XRD study of the FE distortion in a PTO thin film. [Despont2006] By using synchrotron radiation the kinetic energy of the photoelectrons can be tuned so as to favor the more bulk-sensitive, forward scattering or the more surface sensitive, multiple scattering regimes. [Winkelmann2008]

## 5.2 Experimental and theoretical methods

### 5.2.1 Experiment

The sample was a 7.5 × 7.5 $mm^2$ BTO(001) single-crystal furnished by MaTecK GmbH. Figure 5-1 shows an AFM topography image of the (001) surface after annealing at 900 °C in $O_2$ with a flow rate of 5 l/min for three hours. Wide, flat terraces with mainly 0.4 nm step heights are observed, indicating a single surface termination.

The XPD experiments were carried out at the Antares beamline, Synchrotron Soleil (Saint Aubin). The sample was ozone cleaned ex-situ for one hour before introduction into the vacuum system. To remove surface carbonates, our experiment has shown that ozone treatments are preferable. It was then annealed in-situ in $O_2$ ($2 \times 10^{-4}$ Pa) for several hours to remove residual organic contaminations

on the surface. The base pressure of the system was better than $3 \times 10^{-8}$ Pa. BTO has a ~3.2 eV band gap rendering it difficult for x-ray photoelectron spectroscopy experiments due to charging. To overcome this problem the sample was annealed in UHV at 740 °C for one hour. This procedure created oxygen vacancies[Hirata1994, Kuwabara1997] increasing the sample conductivity. The inset of Figure 5-4 shows a typical LEED (1 × 1) pattern for BTO(001) single crystal after annealing. The LEED has four-fold symmetry, therefore the experimental azimuthal angular range guarantees that all diffracting structures were measured and that symmetrization of the data set could be used to plot the XPD patterns over 2π. Thus whatever the preparation of in-plane polarization, this actually makes it certain that $P^{in} = (P_x + P_{-x} + P_y + P_{-y})/4$, a key part in the data analysis.

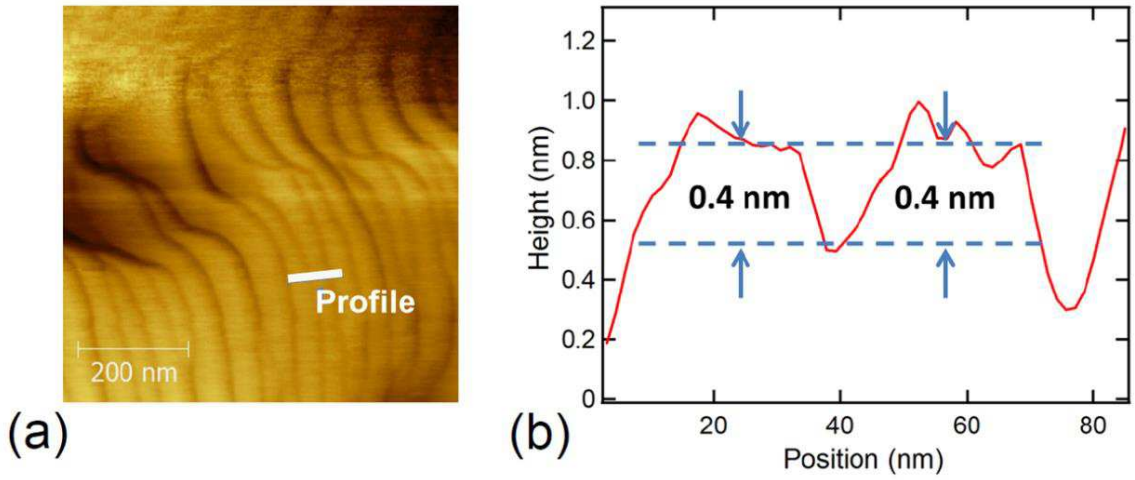


**Figure 5-1.** (a) AFM topography image of BTO(001) surface after annealing at 900 °C in 1 atmosphere of $O_2$ with a flow rate of 5 l/min for three hours, (b) line profiles showing the appearance to one unit cell steps after annealing in oxygen.

An electrostatic hemispherical analyzer (Scienta 4000) was used allowing simultaneous detection of emitted electrons over a wide angular range without tilting of the sample. All the data were normalized by the background to each spectrum in the XPD pattern. The 700 eV photon energy was chosen to increase surface sensitivity and to ensure that the XPD data included multiple scattering. Angle scanned XPD patterns were measured over a part of the hemisphere above the sample surface: Ba 4d, Ti 2p and O 1s core-level photoelectron intensities were collected for polar emission angles from 11° to 69° (surface sensitive) and an

azimuthal sector of more than 90°. The azimuthal angle was scanned in steps of 1°. For each value of the azimuthal angle three fixed polar angles were measured. The analyzer has a polar acceptance of ~25° and the overall analyzer angular resolution is better than 0.2°. Using 700 eV photon energy the kinetic energy for Ba $4d_{5/2}$ (610 eV), Ti $2p_{3/2}$ (240 eV) and O 1s (170 eV) gives inelastic mean free path values of 18.2 Å, 9.5 Å, and 6.9 Å, respectively.[Tanuma1994] The overall energy resolution (beamline and spectrometer) was 0.25 eV. All measurements were done at room temperature.

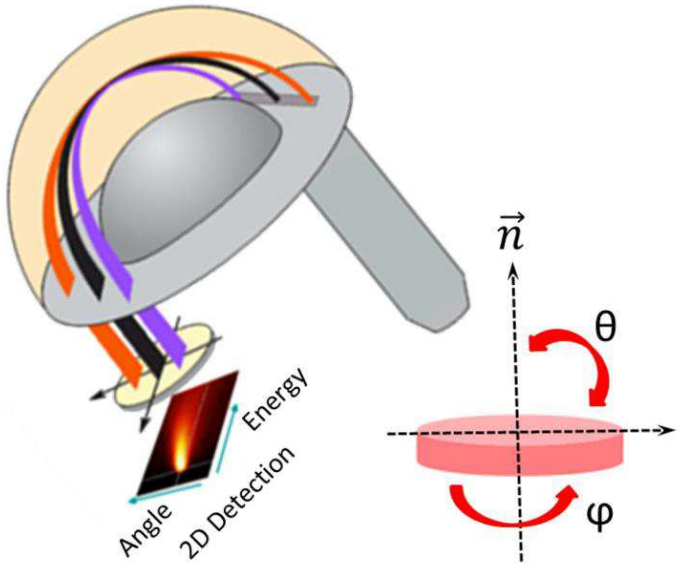


**Figure 5-2.** XPD measurement using 2D detector.

### 5.2.2 Theory

XPD simulations of the BTO(001) surface are complex due to the large parameter space. In this thesis, the surface termination, BaO or $TiO_2$, and different polarization directions, $P^+$, $P^-$ and $P^{in\text{-}plane}$, are tested, with a view to understanding inter-planar relaxation in the surface region and surface rumpling. We have adopted a simulation strategy which allows testing in parallel of the surface rumpling and relaxation, the surface termination as well as the weight of different polarities. The best simulation is then obtained by combining the two final solutions in a last iteration.

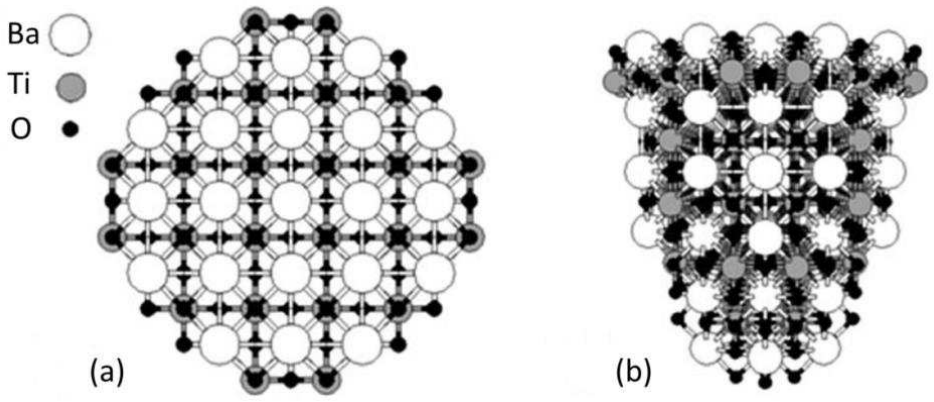


**Figure 5-3.** 430 atom cluster of the BTO(001) surface with surface termination BaO used for simulation of the XPD anisotropy: (a) top view and (b) lateral view. Black color corresponds to oxygen atoms, white to barium atoms, and gray to titanium atoms.

The XPD simulations were done by Dr. A. Pancotti using the cluster model approach of the MSCD code[Chen1998] based on the muffin-tin potential approximation. Two paraboloidal clusters were used. The first one had a surface radius of 22 Å and a depth of 10 Å and contained 900 atoms. It was used to investigate changes in the inter-planar distances and surface rumpling, starting from the unrelaxed surface of the bulk structure. The second one was used for the final simulation of the experimental result, including not only the surface relaxation but also bulk photoelectron diffraction. This cluster has 430 atoms, a depth of 25 Å, and radius 12 Å, sufficiently large to ensure convergence of the scattering calculation and to avoid cluster border effects. In Figure 5-3 we show the second cluster with, in this case, a BaO-terminated BTO(001) surface. There are thus five emitting layers in the final cluster, which proved sufficient to simulate the XPD pattern. The structure is comparable to the cluster in literature, eg. Cu(111) reported by Despont et. al. [Despont2006] Additional emitters did not improve significantly the results.

In order to account for surface relaxation, we allowed atoms of two outermost surface layers to relax along the z axis. We then extended relaxation to the third to fifth subsurface layers. Atoms are fixed at their lateral bulk positions and allowed to relax in the z direction. The structure is determined in a fit procedure that searches for the set of parameters that optimizes the agreement between the theoretical and experimental diffraction curves, through minimization of the

reliability factor Ra, defined as the difference between the experimental and the simulated diffraction patterns,[Chen1998]

$$R_a = \sum_i \frac{[\chi_c^i(\theta,\phi) - \chi_e^i(\theta,\phi)]^2}{\chi_c^i(\theta,\phi)^2 + \chi_e^i(\theta,\phi)^2}$$

The quantities $\chi_c^i$ and $\chi_e^i$ are, respectively, the calculated and experimental photoelectron diffraction anisotropies. The smaller the $R_a$ factor, the better the agreement with experiment, with $0 \leq R_a \leq 1$. A perfect agreement corresponds to $R_a=0$, no agreement is expressed by $R_a=1$. The sum in the $R_a$ equation is over all angles in the database.

To find the best parameters in our relaxations in the simulations with MSCD code, we used a genetic algorithm.[Viana2007] The genetic algorithm was used to optimize the relaxation of the interlayer distances of the model clusters with five different variables $d_{12}$, $d_{23}$, $d_{34}$, $d_{45}$, and $d_{56}$, thus minimizing R-factor analysis.

The large number of elastic scattering events at low to moderate photoelectron kinetic energy make it is necessary to use multiple scattering calculations (MSCs). In order to reduce computing time for the cluster calculations we have followed a Rehrs-Albers (RA) approach in which the exact Green's function formalism is expressed in terms of scattering matrices expanded over all angular momentum quantum numbers m and l. The exact RA formalism is the curved wave analogy to the plane wave scattering. However, the scattering matrices can be truncated to 2nd, 3rd or 4th order depending on the intial state of the electron. Higher-order versions of RA are necessary for d and f initial states.[ChenY1998] Since our photoelectron diffraction data includes the Ba 4d emission we have used the 4th order RA approximation an allow up to eight scattering events within the cluster. The structure was optimized using rumpling (relative cation/anion displacement) and inter-planar relaxation parameters for the first atomic layers of both $TiO_2$-terminated and BaO-terminated BTO(001). The calculations were performed for a temperature of 300 K. The simulations are assessed with respect to the experimental data using a reliability factor, R.[ChenY1998] The smaller the R-factor, the better the agreement with experiment. A perfect agreement corresponds to R = 0, no agreement is expressed by R = 1. For oxide structures with many

parameters a good R factor is typically lower than 0.30-0.40.[Pancotti2009, Pancotti2013]

## 5.3 Results

### 5.3.1 XPS

Figure 5-4 shows an XPS survey spectrum for the clean BTO(001) surface. There is evidence for a small amount of surface C contamination, 10 times weaker than the O 1s intensity after taking into account the relative cross-sections. The C 1s line (BE = 284.6 eV) to check the binding energy calibration. As shown below in Figure 5-6(d), the C 1s XPD signal has weak anisotropy, suggesting that the C shows little local ordering. We assume that the residual C contamination does not alter systematically the surface order.

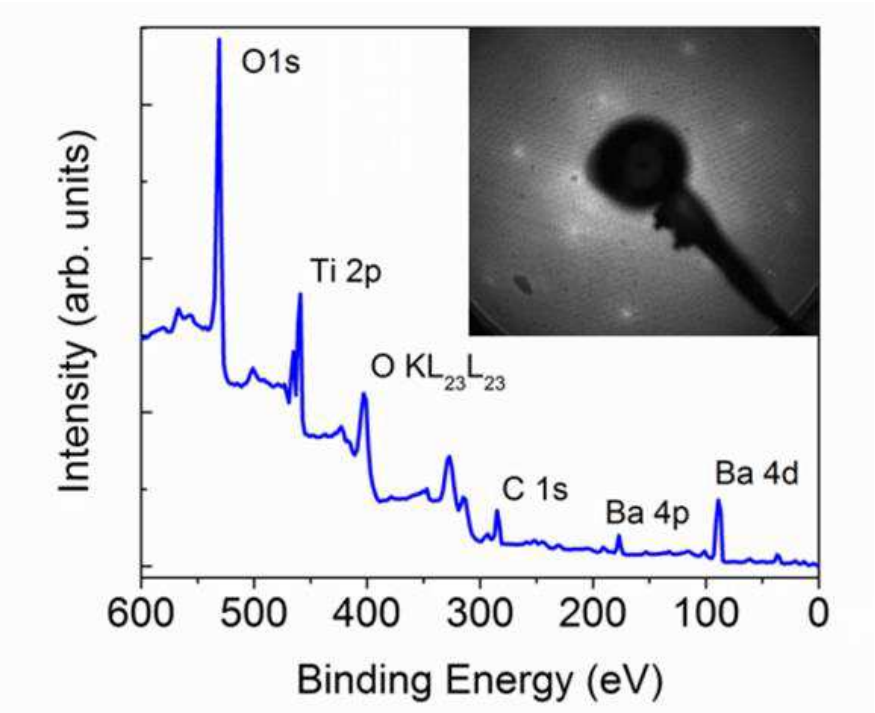


**Figure 5-4.** Survey XPS scan of clean BTO(001) single crystal. Inset typical (1 × 1) LEED image of the BTO(001) surface.

To characterize the surface chemistry, the core level spectra were taken with high counting statistics. The Ba $4d_{5/2}$, Ti $2p_{3/2}$ and O 1s core level spectra taken at normal (top) and 55° offnormal angle (bottom) emission, are shown in the Figure

5-5(a)-(c). A Shirley background was subtracted from all the core level spectra. The Ba $4d_{5/2}$ spectra have two components, see Figure 5-5(a). The spectra were fitted using a mixed Gaussian/Lorentzian lineshape (80/20 %) with a full width half maximum (FWHM) of 1.25 eV for both components and a spin orbit splitting of 2.55 eV. The binding energy (BE) of the main component at normal (55°) emission is 89.64 (89.67) eV and the high binding energy component (II) is at 90.76 (90.87) eV, thus the core level shift is 1.13 (1.20) eV. At 55° off normal detection, peak II increases in intensity, suggesting it is due to emission from surface or near-surface atoms. The shift is very similar to that observed on the clean surface of a thick $Ba_xSr_{1-x}TiO_3$ single crystal film.[Baniecki2006] However, a high binding energy component is also observed on a clean, $TiO_2$-terminated surface of BTO as in chapter 4. Therefore, it is not necessarily due to a reduced Ba-coordination, since in the latter case, there are no Ba surface atoms for such a surface. The atomic rearrangement to screen the surface charge can also modifies the electronic environment of the near-surface Ba atoms as described in chapter 4.

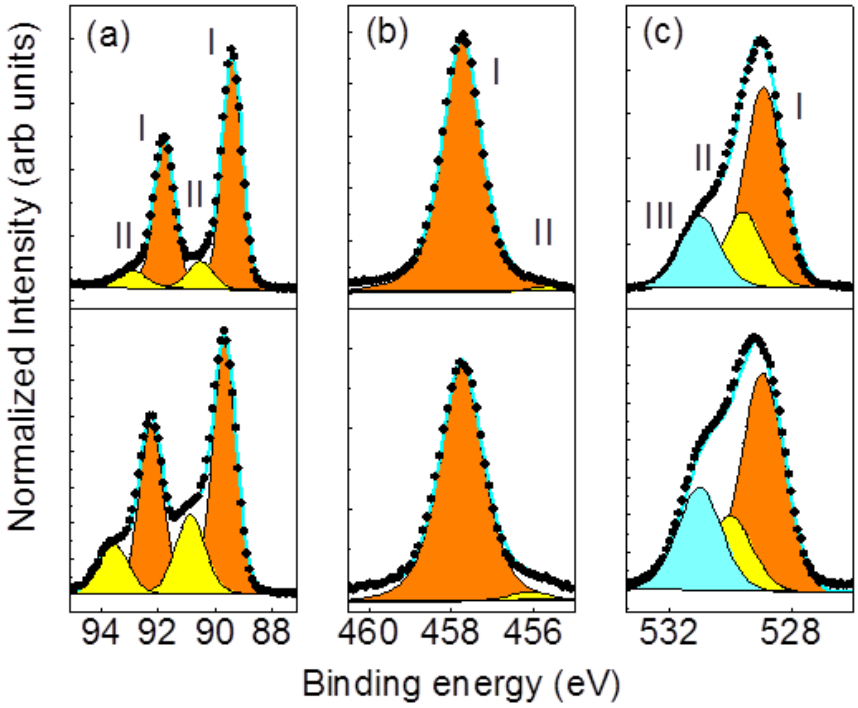


**Figure 5-5.** XPS core-level spectra: (a) Ba 4d; (b) Ti $2p_{3/2}$; (c) O1s core level spectra at normal (top) and 55° (bottom) surface sensitive emission angles. The bulk perovskite emission (I) is orange, the surface related components (II) in the Ba 4d and O 1s spectra and the $Ti^{3+}$ component (II) in the Ti $2p_{3/2}$ spectrum are in yellow and blue.

The Ti $2p_{3/2}$ spectra in Figure 5-5(b) are fitted with a FWHM of 1.3 eV and Gaussian/Lorentzian (80/20) line shapes. Both normal and grazing angle spectra have a main component (I) due to Ti bonding in the perovskite structure with valency of 4+. The component II, shifted by 1.8 eV to lower binding energy, is again associated with Ti in a reduced (3+) valence state due to the formation of oxygen vacancies after annealing.

In the O 1s spectrum (Figure 5-5(c), top) taken at the normal detection there are three components: peak I at 529.10eV (57.8 % intensity) and peaks II and III at 529.58 eV (21.7 %) and 530.94 (20.5 %), respectively. Peak I is due to oxygen in the bulk perovskite environment, peak II, shifted by 0.7 eV, is associated with proton adsorption on surface lattice oxygen and peak III to $OH^-$ adsorption at on-top cation sites as in chapter 4. The spectrum taken at 55° emission also has three peaks.

To quantify the surface nature of the Ba HBE peak we use the same layer by layer attenuation model as for BTO films in chapter 4. Assuming a BaO terminated surface, the fraction of the total Ba 4d intensity due to surface Ba atoms can be written as $(1 - k^2)$. Similarly, the fraction of the total O 1s intensity due to surface oxygen atoms is $(1 - k^2) / (2 + k)$. We assume that both BaO and $TiO_2$ have the same attenuation factor and use the inelastic mean free path values given above.

The model predicts that a 0.20 (0.32) fraction of the total Ba 4d intensity is due to surface atoms at normal (55° offnormal) emission angle. For the O 1s the predicted fraction is 0.18 (0.29). The respective experimental values for the Ba 4d are 0.14 (0.24) and for the O 1s 0.23 (0.36), close to the model predictions, suggesting that the surface is mainly BaO terminated. The difference between the measured and model values could be explained by an altered surface electronic environment extending over several atomic layers. The ionic displacements deduced from the XPD analysis discussed below provide further support for a changed near-surface electronic environment.

The fraction of $Ti^{3+}$ increases from 1.6 % to 3.5 % of the total intensity when going from normal to 55°. Each oxygen vacancy Vo reduces two $Ti^{4+}$ ions, and if we assume that Vo are created preferentially in the $TiO_2$ planes then this corresponds to a near-surface Vo concentration of 0.9 % (of the total number of

surface oxygen atoms) in the first $TiO_2$ layer. Using the XPS intensities, tabulated sensitivity factors[Wagner1979] and inelastic mean free paths[Tanuma1994] we can estimate the bulk (surface) stoichiometry of the sample to be $Ba_{0.214}Ti_{0.203}O_{0.583}$ ($Ba_{0.221}Ti_{0.197}O_{0.582}$) which is very close to the oxygen vacancy concentration as estimated from the $Ti^{3+}$ intensity. The O desorption energy at the surface is lower than in the bulk, thus the reduction in oxygen content with annealing is correlated with an increase in the proportion of Ba at the surface.

### 5.3.2 XPD results and simulations

In Figure 5-6(a)-(d) we present the experimental Ba 4d, Ti 2p, O 1s and C 1s XPD patterns acquired using 700 eV photon energy. The data are presented in the form of a stereographic projection or diffractogram. Normal emission intensity is at the center and grazing angle emission is at the edge of the diffractogram. The XPD anisotropy, as defined in chapter 4, is 33, 32, 23 and 8 % for the Ba 4d, Ti 2p, O 1s and C 1s, respectively. The anisotropy is sharpest for the Ba 4d emission. This is to be expected because the higher KE enhances forward focusing and thus the XPD signal reflects the bulk crystal structure, assumed to be constant, rather than that of the surface which may vary over the first atomic layers.

The angular anisotropy in the C 1s emission is low for most polar angles, only becoming significant at grazing emission, probably from residual gas in the chamber which was adsorbed onto the surface. The beam spot (~100μm) on the sample is much larger than the typical domain width (~1μm). The presence of domain ordering (visible to the eye) means that the XPD intensity anisotropies in the diffractograms correspond to a weighted sum of those due to the atomic structures of differently polarized domains. The aim of the simulations is to quantify both the surface structural changes in each domain and to estimate the proportion of each polarization present at the surface.

There are four possible in-plane polarizations which can be labelled $P_x$, $P_{-x}$, $P_y$ and $P_{-y}$. From symmetry each should have the same rumpling and relaxation in the z-direction, i.e. perpendicular to the surface plane. From consideration of the elastic energy there is no reason that there should be more of one particular in-plane polarization than anothers. We assume that all four in-plane polarizations are present in equal proportions. The in-plane polarization Pin can be written as $P^{in}$ =

($P_x + P_{-x} + P_y + P_{-y}$) /4. There are, therefore, three possible polarizations $P^+$, $P^-$ and $P^{in}$, satisfying the condition $N^+ + N^- + N^{in} = 1$, where $N^+$, $N^-$, $N^{in}$ are the fractions of each domain type contributing to the XPD signal.

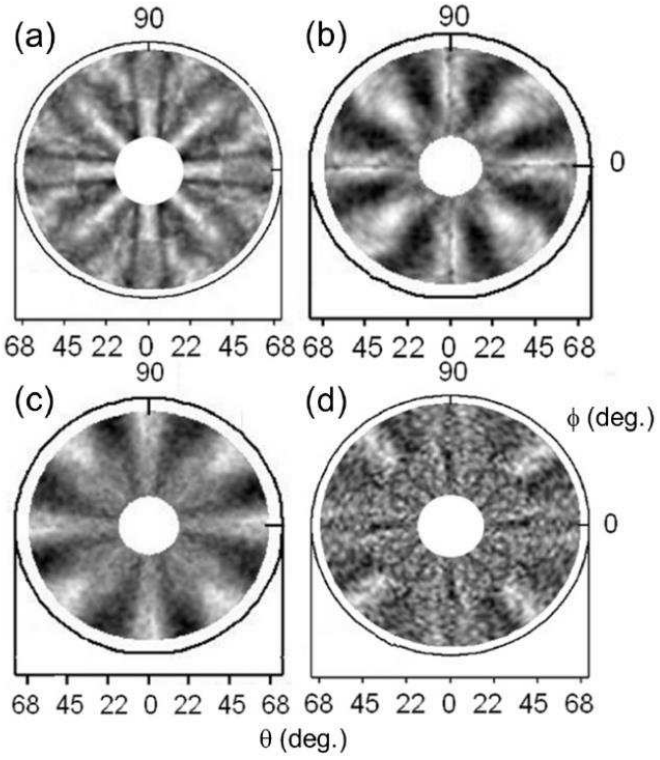


**Figure 5-6.** Experimental XPD for BTO(001) obtained with 700 eV photon energy for (a) Ba 4d, (b) Ti 2p, (c) O 1s and (d) C 1s emission.

The surface atomic structure of each polarization is described in terms of 7 parameters: 4 layer rumpling values $\eta_i$ and 3 inter-layer relaxation parameters $\Delta d_{ij}$, giving in total 23 adjustable parameters. The R-factor optimization of the Ba 4d, Ti 2p and O 1s simulations must converge to the same result to give a reasonable solution. This is an extremely large parameter space and it is unrealistic to adjust all 23 parameters simultaneously and expect convergence to a global minimum. We have adopted the following three step method, which we refer to as method (1).

In the first step the R-factor for each of the Ba 4d, Ti 2p and O 1s XPD patterns is minimized with respect to the experimental diffraction pattern assuming a single polarization value. This is repeated for each of the three possible polarizations, $P^+$, $P^-$ and $P^{in}$.

The atomic positions are then fixed to these values and the R-factors are optimized by linear combination of $P^+$, $P^-$ and $P^{in}$ for each XPD pattern. Since $N^+ + N^- + N^{in} = 1$, the results can be presented in the form of a contour plots with $N^+$ and $N^-$ axes.

In the third step, $N^+$, $N^-$ and $N^{in}$ are fixed at the average $N^+$, $N^-$ and $N^{in}$ values for the three XPD patterns and all twenty one structural parameters $\eta_i$ and $\Delta d_{ij}$ values are simultaneously relaxed.

Prior to the first step the non-structural parameters were determined giving a 400 K Debye temperature and ~6 eV[Nascimento2007] for the inner potential; this calculation was performed for two possible terminations, BaO or $TiO_2$ surface. The Debye temperature represents an average value for the Ba, O and Ti emitters. The experimental lattice positions of bulk tetragonal BTO were used as initial values. [Mitsui1981] For the in-plane polarization the lateral positions were fixed at those given by Padilla and Vanderbilt.[Padilla1997] The values of the non-structural parameters are assumed not to vary in the final optimized structure.

Step 1

The R-factor minimization as a function of rumpling and relaxation was done using the genetic algorithm method described in chapter 3.2 for each (Ba 4d, Ti 2p and O 1s) XPD simulation.[Viana2007] The O 1s XPD pattern is used to ascertain the surface termination layer since the corresponding XPD data is the most surface sensitive. The experimental and simulated XPD azimuthal curves for BaO or $TiO_2$ terminated surfaces at different, fixed polar angles (14.6°, 30.6°, 45.6° and 68.6°), with a $P^+$ polarization are presented in Figure 5-7. As in the experimental XPD, the best fit is systematically obtained for the BaO terminated layer. All simulations were therefore done assuming that the surface is mainly BaO terminated.

The results for $P^+$, $P^-$ and $P^{in}$ polarization states for the Ba 4d, Ti 2p and O 1s after the 1st step of the R-factor optimization are shown in Figure 5-8. The simulated Ba 4d patterns have the sharpest structure, demonstrating the higher kinetic energy will favour the forward scattering regime and is less sensitive to surface relaxations.

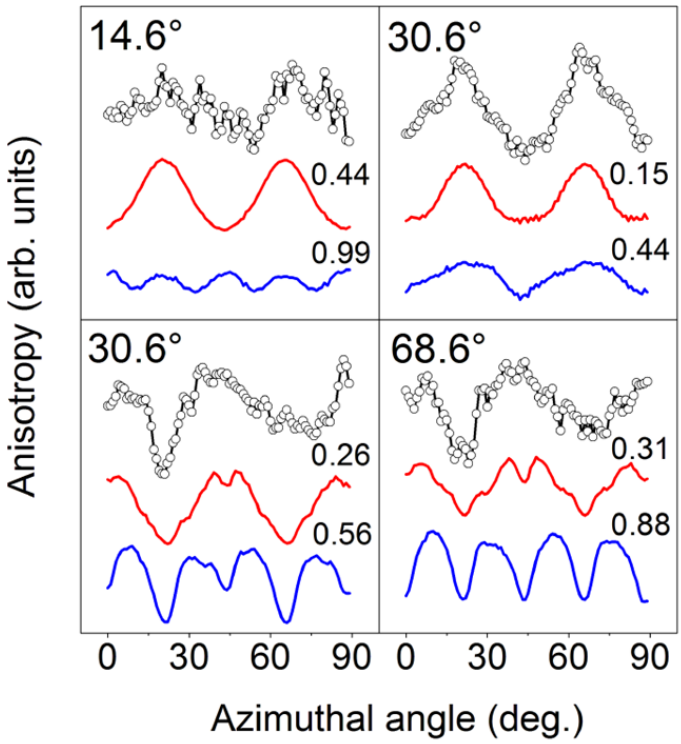


**Figure 5-7.** Experimental and simulated O 1s XPD azimuthal curves taken at polar angles of 14.6°, 30.6°, 45.6° and 68.6°.The experimental anisotropy (circles) is compared with the simulations for $TiO_2$ (blue) and BaO (red) terminations in $P^+$ polarization. The numbers represent the R-factors obtained with $TiO_2$ and BaO terminations in $P^+$ polarization.

Step2

The results of the 2nd step minimization of the R-factor as a function of a linear combination of $P^+$, $P^-$ and $P^{in}$ are reported in Figure 5-9 in the form of R-factor contour plots for Ba 4d (Figure 5-9(a)), Ti 2p (Figure 5-9(b)) and O 1s (Figure 5-9(c)). The $N^+$ and $N^-$ values are read from the center of the minimum contour of the R-factor. The linear combination minimizing the R-factor are close but not the same for all three XPD patterns. For the Ba 4d and O 1s XPD, the R-factor of a linear combination is minimized for a surface with approximately 56 % $P^+$ and 44 % $P^-$ domains, whereas for the Ti 2p XPD, the R-factor of a linear combination reaches minimum with 58 % $P^+$, 8 % $P^-$ domains and 34 % $P^{in}$ and for the O 1s the minimum is found for 54% $P^+$ and 46% $P^-$. Figure 5-10 shows the average contour plot of the R-factor as a function of polarization for the three XPD patterns. The minimum is found for 55 % $P^+$, 38 % $P^-$ and 7 % $P^{in}$.

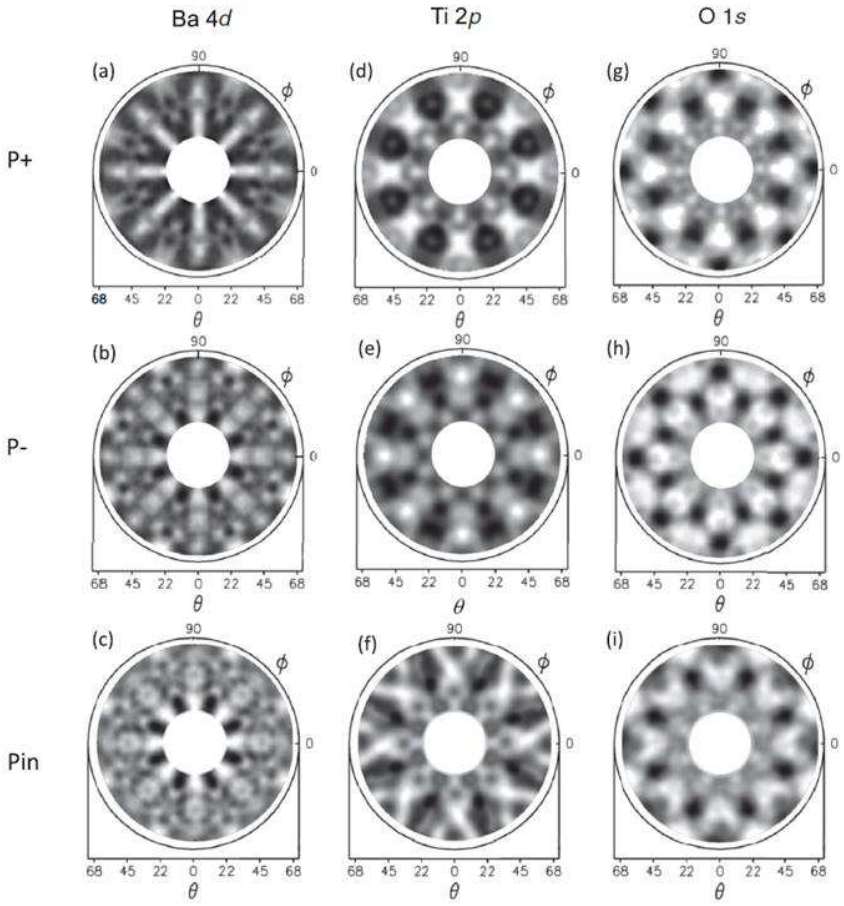


**Figure 5-8.** Multiple scattering simulations of (a)-(c) Ba 4d (d)-(f) Ti 2p and (g)-(i) O 1s XPD for (a), (d), (g) $P^{+}$, (b), (e), (h) $P^{-}$ and (c), (f), (i) $P^{in}$ polarization.

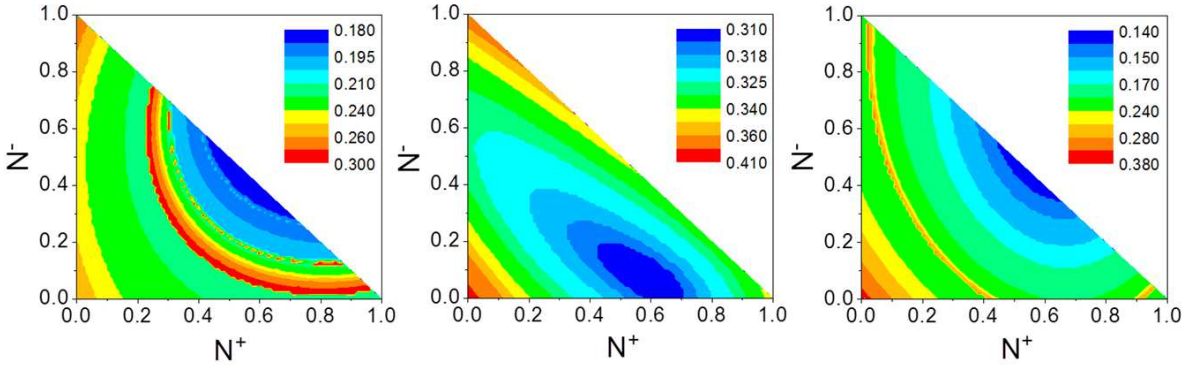


**Figure 5-9.** R-factor $N^{+}/N^{-}$ contour plots for (a) Ba 4d (b) Ti 2p and (c) O 1s XPD simulation. $N^{+}$, $N^{-}$ and $N^{in}$ are the proportions of $P^{+}$, $P^{-}$ and $P^{in}$ domains contributing to the XPD signal satisfying the condition $N^{+}+ N^{-} + N^{in}= 1$, and $P^{in}= (P_x +P_{-x} +P_y +P_{-y})/4$.

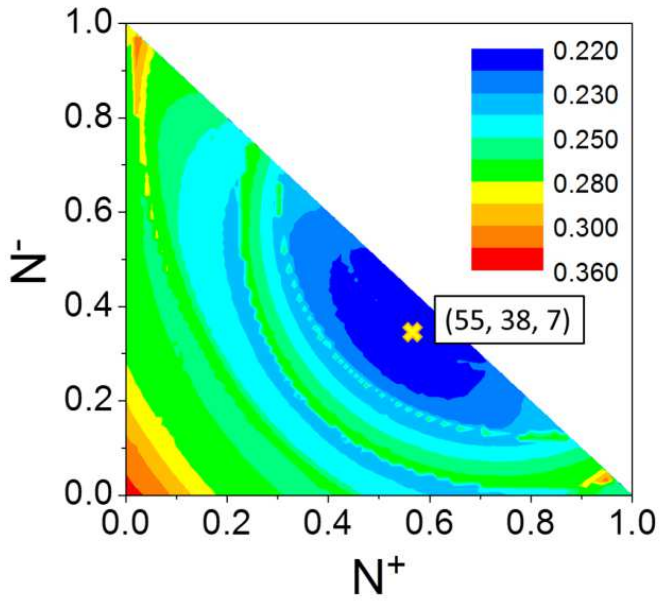


**Figure 5-10.** Average R-factor $N^+/N^-$ contour plot of Figure 5-10. The R-factor minimum is at 55 % $P^+$, 38 % $P^-$ and 7 % $P^{in}$.

Step 3

Finally, for each XPD pattern, Ba 4d, Ti 2p and O 1s, we have held the linear combination constant at 55 % $P^+$, 38 % $P^-$ and 7 % $P^{in}$ and iterated simultaneously the 21 rumpling and relaxation parameters. The atomic rumpling $\eta = [\delta_z(M) - \delta_z(O)]/2$ and the changes in the inter-planar spacing $\Delta d_{ij}$ are given in Tables 5-I, 5-II, 5-III for the Ba 4d, Ti 2p and O 1s XPD simulations.

Figure 5-12 compares the final simulated diffractogram obtained with the relaxed atomic distortions and the linear combination of 55 % $P^+$, 38 % $P^-$ and 7 % $P^{in}$ domains with experiment. All of the experimental structure is reproduced. The structure appears blurred in comparison with the simulations of singly polarize domains in Figure 5-9, however, the much better R-factor demonstrates that this blurring is in fact due to the simultaneous presence of different surface polarizations. The Ti 2p simulation shows similar agreement with experiment. The agreement is less good for the O 1s, again we think that this is due to the residual surface contamination since the O 1s XPD is the most surface sensitive and also should show the strongest multiple scattering effects. Figure 5-13(a) and (b) are sectional schematics of the inter-planar relaxation and intra-planar rumpling for the first four atomic layers in $P^+$ and $P^-$ domains, respectively. The original and relaxed

atomic layer positions are indicated by dotted and solid lines respectively. The vertical atomic displacements are multiplied by 10 for clarity.

We also tried a second method to optimize the strctures, method (2), which should, in principle, converge to the same solution.

First, the linear combination of $N^+$, $N^-$ and $N^{in}$ is found using the bulk atomic structure in the ferroelectric phase. Then, with $N^+$, $N^-$ and $N^{in}$ fixed, the rumpling and relaxation for each polarization has been optimized. The results are shown in Figure 5-11(a)-(c). Three distinct minima are found for the Ba 4d, Ti 2p and O 1s XPD simulations. The minima are also much shallower than those obtained using method (1), illustrated in Figure 5-9. It was not possible to find a global minimum using method (2). Furthermore, the R-factors obtained are much larger than those of method (1). We interpret this as being due to the use of the bulk ferroelectric distortion without relaxation and rumpling as starting values for the simulations to search for the best linear combination of $N^+$, $N^-$ and $N^{in}$. Such values are too far from those giving a consistent solution with method (1), even for the genetic algorithm. In other words, there are indeed significant structural changes in the first few atomic layers of BTO(001) with respect to the bulk FE structure.

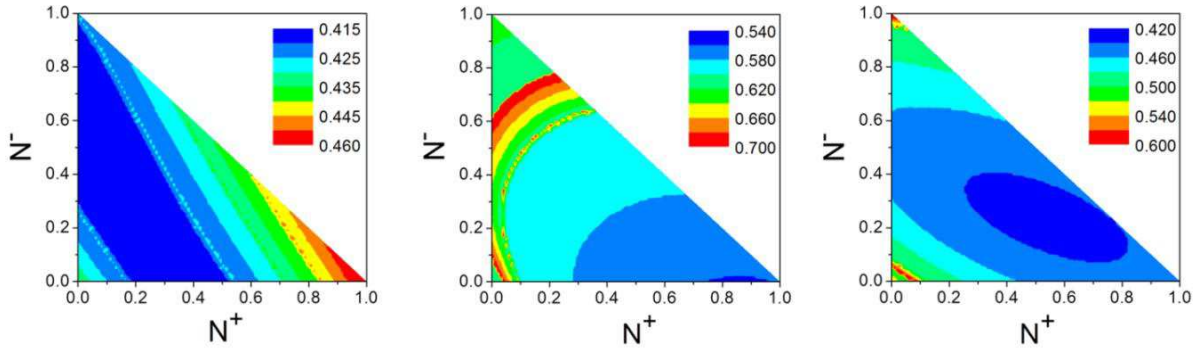


**Figure 5-11.** R-factor $N^+/N^-$ contour plots for (a) Ba 4d, (b) Ti 2p and (c) O 1s XPD simulations.

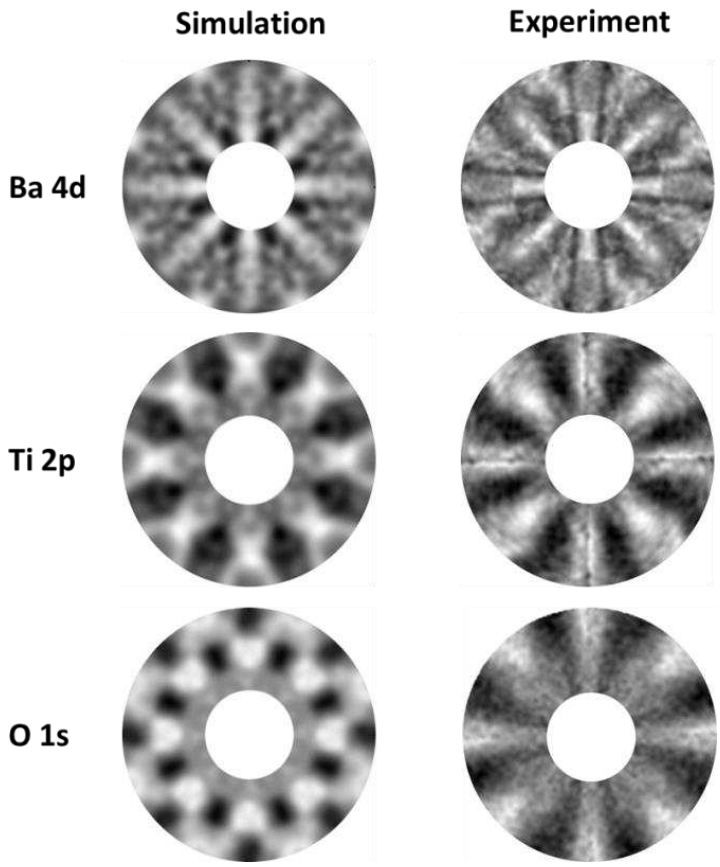


**Figure 5-12.** Comparison between the final simulated diffractogram obtained with the relaxed atomic distortions and the linear combination of 55 % $P^{+}$, 38 % $P^{-}$ and 7 % $P^{in}$ domains with experiment.

## 5.4 Discussion

The rumpling and relaxation amplitudes in Figure 5-13 vary when going from the surface layer into the bulk. The main atomic distortion in BTO is expected around the Ti ion, however, because of the longer inelastic mean free path, the Ti 2p photoelectrons are more sensitive to the subsurface atomic layers than the O 1s and probably give slightly less accurate values for surface related atomic distortions. The O 1s XPD is extremely surface sensitive with an inelastic mean free path of 6.9 Å. The Ba 4d XPD is the most sensitive to distortion in the sub-surface atomic layers, closer to that in the bulk. This spread in depth sensitivities is actually an advantage because the three XPD simulations are required to converge to a structure which describes changes in relaxation and rumpling going from the surface into the bulk.

The rumpling and interlayer relaxation in Tables 5-I, 5-II and 5-III can be compared with first principles theory and experiment in the literature reproduced in Table 5-IV, using c/2 = 2.018 Å to obtain η and $\Delta d_{ij}$.[Padilla1997, Meyer2001, Shin2008]

The rumpling for $P^{\pm}$ states have the same sign as the polarization and are quantitatively similar. The rumpling magnitude varies between 0.01 Å and 0.06 Å with a mean value of 0.03 Å (0.7% of the lattice parameter) whereas the magnitude of the interlayer relaxation varies between 0.01 Å and 0.13 Å with a mean value of 0.038 Å (0.95 % of the lattice parameter) over the first four layers. In general, the rumpling increases deeper into the BTO whereas the $\Delta d_{ij}$ values decrease towards the bulk. The Δd values obtained from the Ti 2p and O 1s simulations show a larger spread in values for the sub-surface layers, possibly reflecting the higher surface sensitivity.

Large rumpling and small interplanar relaxation are consistent with bulk ferroelectric distortion, unaffected by surface boundary conditions. The lower rumpling at the surface is consistent with partial screening of surface polarization charge by atomic rearrangement, giving rise to a surface polarization lower than in the bulk. No significant change in rumpling or relaxation is observed beyond the 4th atomic layer, i.e. the FE distortion is no longer influenced by the surface and has adopted the bulk value. These results shed some new light on the nature of the surface "dead" layer.[Zhou1997, Li2005] Atomic displacements can reduce the surface polarization but given the non-zero rumpling observed by XPD, the surface may not be completely "dead" in terms of ferroelectric polarization. This agrees with predictions made on the basis of first principles calculations of a BaO terminated in-plane polarized surface[Geneste2009] and with the LEED I-V described in chapter 4 on an epitaxially strained BTO(001) thin film which showed that reconstruction can even give rise to a dipole inversion in the clean surface layer. The interlayer relaxation tends to zero going into the bulk corresponding to a constant ferroelectric distortion, as expected far from the polarization discontinuity of the surface. The structural changes over the first two unit cells will modify the near-surface electronic environment, providing a more satisfactory qualitative explanation of the high binding energy component in the Ba 4d core level spectrum. However, this must be confirmed by more systematic experiments and calculations.

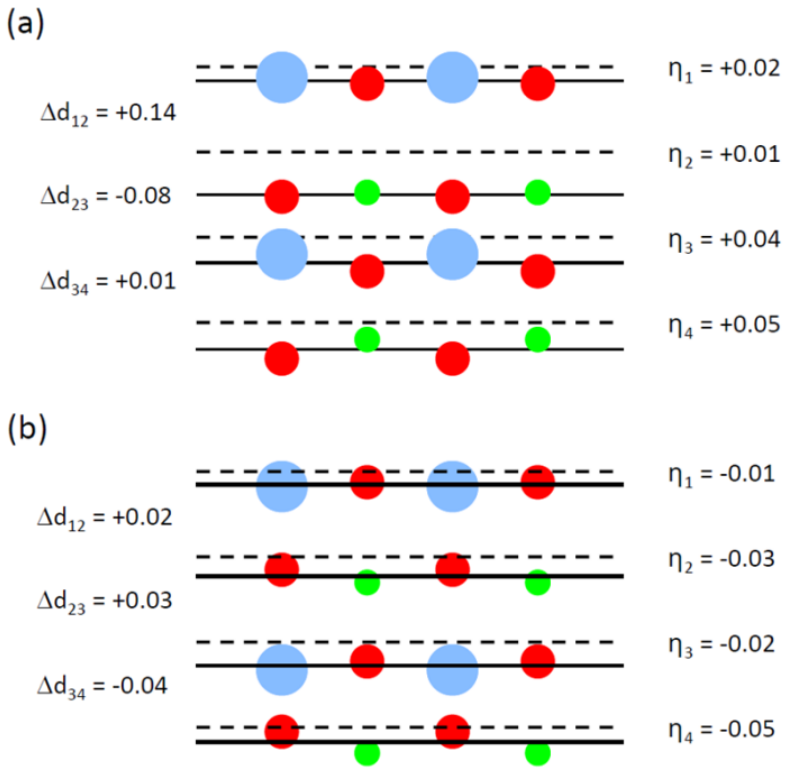


**Figure 5-13.** Relaxation and rumpling for the first four atomic layers in (a) $P^+$ and (b) $P^-$ domains obtained from O 1s XPD. The original and relaxed atomic layer positions are indicated by dotted and solid lines respectively. The atomic displacements are multiplied by 10 for clarity. Color coding as in Figure 2-6.

Figure 5-14 shows a qualitative schematic of how the differently polarized domains deduced from the best linear combination of the multiple scattering results might combine at the surface. The antiparallel, out of plane polarizations give rise to 180° domain walls, perpendicular to the surface. However, the presence of 7 % in-plane polarization at the surface implies that there are also some 90° domain walls which intersect the surface at 45° as shown on the right hand side of Figure 5-14. Other forms of screening by adsorbates, defects or free charge carriers have not been taken into account. Although the parameter space is large, the full Ba 4d, Ti 2p and O 1s XPD patterns constitute three independent measurements of the same atomic distortions, each of which is used to optimize a consistent multiple scattering simulation.

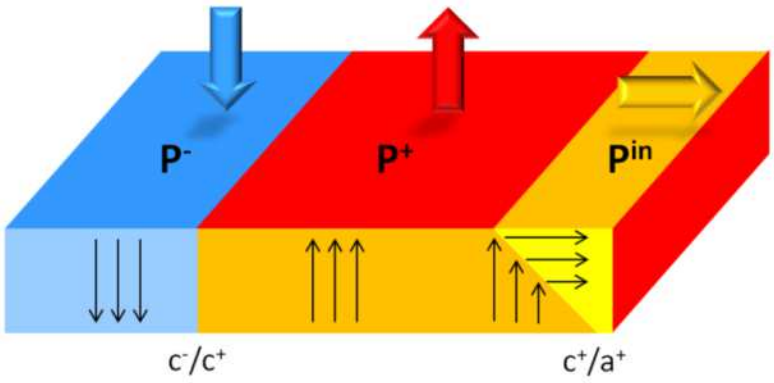


**Figure 5-14.** qualitative schematic of surface domain ordering and domain walls resulting from the best fit of a linear combination of the multiple scattering simulations to the experimental data.

| | Ba 4d | | |
|---|---|---|---|
| | $P^+$ | $P^-$ | $P^{in}$ |
| $\eta_1$ | +0.02 | -0.01 | +0.02 |
| $\eta_2$ | +0.01 | -0.03 | +0.03 |
| $\eta_3$ | +0.04 | -0.02 | +0.01 |
| $\eta_4$ | +0.05 | -0.05 | +0.02 |
| $\Delta d_{12}$ | +0.14 | +0.02 | -0.02 |
| $\Delta d_{23}$ | -0.08 | +0.03 | +0.09 |
| $\Delta d_{34}$ | +0.01 | -0.04 | -0.06 |

**Table 5-I.** Atomic rumpling (η) and changes in inter-planar spacing ($\Delta d_{ij}$) obtained from the final Ba 4d XPD simulation for in- and out-of-plane polarizations. All values are in Å.

| | Ti 2p | | |
|---|---|---|---|
| | $P^+$ | $P^-$ | $P^{in}$ |
| $\eta_1$ | +0.01 | -0.01 | +0.03 |
| $\eta_2$ | +0.02 | -0.04 | +0.03 |
| $\eta_3$ | +0.02 | -0.02 | +0.01 |
| $\eta_4$ | +0.05 | -0.04 | +0.02 |
| $\Delta d_{12}$ | -0.02 | -0.02 | -0.02 |
| $\Delta d_{23}$ | -0.04 | +0.04 | +0.05 |
| $\Delta d_{34}$ | +0.08 | -0.03 | -0.06 |

**Table 5-II.** Atomic rumpling (η) and changes in inter-planar spacing ($\Delta d_{ij}$) obtained from the final Ti 2p XPD simulation for in- and out-of-plane polarizations. All values are in Å.

| | O 1s | | |
|---|---|---|---|
| | $P^+$ | $P^-$ | $P^{in}$ |
| $\eta_1$ | +0.01 | -0.01 | +0.03 |
| $\eta_2$ | +0.02 | -0.04 | +0.04 |
| $\eta_3$ | +0.03 | -0.04 | +0.01 |
| $\eta_4$ | +0.02 | -0.06 | +0.05 |
| $\Delta d_{12}$ | -0.02 | -0.02 | -0.04 |
| $\Delta d_{23}$ | -0.04 | +0.04 | +0.01 |
| $\Delta d_{34}$ | +0.05 | 0.00 | -0.01 |

**Table 5-III.** Atomic rumpling ($\eta$) and changes in inter-planar spacing ($\Delta d_{ij}$) obtained from the final O 1s XPD simulation for in- and out-of-plane polarizations. All values are in Å.

| | literature | | |
|---|---|---|---|
| | $P^+$ | $P^-$ | $P^{in}$ |
| | [Fechner2008] | [Schneider1998] | [Berlich2011] |
| $\eta_1$ | +0.01 | +0.03 | -0.03 |
| $\eta_2$ | +0.03 | +0.04 | +0.04 |
| $\eta_3$ | +0.01 | +0.03 | +0.01 |
| $\eta_4$ | +0.03 | +0.05 | -- |
| $\Delta d_{12}$ | -0.09 | +0.02 | -0.12 |
| $\Delta d_{23}$ | +0.16 | -0.02 | +0.04 |
| $\Delta d_{34}$ | -0.03 | +0.02 | -- |

**Table 5-IV.** Vertical atomic rumpling ($\eta$) and changes in inter-planar spacing ($\Delta d_{ij}$) from first principles calculations and experimental LEED data. The displacements of Ref. [Despont2006] were converted back to the absolute displacements using the calculated lattice parameter. The $\delta$(O) value used in the $TiO_2$ plane is the average of the two oxygen displacements. All values are in Å.

The R-factor minimization strategy has made use of a genetic algorithm and a step by step approach to a global minimum. The best solution is found for a linear combination of in and out of plane surface domain polarizations. The good agreement with available literature values for the atomic rumpling and inter-planar spacings and the consistency of three independent measurements of the ferroelectric distortions by the Ba 4d, Ti 2p and O 1s XPD suggest that the method presented is fairly reliable. We therefore have a method which relates both to macroscopic FE domain ordering and microscopic surface reconstruction within each domain.

This interpretation does not attempt to quantify other forms of screening by adsorbates, defects or free charge carriers. Oxygen vacancies were necessary to avoid charging under photoemission. The Ti 2p XPS shows that there are Vo near the surface. We assume that the intrinsic contribution of Vo to polarization stability is the same for $P^+$ and $P^-$, however, there is evidence that this may not always be the case.[Mi2012] Further work is needed in this direction to study correlation between Vo and surface structural charges.

An obvious next step would be the use of spatially resolved XPD to distinguish a single FE domain. This could be done using a zone plate to obtain a micro-focused beam smaller than the domain width. The Vo concentration is also an important question since it increases the sample conductivity. The formation of Vo by annealing in UHV was necessary in order to avoid charging under the synchrotron beam, too much conductivity would destroy the ferroelectric state. One recent study of BTO suggests that above a critical doping level of $1.36\times10^{21}/cm^3$ a tetragonal to cubic insulator-metal transition occurs.[Iwazaki2012] This corresponds to an Vo concentration of 2-3 %, higher than the values discussed here as estimated from the $Ti^{3+}$ component of the Ti 2p spectra. The BTO surface studied here is therefore still ferroelectric despite the annealing treatment. This is supported by the observation of variations in the surface layer rumpling on a similar sample, which was inverted by dissociative adsorption of water as described in chapter 4. This would not be expected if, for example, the system had already undergone a transition to a metallic, paraelectric state due to the Vo concentration.

## 5.5 Conclusion

XPD using synchrotron radiation was used to determine the domain structure, atomic rumpling and inter-planar relaxation at the surface of BTO(001). After ex-situ cleaning and in-situ annealing in oxygen the surface is atomically flat with a preferential BaO termination plane and a (1 × 1) surface structure. Multiple scattering simulations of Ba 4d, Ti 2p and O 1s XPD are performed using a genetic algorithm. Given the large parameter space a three step method is used to converge to a global R-factor minimum. Polarization dependent rumpling and interplanar relaxation is determined and the proportion of in and out-of plane polarized domains obtained. At the surface of clean BTO(001) single crystal the polarization

charge is screened by a combination of domain ordering and surface structural changes. These results provide a complete experimental description of surface rumpling and relaxation as a function of polarization and a quantitative estimate of the proportion of differently polarized surface domains.

# Chapter 6

# Screening of ferroelectric domains on $BaTiO_3$ (001) surface by ultraviolet photo-induced charge and dissociative water adsorption

## 6.1 Introduction

Photo-generated charge carriers can also efficiently screen the surface and interface polarization charge and hence the depolarizing field.[Kalinin2002, Shao2006, Wu2011] The photo-generated pair lifetimes can be strongly dependent on the ferroelectric surface topology and the polarization state can influence redox reactions.[Wang2012, Alexe2012, Giocondi2001] In this chapter, we present results on the comparing role of photo-generated free charge and dissociative water adsorption in screening polarization of micro-sized domains of $BaTiO_3$.

To detect changes in the surface potential, near-field techniques such as piezo-response force microscopy (PFM) or scanning surface potential microscopy (SSPM) have been successfully used (Figure 6-1).[Gruverman2002, Kalinin2001] Another approach, avoiding tip-surface interactions which may influence the domain polarization[Shao2006], is mirror electron microscopy (MEM) using a low energy electron microscope (LEEM), as described in chapter 3. Variations in the MEM-LEEM energy can then be related to changes in the screening of the surface polarization charge.

We have used MEM-LEEM to perform an experimental study of the surface potential of a $BaTiO_3$ (001) single crystal under UV illumination. We compare the relative efficiencies of chemisorption and free charge carriers in screening the surface charge. X-ray photoelectron spectroscopy (XPS) provides information on the surface chemistry. The MEM-LEEM transition is measured as a function of the FE polarization under UV illumination before and after the dissociative adsorption of water. The potential contrast in the MEM-LEEM transition reflects the screening

of the polarization charge of the $P^+$ and $P^-$ domain surfaces. In a second experiment, the dynamics of screening by photo-generated carriers on dry and wet surfaces are also studied.

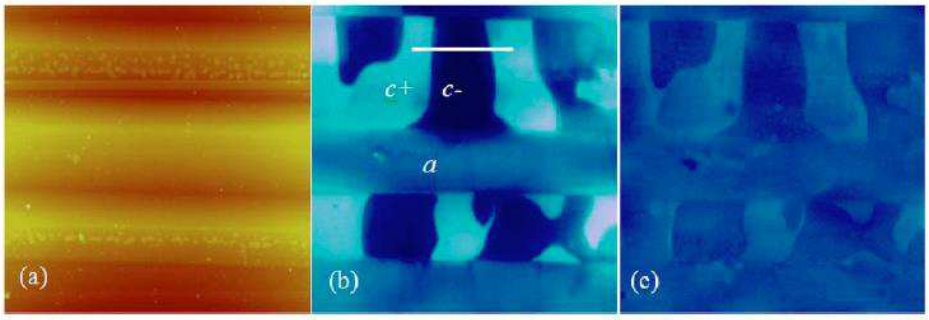


**Figure 6-1.** (a) AFM topography of a $BaTiO_3$ (001) surface that shows three corrugations due to a-c domain walls. z scale is 200 nm.(b) The surface potential image of the same area as shown in (a) shows c domains with curved domain walls. (c) The surface potential image when the UV light is on. z scale is 0.25 V. (This figure is reproduced from [Shao2006])

## 6.2 Experimental section

The 10×10×0.5 mm BTO(001) single crystal was furnished by SurfaceNet GmbH. To eliminate surface carbon contamination, the sample was cleaned by UV-ozone before being introduced into the UHV chamber. Then it was annealed in situ at 700 °C for 3 hours with a base pressure of $1x10^{-9}$ mbar to remove residual contamination on the surface such as $H_2O$ or $CO_2$ ensuring an adsorbate free surface and to create sufficient oxygen vacancies to avoid charging during XPS and LEEM measurements. Water exposure was performed the same dedicated third chamber as described in chapter 4. Pure $H_2O$ was obtained by freeze-pump-thaw cycles and then introduced into the chamber at $1 \times 10^{-4}$ Torr for 1 h, equal to $3.6 \times 10^5$ L. After exposure, sample was transferred back to the main chamber for the MEM-LEEM analysis using an Elmitec III LEEM. UV illumination was carried out by a Driel UV lamp with primary line of 254 nm. The exposure power of 20 $mW/cm^2$ on the sample surface was measured by a power meter. All MEM-LEEM images have been normalized with respect to the flat field to minimize contributions due to inhomogeneities in the double multi-channel plate detection system.

XPS was carried out using a monochromatic Al Kα (1486.7 eV) X-ray source (Omicron Nanotechnology GmbH). The overall energy resolution (photons and spectrometer) was 0.35 eV. The data were analyzed using the CasaXPS software[CasaXPS] which employs a linear least squares optimization with a peak fitting algorithm. Shirley backgrounds were subtracted from the data as part of the curve fitting process.

## 6.3 Results and discussion

### 6.3.1 $BaTiO_3$ single crystal under UV exposure

The C 1s peak is below the detection limit in XPS showing that the surface is clean with very low carbon contamination (Figure 6-2(a)). The Ba 3d, Ti 2p and O 1s core level XPS spectra are shown in Figure 6-2(b)-(d) at normal and grazing (60°) emission. The high resolution XPS spectra of Ba $3d_{5/2}$ are shown in Figure 6-2(b). The main peak, labeled I, has a binding energy (BE) of 778.8 eV and is due to bulk-coordinated Ba. Each spectrum also has a component labeled II, shifted by 1.7 eV to high binding energy (HBE). The grazing emission angle spectrum confirmed that this HBE component is of surface origin as in chapter 4. The Ti $2p_{3/2}$ spectra are presented in Figure 6-2(c). The spectra have a main component (BE 458.5 eV) due to Ti with a formal valency of 4+ as in the perovskite structure, and a weak, component, shifted by 1.7 eV to low binding energy (LBE), corresponding to $Ti^{3+}$ resulting from the formation of oxygen vacancies, Vo. We consider each layer as a homogeneous medium and take into account the layer attenuation factor given by k as presented in chapter 4. The surface Vo concentration can be estimated to be 3.0 %. The XPS is sensitive only to the first few nanometers of the surface where the annealing induced Vo concentration is expected to be highest. Deeper in the crystal the Vo concentration may be much lower. Indeed, the slight charging under UV illumination (see below) shows that the bulk crystal still has a high insulating characteristic.

Figure 6-2(d) shows the O 1s spectra. The spectrum has three components, peak I is due to oxygen in the perovskite environment,[Baniecki2006] and peaks II and III, both of which are of surface origin. $O_{II}$ may be attributed to oxygen in lattice positions coordinated with a proton, as described in chapter 4, whereas $O_{III}$ is

ascribed to hydroxyl groups chemically bound to surface cations,[Baniecki2006] present even in "dry" samples. [Wendt2006]

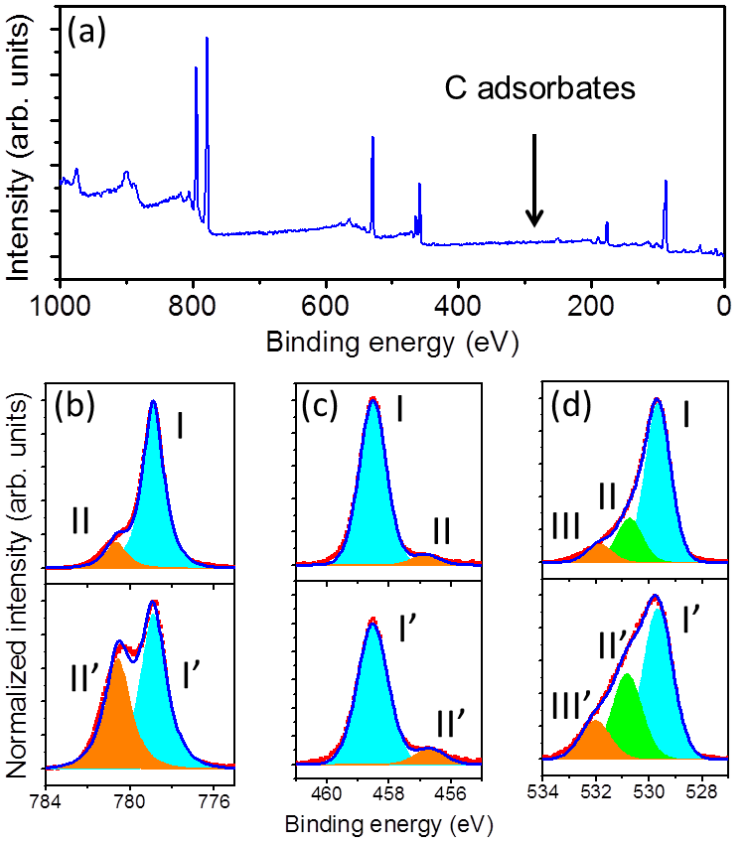


**Figure 6-2.** XPS core level spectra: (a) Survey; (b) Ba $3d_{5/2}$; (c) Ti $2p_{3/2}$; (d) O 1s core level spectra at normal (top) and 60° offnormal (bottom) detection angles.

The right hand inset of Figure 6-3 is a typical MEM image from the clean sample taken at a start voltage of -1.8 V with a field of view (FoV) of 40 µm. Some other MEM-LEEM images with different start voltage are shown in Figure 6-4. Two distinct levels of intensity are observed corresponding to different electrostatic potentials above the surface. This is supported by the inversion in the intensity contrast as start voltage is increased. We identify the two regions as the surfaces of differently polarized domains ($P^+$ and $P^-$, see below). The reflectivity curves extracted from the two domains are plotted in Figure 6-3 (full symbols) as a function of start voltage. The position of the MEM-LEEM transition is obtained from the midpoint of the decrease in the reflectivity curve. The difference in the

MEM-LEEM transition measures directly the difference in the electrostatic potential above the surface and hence in the effective surface charge.

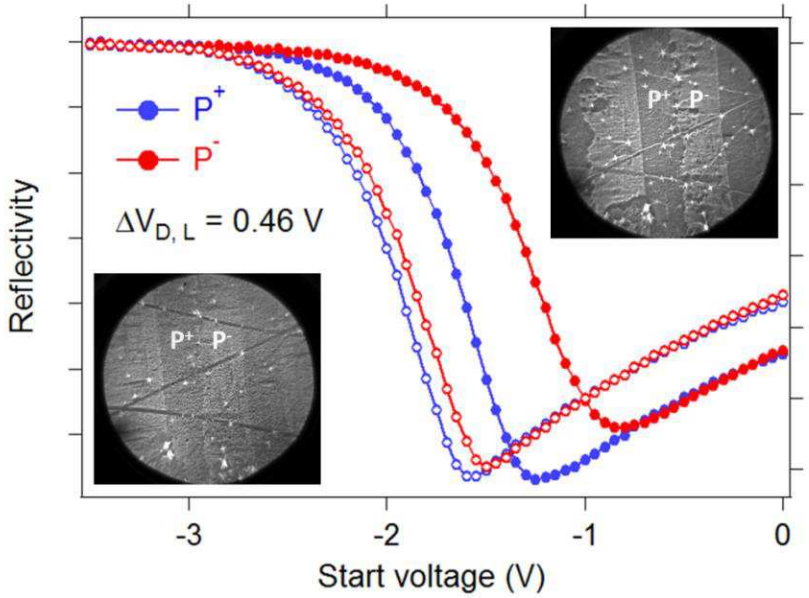


**Figure 6-3.** Right-hand inset: MEM image at a start voltage of -1.8V showing the contrast in electrostatic potential above the clean surface of differently polarized domains. Left-hand inset: same in steady state conditions with UV illumination. Main figure: reflectivity curves extracted from $P^+$ and $P^-$ domains as a function of start voltage without (full symbols) and with (open symbols) UV illumination.

At the clean surface, the shift in the MEM-LEEM transition between the two domains is 400 mV. Such a large shift in electrostatic potential is attributed to opposite polarizations perpendicular to the surface, pointing either outwards ($P^+$) or inwards ($P^-$). Using PFM, Shao et al. reported a 150-200 mV shift between $c^+$ and $c^-$ domains as presented in Figure 6-1, however, their data were acquired in air and the potential contrast was probably attenuated by adsorbates.[Shao2006] Our UHV prepared surface is adsorbate free as shown by the XPS and AES.

When the sample was illuminated with UV light, the shift in the MEM-LEEM transition between the two domains is significantly reduced within a few tens of seconds, reaching a steady state value of 90 mV after 200 seconds. The reflectivity curves extracted from the two domains are plotted in Figure 6-3 (open symbols) as a function of start voltage. A PEEM intensity due to the UV illumination is also detected, however, the intensity was more than three orders of magnitude lower

than that of the MEM-LEEM signal, it therefore makes a negligible contribution to the acquired images. As can be seen in the left hand inset of Figure 6-3, the domain structure is unchanged by the UV illumination, but the contrast is reduced. When the UV light is switched off, the contrast gradually increases back to the original value, although at a slower rate. The experiment is repeatable without altering the domain structure.

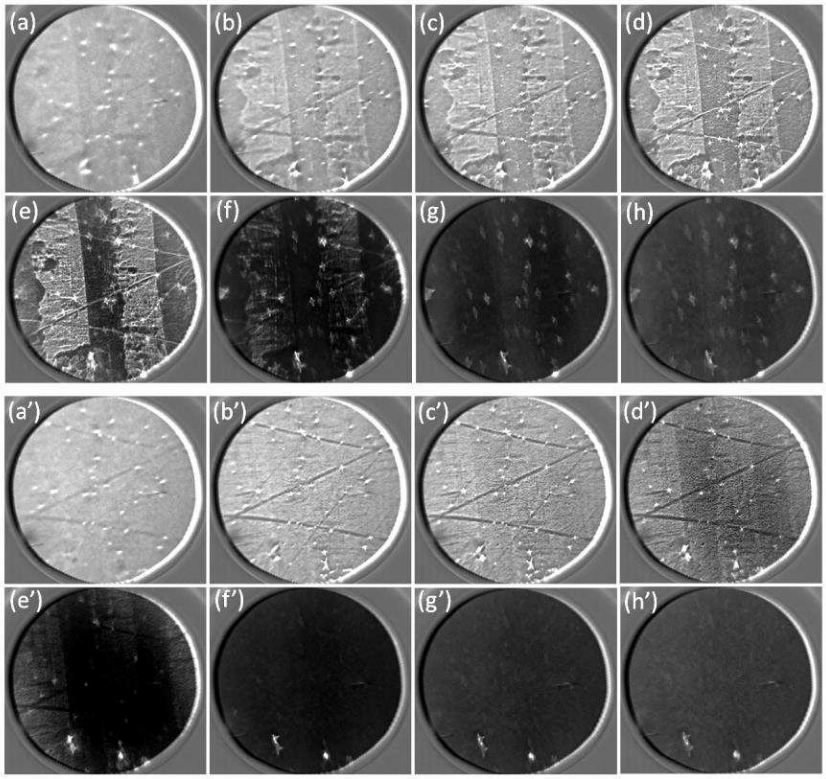


**Figure 6-4.** MEM-LEEM images with start voltage of (a) -4, (b) -3.5, (c) -3, (d) -2.5, (e) -2, (f) -1.5, (g) -1 and (h) -0.5 V, with (a')-(h') and without (a)-(h) UV illumination.

The average value of the MEM-LEEM transition shifts by $\Delta V_{off,\ on} = 0.46V$ to lower start voltage when illumination is switched on. This is due to the UV-induced photoemission positively charging the surface. The MEM-LEEM transition measures only a potential change perpendicular to the surface, therefore, in the case of in-plane polarization only a photoemission induced shift to lower start voltage would be expected with no screening by electron hole pairs. As the effect reported by Shao et. al., when the UV light is switched on during imaging in contact mode, rapid 180° domain wall motion is visible in consecutive PFM images as presented in Figure 6-5.

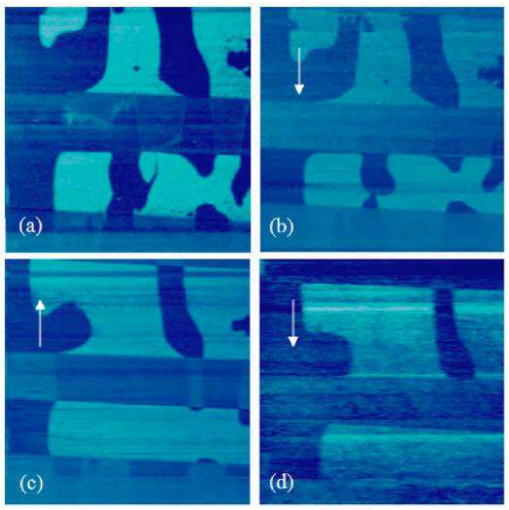


**Figure 6-5.** (a) PFM phase image of domains in $BaTiO_3$. (b)-(d) Consecutive images showing the motion of 180° domain walls during UV illumination as imaged with PFM. The arrows indicate the slow scan direction. The scan rate is 2 min and 50 s per frame. (This figure is reproduced from [Shao2006])

### 6.3.2 $BaTiO_3$ single crystal surface charge dynamics

To study the surface charge screening dynamics, we recorded fixed start voltage (-1.8 V) MEM images at 1 frame per second under UV illumination. The time dependence of the domain intensity contrast, defined by $\Delta I=I(P^+)-I(P^-)$, when the UV light is switched on and off in Figure 6-6. By fitting the data using an exponential dependence of $\Delta I$ versus time, i.e. $\Delta I = A + B \exp(-t/\tau)$ we obtain time constants $\tau_{on}$=41.3 s for light-on and $\tau_{off}$=104.2 s for light-off processes. These values are several times greater than those found by Shao et al.[Shao2006] with a lower power UV lamp. However, in our case the BTO, has been vacuum annealed for 3 hours at 700°C creating a significant concentration of Vo which could act as charge traps [Papageorgiou2010] and increase the time constant to attain the steady state.

Under UV illumination, electron-hole pairs are generated mainly near the surface because of the large cross section of photo-excitation in the UV range. Under the effect of the internal polarization field, electrons (holes) drift to the $P^+$ ($P^-$) surface and some are can be trapped in vacant trap states. Thus a space-charge field opposing the polarization field increases until it is equal to the polarization field or until the rate of electron-hole pair generation equals that of recombination. When

the light is switched off, the trapped carriers are thermally activated and diffuse along the concentration gradient to eventually recombine.[Shao2006] The spatial redistribution and retrapping of photo-carriers result in the observed exponential decays.

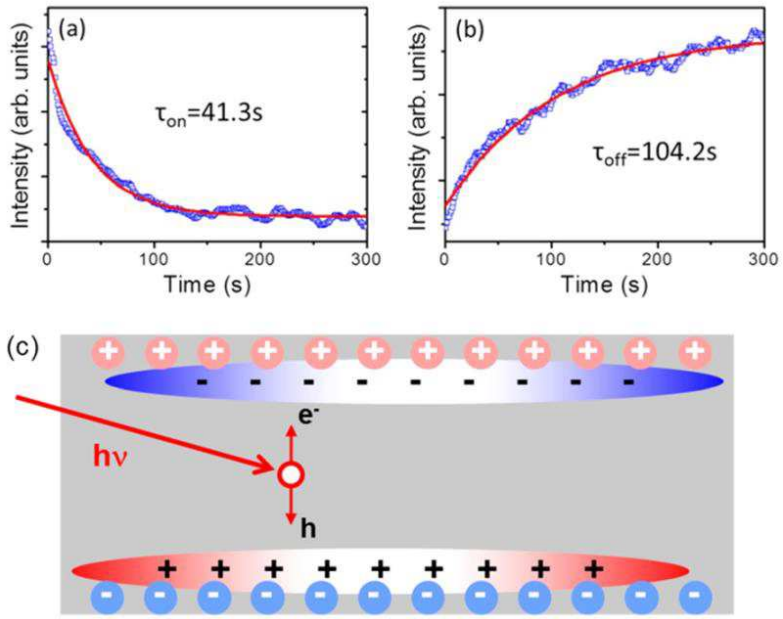


**Figure 6-6.** Time dependence of surface potential contrast ΔI between $P^+$ and $P^-$ domains immediately after UV light is switched (a) on and (b) off. (c) Schematic showing the drift of photogenerated charge carriers in an out of plane polarized ferroelectric slab.

### 6.3.3 $BaTiO_3$ single crystal with water exposure

In order to compare the screening efficiency of the super band-gap photo-generated carriers with extrinsic screening, we have carried out the same dynamical experiment following dissociative water adsorption on the BTO surface. The right hand inset of Figure 6-7 shows a MEM image taken at a start voltage of -2.2 V from the sample after a water exposure of to 3.6 $\times 10^5$ L. A net decrease in contrast between $P^+$ and $P^-$ domains was observed with respect to the dry surface in Figure 6-3. The reflectivity curves in Figure 6-7 show that the surface charge is indeed screened by dissociative water adsorption, reducing the $P^+/P^-$ surface potential shift to only 75 mV. At higher start voltage, the reflectivity is flatter than in Figure 6-3 due to a slight misalignment of the LEEM but it does not affect the differences measured in the electrostatic potentials above the $P^+$ and $P^-$ domains. Thus, the high

screening following 3.6 × $10^5$ L dissociative water adsorption is similar to that obtained in steady state conditions of UV photo-generated charge. After 1 h exposure to UV light, the MEM image is shown in the left hand inset of Figure 6-7. Again, the domain structure did not change after UV exposure but the $P^+/P^-$ surface potential shift has decreased to 50 mV.

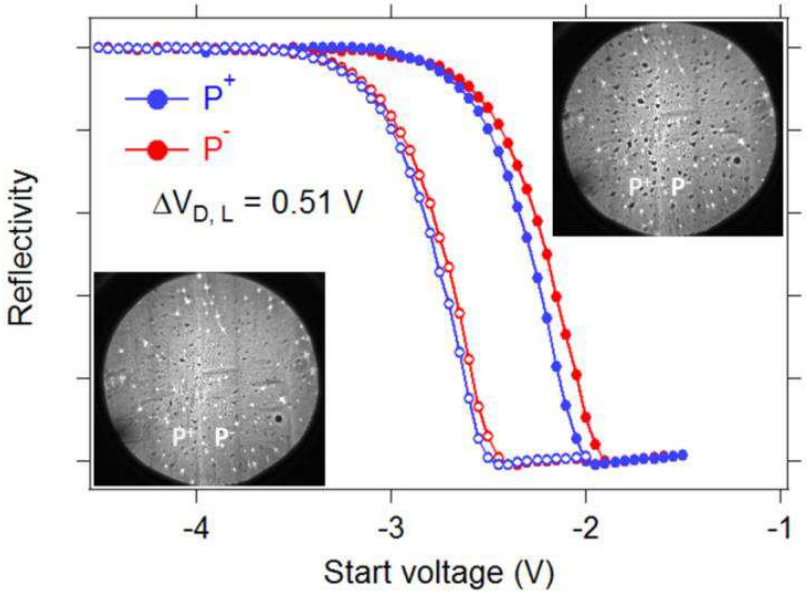


**Figure 6-7.** Right-hand inset: MEM image at a start voltage of -2.2V showing the contrast in electrostatic potential above differently polarized domains of the BTO(001) surface after dissociative water adsorption. Left-hand inset: same in steady state conditions after UV illumination. Main figure: reflectivity curves extracted from Pþ and Pdomains as a function of start voltage before (full symbols) and after (open symbols) UV illumination.

Our initial surface was almost carbon free and gives rise to a large shift, 400 mV, in the electrostatic potential above oppositely polarized domains. The crucial importance of adsorbates at ferroelectric surfaces is underlined by the high screening following 3.6x$10^5$ L dissociative water adsorption similar to that obtained in steady state conditions of UV photo-generated charge. These experiments also show that screening by free carriers is a reversible process which, in the experimental conditions used, does not affect the domain structure. Indeed, the observed stripe domain structure with 180° domain walls is one way for the system to minimize its energy. The depolarizing field in one domain is screened by the fields from adjacent domains. However, since our MEM-LEEM experiments probe only the electrostatic potential due to the surface charge, they are not affected by

screening from the adjacent domains which act as an external field on the domain in question. Thus we can quantify the difference in surface potential between adjacent domains. The time constant for screening is longer than that measured on unannealed samples and suggests that charge dynamics are strongly dependent on the surface chemistry, in particular on the oxygen vacancy concentration.

## 6.4 Conclusion

MEM-LEEM has been used to directly observe photocarrier and water adsorbate screening effect on a clean, vacuum annealed $BaTiO_3$ (001) surface. Surface potential contrast between $P^+$ and $P^-$ domains is significantly reduced under UV illumination by photo-generated carrier screening. Contrast is recovered without changes in domain structure after illumination is switched off. Dissociative water adsorption on on-top cation sites is similarly efficient in screening the surface charge. The surface charge dynamics are dominated by drift on UV illumination and thermal diffusion after the UV light is switched off. The time constant for screening is longer than that previously measured on unannealed samples in air and suggests that charge dynamics are strongly dependent on the surface chemistry, in particular, on the Vo concentration.

# Chapter 7

# Surface atomic and chemical structure of $Sr_{0.67}Ba_{0.33}Nb_2O_6$ (001) single crystal

## 7.1 Introduction

Strontium niobate is treated as high performance water splitting photocatalysts due to the special structure construction in which [$NbO_6$] octahedral is distortable, and thus the charge separation photo-generated electrons and holes can be enhanced by the dipole moment.[Kudo2000] Meanwhile the fairly high energy level of Nb 4d is beneficial for the potential hydrogen production by water splitting.[Chen2009, Kudo2000] The charge separation can be enhanced in materials with ferroelectric properties.[Kohno1997] Ferroelectric strontium barium niobate is expected to be a good water splitting photocatalysts. The ferroelectricity in strontium barium niobate is axial and thus involves only up and down domains. Under UV illumination, the charged surface state can separate electron-hole pairs more efficiently and it can enhance local photochemical reactions. Therefore, Strontium barium niobate could provide a new and efficient mode of hydrogen production, either as non-polluting combustible or in fuel cells.

In this chapter, we report an experimental study of the $Sr_{0.67}Ba_{0.33}Nb_2O_6$ (SBN) (001) single crystal surface. Tetragonal tungsten bronzes (TTBs), as an important structure type of ferroelectric materials, have been widely investigated because of their outstanding pyroelectric, piezoelectric, and nonlinear optical properties. [VanUitert1968] In particular, much interest has been devoted to $Sr_{1-x}Ba_xNb_2O_6$ (SBN) due to its excellent electro-optical properties.[Dörfler1999, Lenzo1967, Ewbank1987, Horowitz1993, Cuniot-Ponsard2011] SBN is a ferroelectric material with spontaneous polarization along c-axis of the TTB-like structure. [Jamieson1968] The Curie temperature, dielectric constant, and P-E hysteresis, can be varied by changing the Sr/Ba atomic ratio in the range of $0.25<x<0.75$. [Tanaka1998] For example, the Curie temperature varies from 60 to 250 °C for x

values of 0.25 and 0.75, respectively.[Qu2002] Nevertheless, most of these studies focus on crystal growth or optical and electrical characterization.[Cuniot-Ponsard2003, Tanaka1998, Zhang2013] To our knowledge, there have been as yet few investigations of surface chemistry and structure.

The $Sr_{1-x}Ba_xNb_2O_6$ solid solution is formed in the concentration range of ~0.2-0.8 and has tetragonal tungsten bronze (TTB) structure in which one of the cation sites is not completely filled.[Kim2002, Chernaya2000] The unit cell can be described by the general structural formula $[(A1)_2(A2)_4C_4][(B1)_2(B2)_8]O_{30}$, where A and B represent the different cation sites. The SBN structure is built up of two types of crystallographically independent $NbO_6$ octahedra joined via oxygen apices into a three-dimensional network. In this network, there are three types of structural channels running along the polar c axis. The narrowest triangular channels (type C channels) with 9-fold oxygen coordination sites are empty, the intermediate tetragonal channels (A1) with 12-fold oxygen coordination are occupied only by the Sr atoms, and the largest, pentagonal channels (A2) with 15-fold oxygen coordination sites are filled by Ba or Sr atoms.[Chernaya2000, Belous2007] Variation of the [Sr]/[Ba] atomic ratio shifts the temperature of the FE to PE phase transition, changes the permittivity, and modifies the relaxor properties of SBN.[Belous2007] The stoichiometry alters both the A1 and the A2 occupancy, however, it should be noted that regardless of the [Sr]/[Ba] ratio, 1/6 of the A (A1+A2) sites, in the SBN structure are empty. [Podlozhenov2006] B1 and B2 sites are fully filled with Nb atoms. A schematic of the (001) surface is shown in Figure 2-7. Each unit cell contains 2 tetrahedral A1 and 4 pentagonal A2 sites.

## 7.2 Experimental section

The $10 \times 10 \times 0.6$ $mm^3$ SBN(001) single crystal with nominal Sr concentration of 0.6 was furnished by SurfaceNet GmbH. To eliminate surface carbon contamination, the sample was ozone-cleaned by a short, 10 minute exposure to UV light in air before being introduced into the ultra-high vacuum (UHV) set-up. Then it was annealed at 700 °C for 1 hour at a base pressure of $1 \times 10^{-9}$ mbar to remove residual contamination on the surface such as $H_2O$ or $CO_2$ to ensure a nearly adsorbate free surface following the procedure for BTO single crystal as in chapter 4.[WangJ2012]

LEED and XPS analyses were performed in-situ in the same UHV set-up, with a base pressure of $2 \times 10^{-10}$ mbar. XPS was carried out using a monochromatic Al Kα (1486.7 eV) X-ray source (Omicron Nanotechnology GmbH). The overall energy resolution (photons and spectrometer) was 0.35 eV. The data were analyzed using the CasaXPS software[CasaXPS] which employs a linear least squares optimization with a peak fitting algorithm. Shirley backgrounds were subtracted from the data as part of the curve fitting process.

## 7.3 Results and discussion

### 7.3.1 LEED

Figure 7-1(a) presents the LEED pattern obtained for SBN(001) sample. The LEED pattern was measured at an energy of 45 eV to maximize surface sensitivity. The [100] direction of the SBN sample is 45° from horizontal. The sample has a very well-defined LEED pattern showing the square symmetry structure of the SBN(001) surface and reveals a high crystalline quality. The LEED schematic presented in Figure 7-1(b) is obtained from the superposition of two reconstructions: $(\sqrt{5} \times \sqrt{5})R26.6^\circ$ (red spot) and $(5\sqrt{2} \times \sqrt{2})R45^\circ$ (green spot).[Borg2002, Jaworowski2002] As mentioned before, 1/6 of the A-type sites in the SBN structure are empty. Two kinds of reconstruction, $(\sqrt{5} \times \sqrt{5})R26.6^\circ$ and $(5\sqrt{2} \times \sqrt{2})R45^\circ$, can be formed because of different distribution of empty A-type sites (Figure 7-2). The $(\sqrt{5} \times \sqrt{5})R26.6^\circ$ is produced by ordering of the voids on the A1 cation sites whereas the $(5\sqrt{2} \times \sqrt{2})R45^\circ$ reconstruction comes from ordering of voids on the A2 site. The simultaneous observation of these two surface reconstructions implies that the A-site voids are not randomly distributed but have two long range order states.

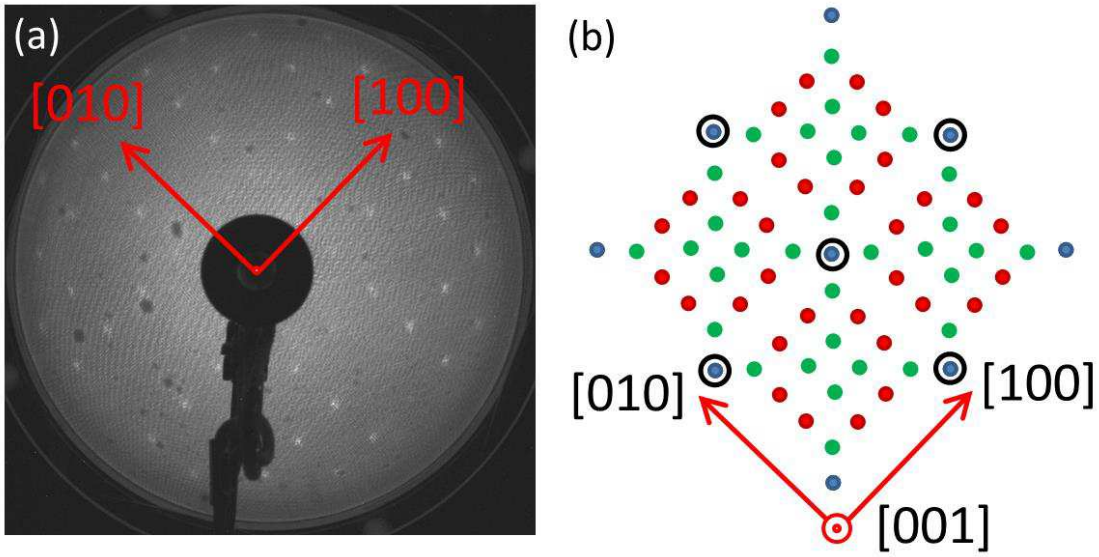


**Figure 7-1.** (a) LEED image on SBN(001) single crystal surfaces at 45 eV; (b) Schematic LEED diffraction pattern showing superposition of two patterns, (√5 ×√5)R26.6°(red) and (5√2 ×√2)R45°(green). The points to both reconstruction are marked by blue color and the (1 × 1) pattern is marked by black circles.

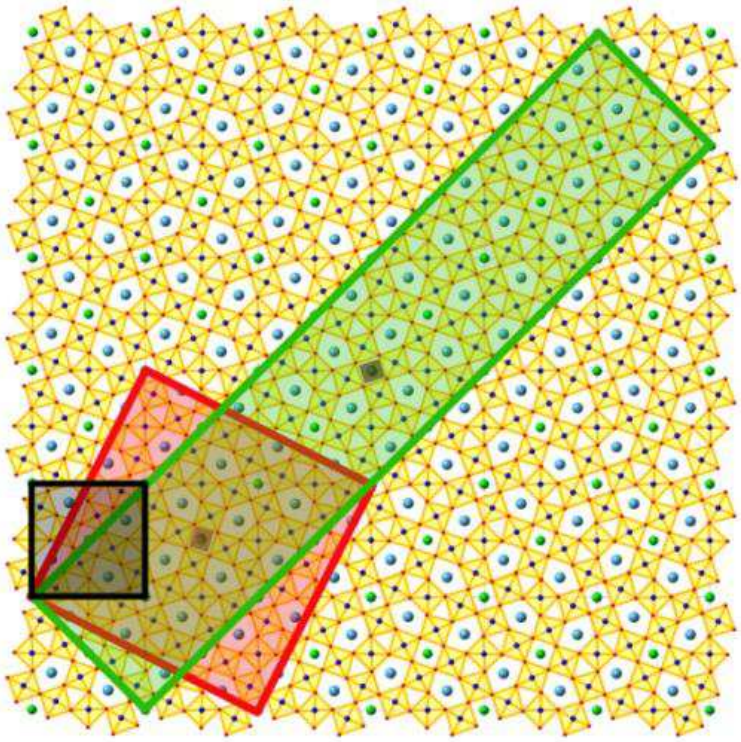

**Figure 7-2.** Schematic diagram showing the SBN cell (black), (√5 ×√5)R26.6° (red) and (5√2 ×√2)R45° (green) reconstruction due to different distribution of empty A1 site. Two void sites are indicated by the small shaded squares.

### 7.3.2 XPS

Figure 7-3(a) shows an XPS survey spectrum for the SBN surface. The C 1s peak is below the detection limit in XPS showing that the surface is clean with very low carbon contamination. The Ba $3d_{5/2}$, Sr 3d, Nb 3d and O 1s core level spectra are shown in Figure 7-3(b)-(e) at normal and grazing (60°) emission.

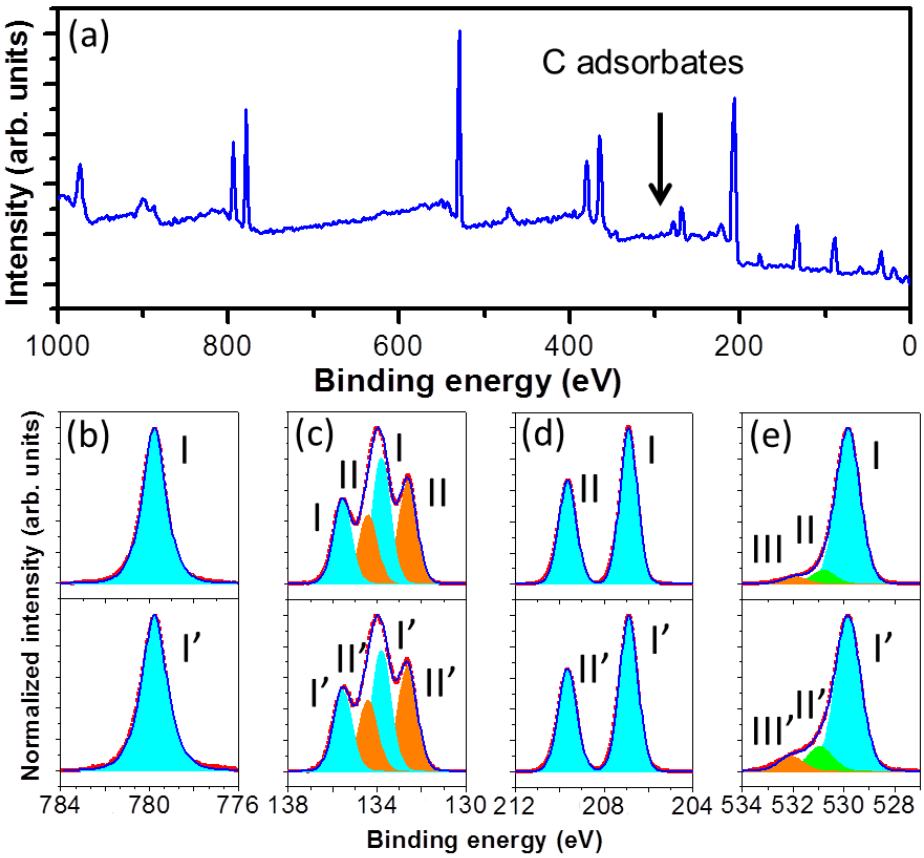


**Figure 7-3.** (a) Survey XPS scan of SBN(001) single crystal. Core level spectra: (b) Ba 3d5/2; (c) Sr 3d; (c) Nb 3d; (d) O 1s core level spectra at normal (top) and 60° (bottom) incidence angles.

The high resolution spectra of Ba $3d_{5/2}$ are shown in Figure 7-3(b). The spectra have only one main component, labeled I, with a binding energy (BE) of 779.8 eV and is due to bulk-coordinated Ba.

The Sr 3d spectra are presented in Figure 7-3(c). The main peaks, labeled I, have a binding energy (BE) of 133.8 eV ($3d_{5/2}$) and 135.6 ($3d_{3/2}$) respectively. Each spectrum also has a component labeled II, shifted by 1.2 eV to lower binding

energy (LBE). The grazing emission angle spectrum shows that this LBE component is a slightly more intense at the surface. The appearance of LBE satellite peaks is also observed on $Ba_{0.5}Sr_{0.5}Co_xFe_{1-x}O_{3-\delta}$ with oxygen deficiency. [Jung2011] However, the ratio of $[Sr]_I/[Sr]_{II}$ = 1.38. The concentration of oxygen vacancies is almost 2.3 %, If the LBE peak is due to an oxygen deficiency, and assuming that one oxygen vacancy reduces two cations then this would imply an oxygen vacancy concentration of 2.3 % with respect to the total number of oxygen atoms. This is obviously not correct here, because the sample remains transparent at all times and, as shown below, there is no evidence in the valence band spectra for a high density of states due to oxygen vacancies. Therefore, the intensity difference is not enough to ascribe component II to a purely surface state. Rather, it corresponds to a different chemical environment present both at the surface and in the bulk. Since strontium atoms are distributed on two different crystal sites, A1 and A2, which have different chemical surroundings[Jamieson1968] that might be the reason for the observed split of two Sr spectra. The quantitative interpretation of the Sr I and II components will be discussed below.

The Nb 3d XPS spectra in Figure 7-3(d) have peaks at 206.9 and 209.6 eV due to the spin-orbit splitting with a formal valence of 5+. There is no low binding energy (LBE) component which would be representative of reduced Nb formed under oxygen-deficit conditions, for example $Nb^{4+}$ or lower valency. This is reasonable because lower Nb valence states are known to oxidize to $Nb^{5+}$ at room temperature.[Atuchina2005, Singh2008]

Figure 7-3(e) shows the O 1s spectra. The spectrum has three components, peak I at 529.8 eV is due to oxygen in the perovskite-like environment, and peaks II (530.8 eV) and III (531.9 eV). As can clearly be seen from the comparison of bulk and surface spectra and contrary to the Sr 3d spectra, both $O_{II}$ and $O_{III}$ are of surface origin. OII may be attributed to oxygen in lattice positions coordinated with a proton as in chapter 4, whereas $O_{III}$ is ascribed to hydroxyl groups chemically bound to surface cations,[Baniecki2006] even present in some “dry” samples. [Wendt2006]

From the relative intensities of the Ba $3d_{5/2}$ and Sr $3d_{5/2}$ core-level components, we can determine a [Sr]/[Ba] = 2/1 ratio based on a reasonable estimate of the photoelectron inelastic mean free path,[NIST] where the cross-sections and

inelastic mean free paths for Sr (Ba) are 0.06934 (0.6036) and 1.78 (1.085) nm, respectively. From single-crystal X-ray measurements, the site-occupancy factors for the A1 and A2 sites was derived to be ~70 % and ~90 % respectively whatever the Sr/Ba ratio.[Podlozhenov2006] So the general structural formula changes to $[(A1)_{1.4}(A2)_{3.6}C_4][(B1)_2(B2)_8]O_{30}$.

For a chemical formula of $Sr_{0.67}Ba_{0.33}Nb_2O_6$, the general structural formula can therefore be written as $[(Sr_{1.4})_{A1}(Sr_{1.93})_{A2}(Ba_{1.67})_{A2}][(Nb_2)_{B1}(Nb_8)_{B2}]O_{30}$. This gives a ratio of Sr in the two A sites, $[Sr]_{A2}/[Sr]_{A1}=1.38$.

For Sr 3d core-level, the $[Sr]_I/[Sr]_{II}$ intensity ratio is 1.21 (1.15) for the bulk (surface), 12 % (17 %) less than the value expected from the stoichiometry as determined by XPS. We suggest that the difference may be due to the partial reduction of the A1 site Sr by the formation of oxygen vacancies, reducing the HBE intensity and reinforcing the LBE intensity in the Sr 3d spectrum. In a simple charge-transfer model, one Vo could result in the reduction of two Sr atoms ions to lower valence, based on the assumption that charge transfer occurs principally from Vo to Sr because of its larger Pauling electronegativity than Ba. Although we have no direct way of measuring the Vo concentration, we do know they are formed by UHV annealing. Circumstantial evidence for a non-negligible Vo comes from the complete absence of sample charging during XPS analysis. Furthermore the formation energy is expected to be lower at the surface than in the bulk. As previously mentioned, $Nb^{4+}$ will oxidize to $Nb^{5+}$ at room temperature, so all the charges transfer from oxygen vacancies, Vo, to Sr atoms.

From the chemical formula, $Sr_{0.67}Ba_{0.33}Nb_2O_6$, in the framework of this simple charge-transfer model we obtain the following expressions related to the intensities of two Sr core-level peaks:

$[Sr]_I+[Sr]_{II}=0.67$

$([Sr]_I-2Vo)/([Sr]_{II}+2Vo)= 1.21\ (1.15)$

The bulk and surface Vo concentration can therefore be estimated to be 0.2 and 0.26 % respectively.

Finally, the valence band (VB) XPS spectra of bulk and surface are reported in Figure 7-4. The blue and red curves are taken at normal and 60° emission angles, respectively. There is nearly no change between the valence band in bulk and at surface, which is consistent the conclusion of XPS results of low concentration of oxygen vacancies and supports the interpretation of the two Sr 3d core level components as being due to distinct chemical sites.

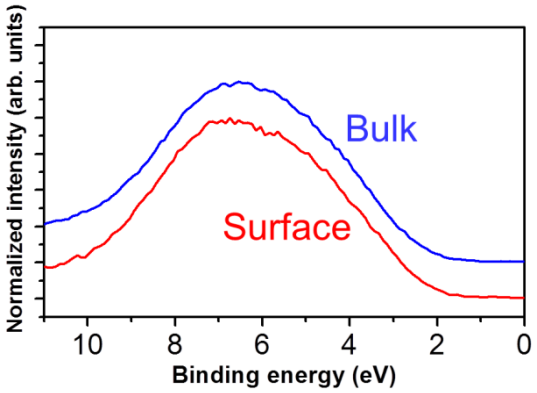


**Figure 7-4.** Valence band spectra of the SBN crystalline at normal (blue) and 60° incidence angles (red) emission.

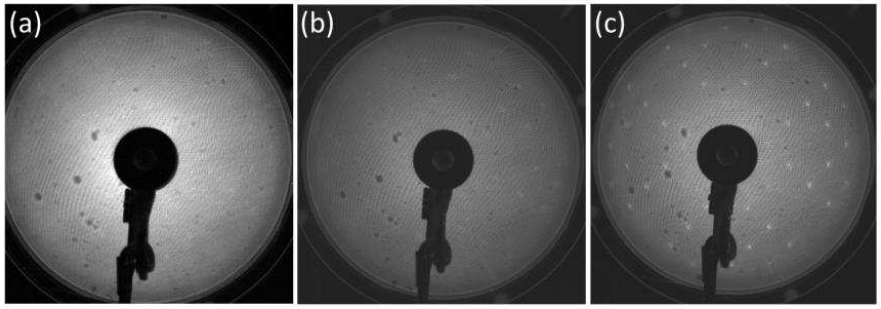


**Figure 7-5.** LEED images on $Sr_{0.6}Ba_{0.4}Nb_2O_6(001)$ single crystal surfaces annealed at (a) 300 °C, (b) 500 °C and (c) 700 °C at 45 eV.

In order to check the LEED pattern observed, thus surface structure, is special for a SBN with certain Sr/Ba ratio or it's the general behavior of SBN surface, a serie of LEED patterns were done on a $Sr_{0.6}Ba_{0.4}Nb_2O_6(001)$ annealed with different temperature. the LEED images on $Sr_{0.6}Ba_{0.4}Nb_2O_6(001)$ single crystal surfaces annealed at 300 °C, 500 °C and 700 °C are shown in Figure 7-5 (a)-(c) at 45 eV. The LEED spots get brighter as annealing temperature increases, however, the structure does not change. Since all the structures are the same, we rule out the

possibility that the LEED pattern is due to a SBN with certain ratio, and thus our results manifest the general behavior of this SBN surfaces.

## 7.4 Conclusion

In conclusion, LEED and XPS have been used to study the surface atomic and chemical structures of a $Sr_{0.67}Ba_{0.33}Nb_2O_6$ (SBN) (001) single crystal. A well-defined $(\sqrt{5} \times \sqrt{5})R26.6^\circ + (5\sqrt{2} \times \sqrt{2})R45^\circ$ LEED pattern is presented, which is due to the surface reconstruction because of alkaline earth metal void in A sites. The split of Sr 3d core level into 2 components suggests two different crystal sites, A1 and A2, with different chemical surroundings. The quantitative XPS analysis shows excellent agreement with the structural model deduced from the LEED. We have therefore a consistent chemical and structural analysis of the SBN(001) surface which should be invaluable in understanding the ferroelectric properties of, for example, strain engineered thin films.

The ferroelectricity in SBN is axial and thus with only up and down domains. The charged surface state can separate electron-hole pairs more efficiently under UV illumination, which can enhance local photochemical reactions. Meanwhile, due to the fairly high energy level of Nb 4d which beneficial for the potential hydrogen production by water splitting, SBN is treated as high performance water splitting photocatalysts and could provide a new and efficient mode of hydrogen production.

# Chapter 8

## General conclusion and perspective

The main objective of this work was to understand how the ferroelectric polarization affects the chemi/physisorption of $H_2O$ molecules on a ferroelectric surface and how this adsorption may in return affect the chemical and the atomic structure of ferroelectrics and hence the ferroelectric properties.

Firstly, we present a study of the atomic and chemical structure on the surface of strained, $TiO_2$-terminated, ferroelectric $BaTiO_3$ (001) epitaxial films on a $SrTiO_3$ substrate, before and after controlled exposure to water.

For an as-received fully compressively strained BTO(001) thin film, it has a $P^+$ polarization. The average polarization over the first two unit cells before water adsorption is $P^+$, pointing vertically toward the surface. However, the rumpled top $TiO_2$ layer has a downward pointing electric dipole, opposite to that of the bulk polarization. This is evidence that to stabilize polarization in the thin film, the first $TiO_2$ atomic layer corrugates and creates a dipole opposite to the bulk polarization to compensate the ionic surface polarization charge. The inversion of the electric dipole at the surface has already been observed for an ultrathin, BaO-terminated BTO film grown on $SrRuO_3$.[Shin2009]

After water exposure, the adsorption of $OH^-$ at on-top Ti surface atom sites switches the dipole of the surface $TiO_2$ layer back in the direction of the bulk polarization. Thus $OH^-$ stabilizes the $P^+$ polarization state. $H_2O$ undergoes mainly dissociative adsorption on the polarized BTO(001) surface. There are two dissociative adsorption sites, oxygen vacancies and on-top surface Ti. The Ti on-top site is the dominant site for $OH^-$ chemisorption.

For the adsorption of $H_2O$ on $TiO_2$-terminated BTO(001) films with different strains, the predominance of dissociative adsorption is confirmed by both XPS and TPD. The on-top $OH^-$-Ti dominates the chemisorption process. The desorption energy of water increases with the diminution of in-plane strain. Since the experimental spontaneous polarization increases with the increasing film thickness, thus diminution of in-plane strain, the higher film polarization in the thicker films

favours water adsorption because it screens more efficiently the depolarizing field and provides a higher desorption energy.

We have also investigated the surface of a ferroelectric $BaTiO_3$ (001) single crystal. After ex-situ cleaning and in-situ annealing in oxygen the surface is atomically flat with a preferential BaO-termination and a (1 × 1) surface structure. Three kinds of domains, $P^+$, $P^-$, and $P^{in}$, were founded. Meanwhile, the rumpling is smaller at the surface than in the bulk, suggesting that both domain ordering and surface structural changes contribute to screening of the polarization.

Surface potential contrast between oppositely polarized ferroelectric domains, $P^+$ and $P^-$, is significantly reduced under UV illumination by photo-generated carrier screening. UV illumination generates electron-hole pairs near the surface because of the large photo-excitation cross section. Under the internal polarization field, electrons (holes) drift to the $P^+$ ($P^-$) surface and some are trapped in vacant trap states. Thus, a space-charge field opposing the polarization field increases until equal to the polarization field or until the rate of electron-hole pair generation equals that of recombination. Dissociative water adsorption on on-top cation sites is similarly efficient in screening the surface charge.

Surface polarization charge in ferroelectric materials can be screened by a variety of mechanisms: intrinsic (charge carriers or defects in the bulk), extrinsic (chemical environment or adsorbates), domain ordering, or even a combination of the above. Chemisorption of $OH^-$ and protons can lead to important changes in the electrical boundary conditions and water film can play an active role in domain switching. Photo-generated charge carriers can also efficiently screen the surface and interface polarization charge and hence the depolarizing field. The domain ordering reduces the energy of the system by screening the depolarizing field through ordering of the ferroelectric domains with antiparallel dipole moments. The depolarizing field in one domain is screened by the electric fields of adjacent domains.

Finally, the surface atomic and chemical structures of a $Sr_{0.67}Ba_{0.33}Nb_2O_6$ (SBN) (001) single crystal are discussed. A well-defined ( $\sqrt{5} \times \sqrt{5}$)R26.6° + (5 $\sqrt{2} \times \sqrt{2}$)R45° LEED pattern is presented, which is due to the surface reconstruction because of alkaline earth metal void in A sites. The split of Sr 3d core level into 2

components suggests two different crystal sites, A1 and A2, with different chemical surroundings. The quantitative XPS analysis shows excellent agreement with the structural model deduced from the LEED.

The ferroelectricity in SBN is uniaxial and thus with only up and down domains. The charged surface state can separate electron-hole pairs more efficiently under UV illumination, which can enhance local photochemical reactions. Meanwhile, due to the fairly high energy level of Nb 4d which beneficial for the potential hydrogen production by water splitting, SBN is treated as high performance water splitting photocatalysts and could provide a new and efficient mode of hydrogen production. Therefore the consistent chemical and structural analysis of the SBN(001) surface which we have done should be invaluable in understanding the ferroelectric properties of, for example, strain engineered thin films.

To further explore the interaction between water and ferroelectric surface, some open questions remain. Our analysis is based on the differences between a slightly defective single domain, epitaxially strained BTO film before and after a controlled water adsorption experiment. The presence of adsorbate-related $O_{II}$ and $O_{III}$ components in the XPS spectra of the as-received sample show that $OH^-$ units are already present, either at the surface or in the bulk of the film. This $OH^-$ incorporation could occur during film growth but may also be due to uptake of residual hydrogen in UHV. More efforts are certainly needed to perfect the growth and analysis conditions. Physisorption is enhanced by higher Vo concentration, whereas preferential $OH^-$ chemisorption occurs at on-top surface Ti sites. The $H_2$ yield of the dissociation process also needs to be quantified. Similar experiments on a single $P^-$ domain, known to be favored by Vo, should also be carried out. These results could be of interest for many applications requiring control of the surface polarization state, for example, the formation of interfaces for magnetoelectric coupling between a ferroelectric and a magnetic oxide or to enhance surface reactions such as water photolysis, which uses precisely the reaction described here.

The formation of nanoscale 180° domains with the polarization that is parallel to the c-axis of the SBN crystal has been observed, the growth condition for epitaxial thin film need to be tried in order to fabricate SBN films with different domain structures.

# Appendix A

# Ferroelectricity in a quasi-amorphous ultrathin $BaTiO_3$ film

## A.1 Introduction

For a long time, it was believed that spontaneous polarization existed only in ionic crystals due to a noncentrosymmetrical spatial distribution of ions in a polar crystalline structure. This commonly accepted idea now needs to be reconsidered following the discovery of noncrystalline pyro- and piezoelectric-phase thin films of $BaTiO_3$ (BTO), $SrTiO_3$ (STO), and $BaZrO_3$ (BZO).[Lyahovitskaya2003, Ehre2007]

The subsequent investigation of this new phase, called quasi-amorphous (QA), revealed that the amorphous material contains a network of randomly connected, slightly distorted octahedral local bonding units (LBU), such as $TiO_6$ or $ZrO_6$, that can be polarized along an axis corresponding to the strain in 50-250 nm films on Si or $SiO_2$ during annealing (Figure A-1).[EhreD2007, Ehre2008, Frenkel2005, Frenkel2007, Lyahovitskaya2005] The material must contain one cation forming stable LBUs and a second cation capable of stabilizing underbonded oxygen. X-ray absorption near edge spectroscopy (XANES) has been used to determine the Ti off-center displacement of 0.44 Å.[Frenkel2005]

Extended x-ray absorption spectroscopy of the QA phase showed that the $TiO_6$ octahedra are deformed by less than 4 %. The $TiO_6$ octahedra are both apex and edge sharing in the amorphous and QA phases. The polarity is the result of the orientational ordering of the LBUs without any detectable spatial long-range order. Alignment of 5 % of the LBUs is sufficient to create a macroscopic polarization. This opens up a new direction for FE material design no longer limited to crystalline compounds. However, ferroelectricity in quasi-amorphous phases has not yet been reported nor has the QA phase in ultrathin device compatible films been observed.

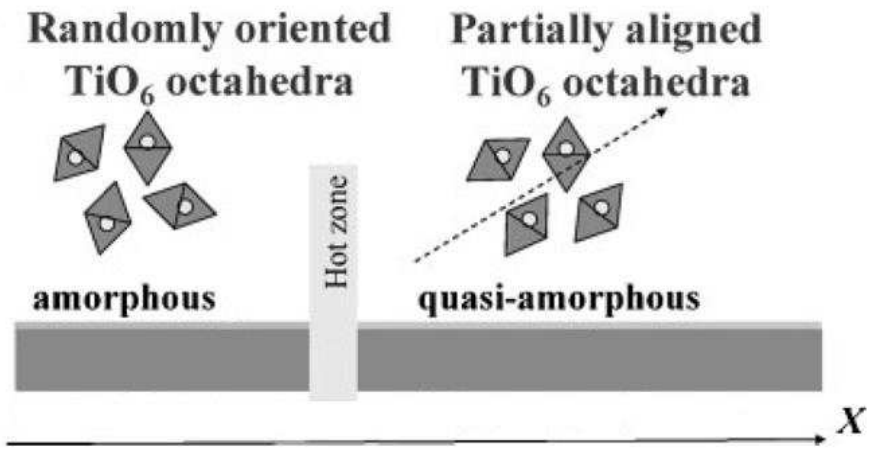


**Figure A-1.** Scheme of the development of the stress and strain gradient in a $SrTiO_3$ or $BaTiO_3$ film pulled in the x-direction through a temperature gradient. (This figure is reproduced from [Wachtel2010])

In this chapter, PFM has been used to write and read stable ferroelectric domains on such a QA film. The phase signal image shows a clear electrical contrast, corresponding to stable, antiparallel FE domains.[Fujisawa2005] P-E hysteresis demonstrates that the ultrathin QA BTO film is ferroelectric. XRD proves the absence of long-range order. Angle-scanned XPD is used to probe elemental-specific local distortions at the surface of ferroelectric materials and is used to confirm the amorphous nature of the QA film. XPS proves the chemical and electronic structure of thin films. Here, it reveals significant differences between the ultrathin QA film and the thicker films already reported.[Ehre2008] The results establish a method to form ultrathin, quasi-amorphous ferroelectric BTO on STO by homogeneous postannealing in $O_2$ flow.

## A.2 Experimental section

The commercial STO(001) substrate with an optical mirror surface finish was etched with buffered $NH_4$-HF solution (BHF) of pH ~5.5 for 10 min, rinced by deionized water and dried in $N_2$ stream. Then it was annealed at 950 °C in $O_2$ flow for 10 hours to obtain the $TiO_2$ termination surface composed of one unit-cell steps and atomically flat terraces following the established protocol.[Kawasaki1994]

After heating the substrate to 650 °C for 1 hour under an oxygen partial pressure of $\sim 10^{-6}$ Torr to remove carbon contamination on the surface, two ultrathin BTO films were grown on these substrates by molecular beam epitaxy (MBE) with a growth rate of ~0.5 monolayers (ML)/min and ~1 ML/min, respectively. The metallic Ba and Ti were put in the Knudsen cells heated by a resistance coil to produce the vapor flux. During growth, the oxygen partial pressure was kept at $2 \times 10^{-6}$ Torr and the substrates were maintained at room temperature. After deposition, the samples were annealed at 700 °C in $O_2$ flow for 1 hour.

The crystalline or amorphous state of the samples was measured by high-resolution x-ray diffraction (six-circles Rigaku SmartLab diffractometer with rotative anode using Cu KαI line, $\lambda = 1.5406$ Å) at INL Lyon in the θ-2θ mode for in-plane and out-of-plane scans.

XPD was conducted on the ANTARES beam line at SOLEIL synchrotron. To determine the film structure, the Ti 2p XPD emission was measured over a wide range of polar and azimuthal angles with an angular resolution of ±1°. The photon energy was 900 eV giving low photoelectron kinetic energies and enhanced surface sensitivity. XPS was carried out using a Kratos Ultra DLD at SPCSI, CEA-Saclay, with monochromatic Al Kα (1486.7 eV). The analyzer pass energy of 20 eV gave an overall energy resolution (photons and spectrometer) of 0.35 eV. The sample is at floating potential and a charge compensation system was used. The binding energy scale was calibrated using the C 1s line at 284.6 eV as a reference. A take-off angle of 90°, i.e., normal emission, was used for all analyses presented. Thus the XPS probes the full BTO film thickness. Grazing angle emission was used to check the surface nature of the core-level peaks. The data were analyzed using the CASAXPS software,[CasaXPS] which employs a linear least-squares optimization with a peak-fitting algorithm. Shirley backgrounds were used and subtracted from the data in the curve fit.

Micron scale polarized FE domains were written by PFM by Dr. B. Gautier using a Bruker Dimension 3100 Atomic Force Microscope at INSA Lyon with conductive, platinum coated tips by applying a dc voltage (writing mode) and the phase signals were observed by applying an ac voltage (reading mode).

## A.3 Results

### A.3.1 AFM

Figure A-2(a) is the atomic force microscopy (AFM) topography image of the STO substrate done by Dr. L. Tortech showing clear terraces, with a single unit-cell step height. The uniform surface termination of the substrate terraces implies a homogeneous interface between the BTO layer and the substrate over the whole sample. Two samples were prepared using different growth rates. Figures 7-2(b) and 7-2(c) show the AFM images of the BTO films after annealing at a temperature of 700 °C in $O_2$. The thicknesses, as estimated from the Sr 3d core-level intensities (see discussion of Sr 3d XPS, below) were 3.2 nm (sample 1) and 3.8 nm (sample 2), grown at rates of 1 and 0.5 ML/min, respectively. The film quality is significant different. Sample 1 has large micrometer-sized pinholes, whereas sample 2 pinholes are smaller by between one and two orders of magnitude.

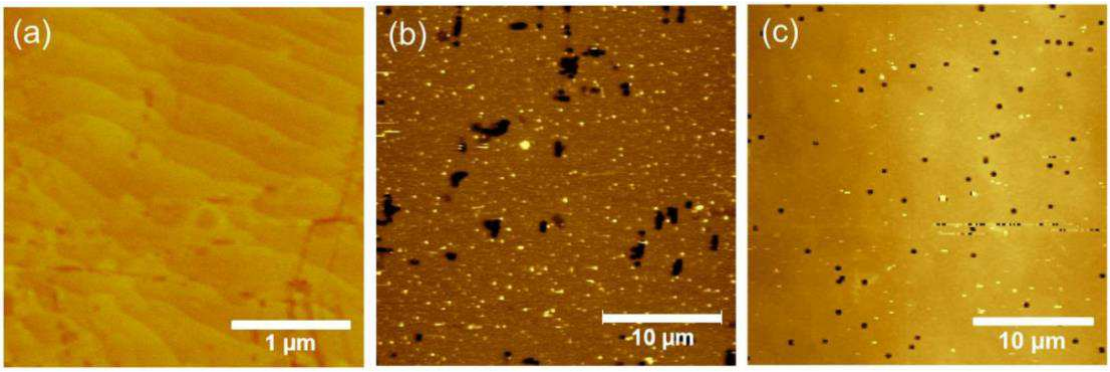


**Figure A-2.** AFM topography image of (a) STO substrate before growth of BTO; (b) sample 1 (crystalline BTO film); and (c) sample 2 (QA BTO film).

### A.3.2 XRD

Figure A-3 shows the XRD scans of the two BTO films. In the out-of-plane scans, the two main peaks located at $2\theta = 22.75°$ and 46.48° correspond, respectively, to the STO(001) and STO(002) reflections from the substrate. For sample 1 (upper curve), structures are observed at the low $2\theta$ angles with respect to the STO peaks position. Their calculated lattice parameter is 0.4037 nm, corresponding to that of fully relaxed BTO (0.4036 nm). The diffraction pattern of the lower growth rate film has no clear small-angle structure, although there

appears to be a very slight asymmetry or shoulder toward lower 2θ angles, discussed below. Thus there is no evidence for long-range order perpendicular to the surface distinct from that of the substrate.

The inset of Figure A-3 shows the in-plane XRD scans. One main peak is observed at 2θ = 32.38° corresponding to the STO substrate. In the case of sample 1 (upper curve in inset), we again observe a structure on the low-angle side of the STO peak, corresponding to an in-plane lattice parameter of 0.4010 nm, consistent with fully relaxed in-plane BTO. On the other hand, the in-plane scan of sample 2 (lower curve in inset), shows no XRD peak apart from that of the STO substrate, confirming the absence of a distinct crystalline phase in this BTO film. For a thin film with a free surface, there is no possible mechanism of isotropic pressure.

Thus the only explanation for the absence of a distinct XRD signal in and out of plane is that the BTO sample 2 has no long-range order, i.e., the BTO is amorphous.

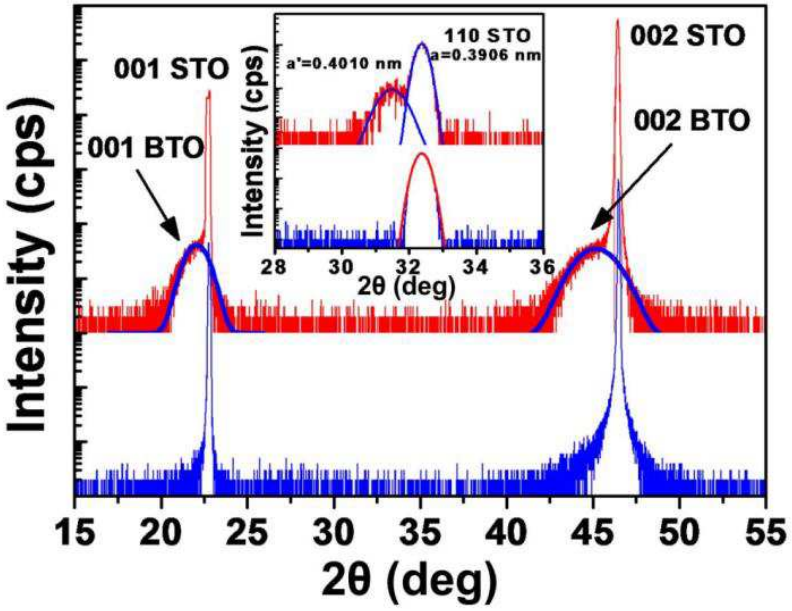


**Figure A-3.** Out-of-plane scan XRD spectra of sample 1 (upper) and sample 2 (lower) subsequently identified as crystalline and quasi-amorphous BTO films, respectively. The two peaks located at 2θ = 22.75° and 46.48° are due to STO(001) and STO (002) reflections, respectively. (inset) In-plane scans of crystalline (upper) and quasi-amorphous (lower). The STO substrate is at 2θ = 32.38°. The low-angle structure in the crystalline film corresponds to fully relaxed BTO, there is a slight low-angle asymmetry in the scan of the quasi-amorphous film.

### A.3.3 XPD

In Figure A-4(a), we present the symmetrized Ti $2p_{3/2}$ XPD patterns of a crystalline BTO film. The XPD pattern of sample 2 is presented in Figure A-4(b). In contrast to the regular diffraction pattern of the crystalline sample, which reflects the high local order, the XPD pattern of sample 2 shows no angular anisotropy. The center of XPD pattern represents normal emission; the edge represents grazing angle emission. Thus there is no macroscopically coherent local order in either inplane or out-of-plane directions, which further reinforces the conclusion from XRD that sample 2 is amorphous.

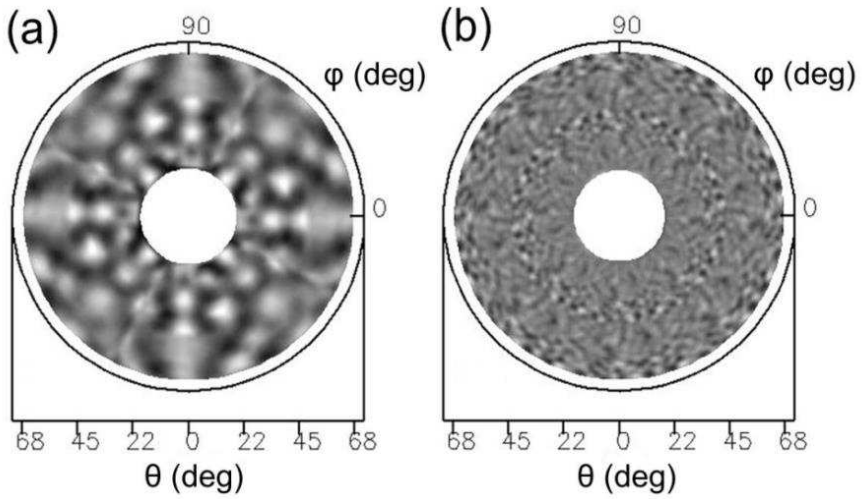


**Figure A-4.** Ti 2p XPD diffraction patterns from (a) crystalline BTO and (b) sample 2 (QA BTO).

### A.3.4 PFM

Figure A-5(a) shows the phase response of the PFM-written FE domains on the amorphous film. The contrast between bright and dark areas can be clearly observed. The outer square of $40 \times 40$ μm$^2$ was written by a positive bias of +6 V creating a negative image charge below the surface and thus a downward pointing polarization ($P^-$) and the inner area of $20 \times 20$ μm$^2$ square was reversed by a −6 V bias, creating an upward pointing polarization ($P^+$). The contrast originating from $P^+$ and $P^-$ polarizations was also observed 24 hours later [see Figure A-5(b)], excluding the possibility of significant charge injection during domain writing,

minimizing artefacts due to the electrostatic interaction between the lever and the sample and confirming the remanent FE polarization.

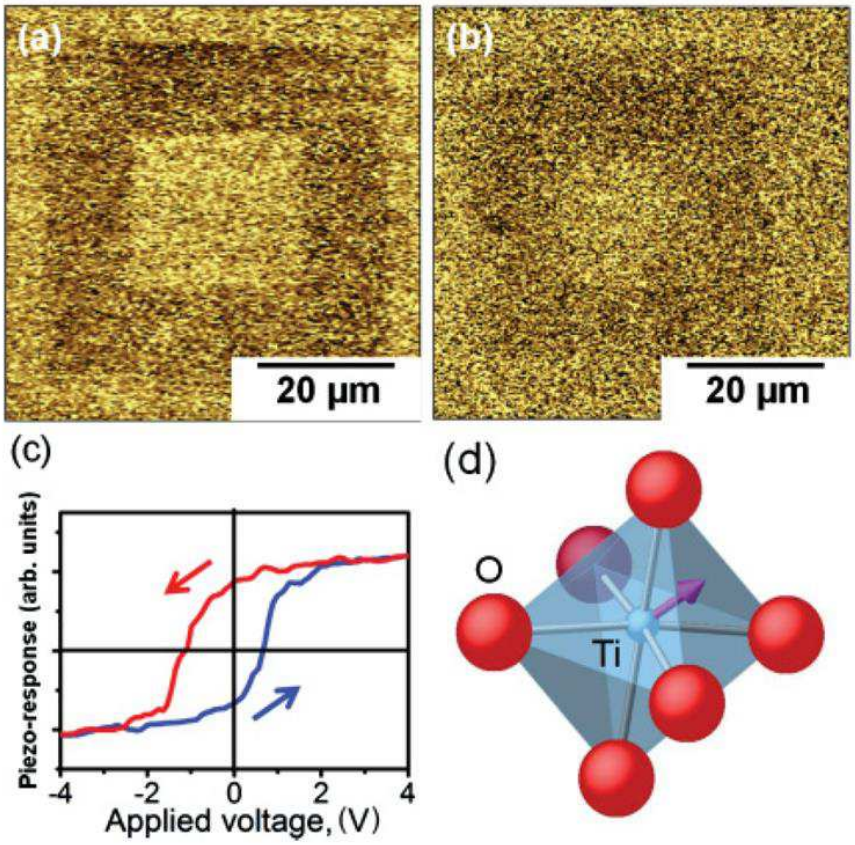


**Figure A-5.** PFM phase image of sample 2 (QA BTO film) showing contrast originating from $P^+$ and $P^-$ polarizations (a) immediately after writing and (b) 24 hours later. (c) Ferroelectric P-E hysteresis loop for the QA BTO film obtained 24 hours after writing. The direction around the loop is indicated by the arrows. (d) Schematic of the distorted $TiO_6$ octahedra in quasi-amorphous BTO. The off-center Ti displacement is along <111>, indicated by the arrow giving rise to shorter and longer Ti-O bonds.

Figure A-5(c) is the hysteresis of the piezoresponse obtained by ramping the applied voltage on the PFM tip obtained in the inner $P^+$ square of figure A-5(b), providing clear evidence of the ferroelectric nature of the film.[Fujisawa2005, Kolosov1995] If the piezo response were due to trapped charge, the hysteresis loop would be reversed. The exterior, unwritten sample area, also exhibits a net positive polarity, probably due to a FE imprint in the film. Ferroelectricity has already been observed in ultrathin crystalline BTO films though never in such a thin amorphous structure.[Sai2005, Garcia2009]

Figure A-5(d) shows a schematic of the off-center <111> Ti displacement from the literature following the order-disorder model of Ref.[Comès1970] and [Zhang2006]. X-ray fine structure (XAFS) experiments [Ravel1998] show that the Ti atoms are displaced along various of the eight possible <111> directions in all phases. First principles quantum mechanics (QM) calculations using the local density approximation to density functional theory (DFT) show that the Ti atoms displace along various <111> directions while retaining the macroscopic symmetries in different phases.[Zhang2006]

Since the volume detection limit of a crystalline phase by XRD is about 0.3 %,[Lyahovitskaya2003, Tanner1976] an order of magnitude smaller than the fraction of $TiO_6$ octahedra thought to contribute to the polarization in thicker QA samples[Frenkel2005] and since the XPD shows no macroscopically coherent local order, we can exclude the formation of nanocrystalline BTO in sample 2. The easy acquisition of a hysteresis loop by the PFM tip over all the sample surface with a high coercive field [estimated from $(|E_C| + |-E_C|)/2$ to be 2000 kV/cm, see below] also makes it highly unlikely that the ferroelectricity originates from small crystalline grains, because the coercive field in grain size around 5 nm is less than 500 kV/cm.[Jo2006] Thus the evidence points to the formation of a polar QA phase of BTO after annealing at 700 °C in $O_2$ flow. From the slight asymmetry or shoulder in the out of plane XRD curve, the calculated lattice constant for the low-angle structure is 4.100 Å , much larger than that of bulk BTO. We interpret it as the result of the alignment along c axis of first BTO unit cell with the STO substrate The Sr-3d intensities discussed below provide further support for this interpretation. The large voids or pinholes observed in AFM image of sample 1 probably result from relaxation of the BTO during post-deposition annealing, producing a fully relaxed, crystalline film. The transition from amorphous to crystalline state requires a considerable volume expansion prior to nucleation.[Wachtel2010] If the expansion is frustrated, then a QA phase results. Hence, sample 2 may form a QA phase due to the in-plane clamping by the STO substrate which would also explain the very small pinholes. We therefore will refer to samples 1 and 2 as the crystalline and the quasi-amorphous (QA) films, respectively.

### A.3.5 XPS

The C 1s, Ti 2p, Ba 3d, O 1s, and Sr 3d core-level XPS spectra are shown in Figures. 7-6(a)-(e). The intensity of the C 1s spectra in Figure A-6(a) shows that both thin film surfaces have a similar low carbon contamination. More importantly, the high-binding-energy component usually associated with carbonate-like bonding at the surface is 12 times weaker than the main C 1s peak. This indicates that the surface is indeed largely free of carbonate adsorbates that could affect the ferroelectricity. In careful studies of clean BTO surfaces, for example, Baniecki et al.,[Baniecki2006] the carbonate peak is typically ten times smaller than the main C 1s line.

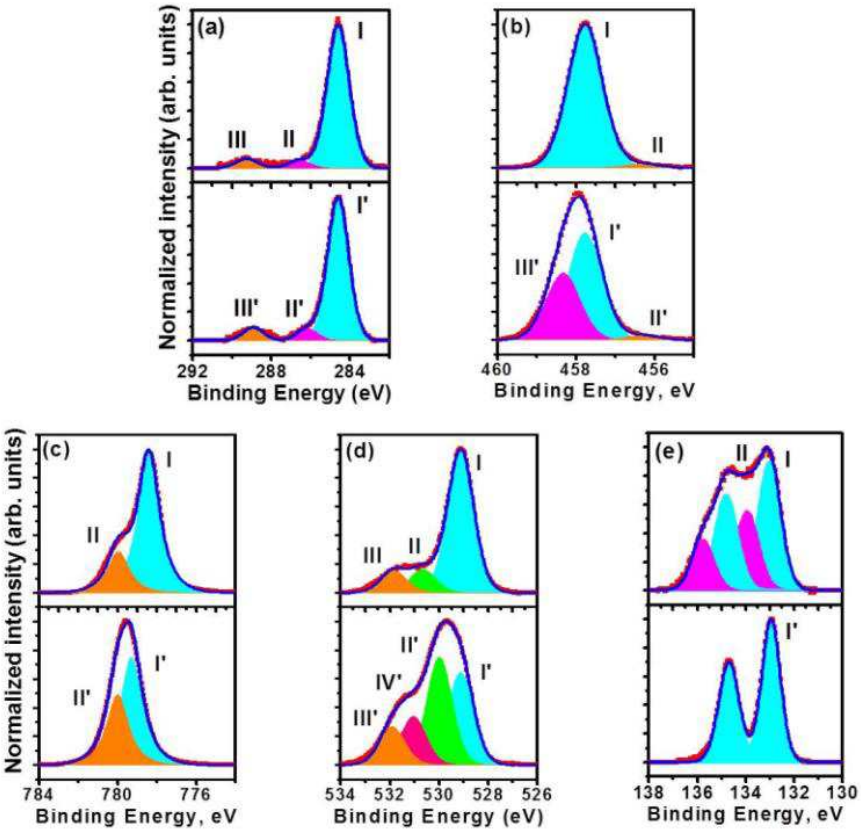


**Figure A-6.** Core-level spectra for crystalline (top) and QA (bottom) films: (a) C 1s, (b) Ti $2p_{3/2}$, (c) Ba $3d_{5/2}$, (d) O 1s, and (e) Sr 3d spectra from the STO substrate under the films.

The Ti $2p_{3/2}$ spectra are shown in figure A-6(b). The spectra are fitted with the same FWHM(1.0 eV) and Gaussian/Lorentzian (70/30) ratio for all peaks. Thanks to the high energy resolution, we see that the two spectra are not identical, unlike

previous work on much thicker films (50-200nm). Both crystalline and QA spectra have a main component due to Ti with a formal valency of 4+ in the $TiO_6$ octahedra, and a very weak, low-binding-energy (LBE) component corresponding to reduced Ti, often described as $Ti^{3+}$. The latter is known to occur as a result of the formation of oxygen vacancies, the presence of which is confirmed by the valence band spectra shown below (see Figure A-7). There is no observable shift in the main peak between crystalline and QA samples in agreement with Ref. [Ehre2008], demonstrating that the $TiO_6$ LBUs are largely unchanged in term of chemistry, consistent with EXAFS analysis of QA STO and BTO.[Frenkel2005, Frenkel2007] However, the intensity decreases significantly in the QA spectrum with the simultaneous appearance of a high-binding-energy (HBE) component shifted by 0.5 eV with respect to the main peak. The HBE component we observe in the QA spectrum is reminiscent of the HBE component observed in Ba 3d spectra of crystalline BTO films.[Baniecki2006, Barrett2010] This has been associated with a near surface space charge region giving rise to charge depletion[LiX2008] and is discussed below.

The XPS spectra of Ba $3d_{5/2}$ and O 1s are presented in figures 7-6(c) and 7-6(d). Both the shape and the position of the Ba $3d_{5/2}$ line change when going from crystalline to QA. In the former, the main peak, labeled I, has a binding energy of 778.4 eV, in the QA sample the peak shifts by 0.9 eV to higher BE. Each spectrum also has an HBE component labeled II, shifted by 1.6 and 0.7 eV for crystalline and QA BTO, respectively. Grazing emission angle XPS confirmed that this HBE component is of surface origin. The shift of the surface component in crystalline BTO is very similar to that observed on the clean surface of a thick BTO single-crystal film and characteristic of the FE state.[Baniecki2006] It should be recalled that there is no evidence for the presence of significant surface carbonate species therefore the HBE component cannot be attributed to $BaCO_3$ species.

The O 1s spectra also show important differences when going from crystalline to QA films. The spectrum of the crystalline film can be deconvoluted into three components, peak I due to oxygen in the perovskite environment, and peaks II and III, both of which are of surface origin. Peak II is shifted by 1.6 eV with respect to peak I, similar to the clean surface related shift in the Ba 3d, whereas peak III is at a binding energy of 531.9 eV and is ascribed to low residual surface contamination.

On the other hand, the QA spectrum requires four peaks to achieve a good fit. Components I and III are unshifted with respect to the crystalline film, unlike the main Ba 3d component in Figure A-6(c). Peak II, of surface origin, is shifted by 0.9 eV with respect to the main component instead of 1.6 eV in the case of the c film. The origin of the fourth peak is still under investigation. However, its presence suggests that there is not a simple symmetry based on static charge transfer between oxygen and cations in the QA amorphous phase, but rather a more complex change in atomic and electronic structure.

The Sr 3d spectra from the substrate of crystalline and QA films are presented in Figure A-6(e). The positions of the main Sr 3d peak of both samples, labeled I, are indistinguishable within the experimental accuracy. The spectrum of the crystalline film has an HBE component, labeled II, shifted by 0.9 eV. The appearance of surface component is also observed on clean STO surfaces.[Baniecki2006, Vanacore2010] In our case, there is no free STO surface, however, the finite XPS probing depth means that the Sr 3d spectra are particularly sensitive to the chemical environment at the BTO/STO interface. Thus the Sr at the interface with the QA film appears to be in a bulk-like environment, whereas the Sr at the interface with the fully relaxed crystalline BTO has a similar spectrum to that of a clean STO surface. This would indeed be consistent with the interpretation of the out-of-plane XRD scan of the QA sample being due to the epitaxy of the first BTO unit cell on the STO surface. The full relaxation of the crystalline BTO film, on the other hand, reduces sufficiently the chemical bonding at the interface so that the Sr-3d spectrum shows a more surface-like character. The Sr-3d intensity has been used to estimate the thickness of the crystalline and QA BTO films to be 3.2 and 3.8 nm, respectively. The mean-free path has been calculated using the National Institute of Standards and Technology (NIST) database,[Powell1999] and as a first approximation we have assumed BTO films with the bulk mass density. A more accurate calculation would have to take into account volume change, but the observed pinhole concentration makes this adjustment difficult.

The valence band spectra are reported in Figure A-7. They are very similar to crystalline and QA results obtained on much thicker films.[Ehre2008] All of the features reported in Ref. [Ehre2008] are visible in the spectra. The double-peak structure at 3.3 and 5.1 eV corresponds to O-2$\pi$ and $\sigma$ bonding orbits. The peaks

are less well resolved in the QA phase because of structural disorder.[Adachi1998, Hudson1993] There is also a broad peak between 8.6 and 11.2 eV in the QA spectrum, which is absent from the crystalline phase. Density functional theory (DFT) calculations have shown that there is a significant contribution to the density of states (mainly, O $p_z$ projected) in this region due to the additional O-O coordination in $BaO_2$ compared to BaO.[Königstein1999] The combination of apex, edge, and even face sharing $TiO_6$ octahedra in amorphous and QA phases would produce such Ba-mediated O-O coordination, as discussed in Ref. [Wachtel2010], although as yet only evidence for apex and edge sharing has been furnished.[Frenkel2007] Note also that the Ba-5p semicore levels are shifted by about 1 eV to higher binding energy just like the Ba 3d shown in Figure A-6(c). The density of states observed in the band-gap region just over 1 eV below the Fermi level corresponds to oxygen vacancy states, consistent with the small component due to reduced Ti observed in Figure A-6(b).

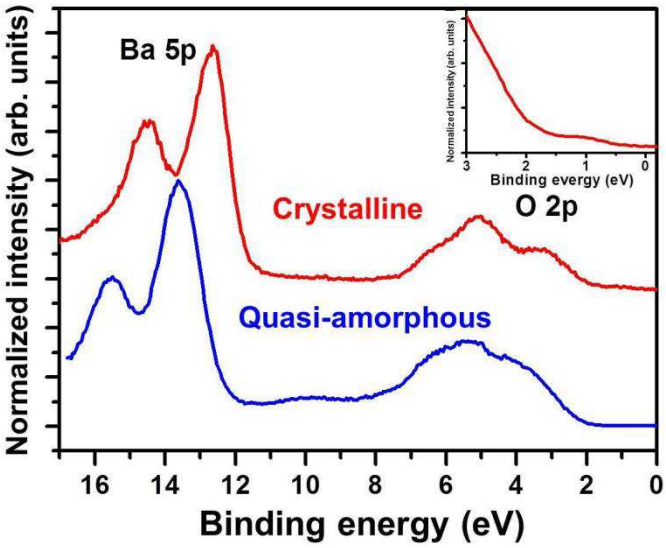


**Figure A-7.** Valence band spectra of the crystalline and QA BTO. (Inset) Fermi-level region of the crystalline BTO film.

## A.4 Discussion

In QA phase, the distorted $TiO_6$ LBUs can, in principle, be connected in three different ways: apex to apex, edge to edge, and face to face (Figure A-8), although as previously mentioned, the latter case has yet to be demonstrated. Ba ions are

located in the voids created between the distorted LBUs. The Ba ions in such bonds must have less than 12 O neighbors and should therefore have some excess negative charge compared with the perovskite BTO. Simultaneously, some of the $TiO_6$ corners must be unconnected and the oxygen at these apices has only one Ti neighbor, acquiring some excess positive charge.

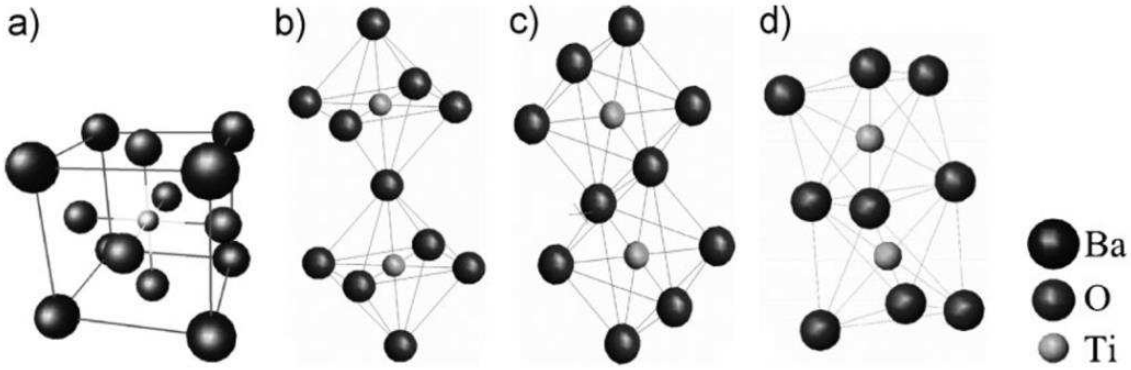


**Figure A-8.** (a) Unit cell of crystalline perovskite (cubic) $BaTiO_3$; (b) scheme of the $TiO_6$ octahedra connected apex–apex as in the crystalline phase; (c), (d) $TiO_6$ octahedra sharing edges and faces, respectively. (This figure is reproduced from [Wachtel2010])

A simple interpretation based on static charge transfer cannot explain all the observed behavior. For example, the Ba 3d peaks are shifted when going from the crystalline to QA film, whereas the O 1s show in addition, a new HBE component. Static charge transfer can give a first insight into, for example, the valence state of ions or the chemical bonding. However, one would expect reciprocity in at least the direction of the core-level shifts between an anion and a cation involved in charge transfer. Exact charge transfer is difficult to measure because it is always, to some extent, arbitrary, in particular, in correlated systems like ferroelectrics.

Dynamical charge is more relevant for deformed polar materials.[Ghosez1998] First principles calculations of the Born effective charge (i.e., in the absence of an external electric field) allow band-by-band analysis of the contributions to the anomalous dynamical charge as a function of the atomic distortion. Using this method, Ghosez et al.[Ghosez1998] have shown that the electronic current flows opposite to the displacement of positive ions enhancing the change in polarization. Contrary to a simple charge transfer model, the dynamical charge tensor is not just a function of the shortest or longest Ti-O bond, but rather of the anisotropy along the Ti-O chains. In this picture, the shorter Ti-O bonds will have enhanced

covalency, whereas the longer bonds will be more ionic. Thus the partially covalent character of Ti-O bonds in perovskite oxides[Vanacore2010, Wadati2009] will certainly be modified by the high off-center Ti position creating a strong anisotropy in the Ti-O bond length along the c axis of each octahedron.

This may explain why we also observe a surface-related peak at HBE in the QA Ti 2p spectrum just like in the Ba 3d spectrum. In the presence of higher ionicity, a stronger space-charge effect at the surface may be expected, giving rise to a similar shift in the Ti $2p_{3/2}$ peak. To our knowledge, such a component has not been previously observed in crystalline BTO and seems to be specific to the ultrathin QA layer. Both O 1s and Ba 3d surface-related peaks are less shifted with respect to the main peak in the QA film than in the crystalline film. We think that the lack of long-range order results in a less well defined microscopic boundary condition of the displacement field at the surface than for a crystalline film. The breaking of the long-range order by the quasi-amorphous structure renders an understanding of the local polarization induced by atomic distortion even more important.

The link between microscopic structure and macroscopic polarization in ferroelectrics has long been a matter of debate with both displacive[Cochran1960] and order-disorder eight-site [Comès1970] models proposed. Recent quantum mechanical calculations using density functional theory,[Zhang2006] based on original insights into the interaction between long wavelength soft phonon modes and local atomic distortion, [Girschberg1997] integrate antiferroelectricity into the ferroelectric phases of BTO to satisfactorily explain XAS,[Ravel1998] Raman,[Vogt1982] and IR[Luspin1980] experiments. Thus the off-center Ti displacement is now thought to be along <111> with local order between adjacent chains of $TiO_6$ octahedra. However, in our case, there is no long-range order, therefore the observed polarization can only be due to a preferential alignment of the local distortion in the $TiO_6$ octahedra.

Some useful insights may be obtained by comparing the coercive field measured here with that measured or calculated for crystalline thin films. In strained crystalline thin films, using the free energy density functional of homogeneous switching in the out-of-plane polarization state ($P_1 = P_2 = 0$, $P \neq 0$) within a nonlinear thermodynamic theory, the coercive field is calculated to be 1600

kV/cm.[Pertsev1998] The coercive field, $E_C$, obtained from ferroelectric hysteresis loop measured on the QA BTO film is 2000 kV/cm in a parallel plate capacitor geometry. This is about eight times larger than that observed of BTO on $SrRuO_3$ (SRO) (Figure A-9),[Jo2006] which has a similar compressive strain (2.2 %). Jo et al. showed that when the domain nucleation shape changes from half prolate spheroidal to cylindrical in thin films, the calculated coercive field is reduced from 700 to 250 kV/cm for a thickness of 4 nm,[Jo2006] in agreement with their experiment. The lack of long-range order in the quasi-amorphous film makes the presence of such cylindrical domains energetically unfavorable, thus a higher coercive field is probable, possibly pointing to spheroidal domain nucleation as the switching mechanism. This is further circumstantial evidence that the macroscopic polarization observed in the quasi-amorphous structure does not include a long-range displacive contribution and is, in fact, due to the sum of local, distortion-induced polarizations.

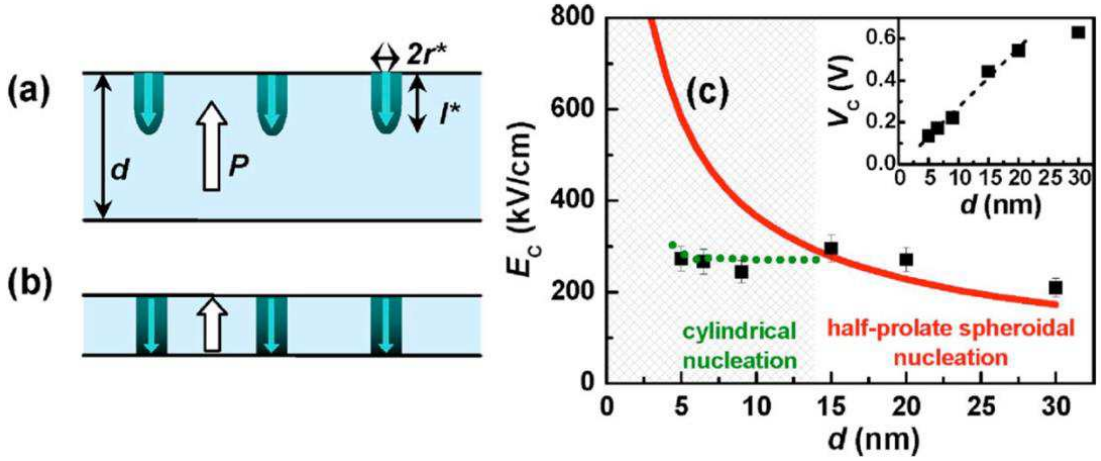


**Figure A-9.** Schematic diagrams of (a) half-prolate spheroidal nucleation and (b) cylindrical nucleation. (c) The d-dependent (solid squares) experimental and calculated $E_C$ based on the half-prolate spheroidal nucleation model (red solid line) and the cylindrical nucleation model (green dotted line). In the shaded region, the d-dependent $E_C$ is thought to be governed by cylindrical nucleation, rather than half-prolate spheroidal nucleation. The inset shows the coercive voltages ($V_C$) as a function of d. (This figure is reproduced from [Wachtel2010])

As previously noted, BTO must undergo a volume expansion of about 10 % prior to the onset of nucleation and crystallization.[Wachtel2010] Due to in-plane clamping, volume expansion is frustrated. The Ti ions shifted 0.44 Å off center in the $TiO_6$ octahedra along the c axis, almost twice as big as in the room-temperature

crystalline FE phase (0.23 Å),[Frenkel2005] changing the anomalous dynamical charge and hence the local polarization. The presence of a local atomic distortion is not, in itself, a sufficient condition for macroscopic polarization that requires a preferential orientation of the LBUs imposed by the in-plane clamping. Our measured coercive field would represent 4−5 % of aligned LBUs in a single-crystal film. For a macroscopic polarization equal to the sum of the local polarizations, the figure is most probably significantly higher. However, it is clear that a detailed understanding of how local polarization can give rise to ferroelectricity in an amorphous structure is far from complete. The exact stoichiometry, for example, may also play an important role.

Compared with the method previously used,[Lyahovitskaya2003, Ehre2007] the one presented here is more suitable for preparation of QA ultrathin BTO films. To form a crystalline phase, an amorphous film must first undergo volume expansion upon heating, turning into an intermediate low-density phase before crystallization. If the film is clamped by a substrate, then in-plane volume expansion is blocked, nucleation may be suppressed resulting in the QA phase.[Ebralidze2005] The lattice mismatch between the STO substrate and BTO is smaller than for Si or $SiO_2$, used by Ehre et. al.,[Lyahovitskaya2005, EhreD2007, Ehre2008, Frenkel2005, Frenkel2007, Wachtel2010] possibly reducing the dislocation density in the film, which could otherwise provide nucleation sites. The key factor in the production of such a QA film seems to be the appropriate growth rate followed by clamping control during annealing in oxygen. We think that this is the reason why we can anneal the whole STO substrate-supported film directly rather than using a pull through a narrow hot zone.

## A.5 Conclusion

We have identified the ferroelectric phase in a quasi-amorphous ultrathin BTO film grown on STO(001) substrate at room temperature by MBE. In-plane clamping prevents nucleation of the as-deposited amorphous BTO during annealing in $O_2$ flow and results in the formation of a QA phase. The QA nature is confirmed by in- and out-of-plane XRD, XPD, and XPS. Significant changes in the electronic structure are observed compared with an ultrathin crystalline film. In the QA phase, Ba ions occupy voids between distorted octahedral LBUs changing the observed core-level binding energies. A new component is observed in the Ti $2p_{3/2}$ corelevel

spectrum, which we qualitatively interpret on the basis of dynamical charge arguments. The valence band spectra are identical to those previously observed in much thicker films. FE polarized domains with good retention have been successfully written into the QA film and the FE nature is proven by a clear P-E hysteresis curve. In the literature, the QA phase was generated from the strain induced by pulling through a high temperature gradient, whereas here the strain state is governed by surface clamping. These results demonstrate the preparation of a QA FE BTO thin film grown on STO substrate by uniform post-deposition annealing.

To further explore the formation mechanism of quasi-amorphous BTO, a series of amorphous BTO with different thicknesses need to be grown and annealed under same condition. Meanwhile, the BTO films with different Ba/Ti ratios can be used to study the stoichiometric influence of quasi-amorphous BTO. Finally, different materials, such as $PbTiO_3$ and $Pb(Zr,Ti)O_3$, will be fabricated for a more systematic understanding of quasi-amorphous phase.

# Bibliography

[Adachi1998] Y. Adachi, S. Kohiki, K. Wagatsuma, and M. Oku, J. Appl. Phys. 84, 2123 (1998).

[Ahn2004] C. H. Ahn, K. M. Rabe, and J.-M. Triscone, Science 303, 488 (2004).

[Al-Mazroai2007] L. S. Al-Mazroai, M. Bowker, P. Davies, A. Dickinson, J. Greaves, D. James, and L. Millard, Catalysis Today 122, 46 (2007).

[Alexe2012] M. Alexe, Nano Lett. 12, 2193 (2012).

[Altman2010] M. S. Altman, J. Phys.: Condens. Matter 22, 084017 (2010).

[Atuchina2005] V.V. Atuchina, I.E. Kalabin, V.G. Kesler, and N.V. Pervukhina, J.

Elect. Spect. Rel. Phenom. 142, 129 (2005).

[Baniecki2006] J. D. Baniecki, M. Ishii, T. Shioga, K. Kurihara, and S. Miyahara, Appl. Phys. Lett. 89, 162908 (2006).

[Barbieri] A. Barbieri and M. A. Van Hove, SATLEED Package. http://www.ap.cityu.edu.hk/personal-website/Van-Hove_files/leed/leedpack.html (accessed March 2012).

[Barrett2010] N. Barrett, J. Rault, I. Krug, B. Vilquin, G. Niu, B. Gautier, D. Albertini, P. Lecoeur, and O. Renault, Surf. Interface Anal. 42, 1690 (2010).

[Barrett2013] N. Barrett, J. E. Rault, J. L. Wang, C. Mathieu, A. Locatelli, T. O. Mentes, M. A. Niño, S. Fusil, M. Bibes, A. Barthélémy, D. Sando, W. Ren, S. Prosandeev, L. Bellaiche, B. Vilquin, A. Petraru, I. P. Krug, and C. M. Schneider, J. Appl. Phys. 113, 187217 (2013).

[Belous2007] A. Belous, O. V'yunov, D. Mishchuk, S. Kamba, and D. Nuzhnyy, J. Appl. Phys. 102, 014111 (2007).

[Berlich2011] A. Berlich, H. Strauss, C. Langheinrich, A. Chasse, and H. Morgner, Surf. Sci. 605, 158 (2011).

[Binnig1986] G. Binnig, C. F. Quate, and Ch. Gerber, Phys. Rev. Lett. 56, 930 (1986).

[Bondino2002] F. Bondino, G. Comelli, A. Baraldi, R. Rosei, S. Lizzit, A. Goldoni, R. Larciprete, and G. Paolucci, Phys. Rev. B 66, 075402 (2002).

[Bonzel1993] H. P. Bonzel, Prog. Surf. Sci. 42, 219 (1993).

[Borg2002] M. Borg, A. Mikkelsen, M. Birgersson, M. Smedh, E. Lundgren, D. L. Adams, C. Almbladh, and J. N. Andersen, Surf. Sci.515, 267 (2002).

[Briggs1996] D. Briggs, and M. P. Seah, Practical Surface Analysis (Second Edition), Volume 1: Auger and X-ray Photoelectron Spectroscopy, John Wiley & Sons, (1996).

[Briggs2003] D. Briggs, Surface Analysis by Auger and X-ray Photoelectron Spectroscopy, edited by D. Briggs and J. T. Grant IM Publication, (2003).

[Brown1998] D. E. Brown, Science 279, 542 (1998).

[Brugere2011] A. Brugere, S. Gidon, and B. Gautier, J. Appl. Phys. 110, 052016 (2011).

[Brundle1975] C.R. Brundle, Surf. Sci. 48, 99 (1975).

[Cai2005] M. -Q. Cai, Y. -J. Zhang, Z. Yin, and M. -S. Zhang, Phys. Rev. B 72, 075406 (2005).

[Carter1962] G. Carter, Vacuum, 12, 245 (1962).

[CasaXPS] N. Fairley, CasaXPS, 2009. http://www.casaxps.com/ (accessed March 2012).

[Chen1998] Y. Chen and M. V. Hove, MSCD Package, Lawrence Berkeley National Laboratory, 1998, http://www.ap.cityu.edu.hk/personal-website/Van-Hove_files/mscd/mscdpack.html.

[ChenY1998] Y. Chen, F. García de Abajo, A. Chassé, R. Ynzunza, A. Kaduwela, M. Van Hove, and C. Fadley, Phys. Rev. B 58, 13121 (1998).

[Chen2009] D. Chen, and J. H. Ye, Chem. Mater. 21, 2327 (2009).

[Cherifi2010] S. Cherifi, R. Hertel, S. Fusil, H. Béa, K. Bouzehouane, J. Allibe, M. Bibes, and A. Barthélémy, Phys. Status Solidi (RRL) 4, 22 (2010).

[Chernaya2000] T. S. Chernaya, B. A. Maksimov, T. R. Volk, L. I. Ivleva, and V. I. Simonov, Phys. Solid State 42, 1716 (2000).

[Cho1971] A.Y. Cho, J. Vac. Sci. Tech. 8, S31, (1971).

[Cho1975] A. Y. Cho, and J. R. Arthur, Prog. Solid State Chem. 10, 157, (1975).

[Choi1999] G. J. Choi, H. S. Kim and Y. S. Cho, Mater. Lett. 41, 122 (1999).

[Cochran1960] W. Cochran, Adv. Phys. 9, 387 (1960).

[Comès1970] R. Comès, M. Lambert, and A. Guinier, Acta Crystallogr. Sect. A 26, 244 (1970).

[Corcoran2010] C.J. Corcoran, H. Tavassol, M.A. Rigsby, P.S. Bagus, and A. Wieckowski, Journal of Power Sources 195, 7856 (2010).

[Cuniot-Ponsard2003] M. Cuniot-Ponsard, J. M. Desvignes, B. Ea-Kim and E. Leroy, J. Appl. Phys. 93, 1718 (2003).

[Cuniot-Ponsard2011] M. Cuniot-Ponsard, J. M. Desvignes, A. Bellemain, and F. Bridou, J. Appl. Phys. 109, 014107 (2011).

[Cunningham2005] W. P. Cunningham, and M. A. Cunningham, McGraw-Hill Science/Engineering/Math 3rd edition (2005).

[Ding2004] X. M. Ding, X. J. Yang, and X. Wang, Surface Physics and Surface Analysis, Fudan University Press, Shanghai, (2004).

[Despont2006] L. Despont, C. Koitzsch, F. Clerc, M. Garnier, P. Aebi, C. Lichtensteiger, J. -M. Triscone, F. Garcia de Abajo, E. Bousquet, and P. Ghosez, Phys. Rev. B 73, 094110 (2006).

[Dörfler1999] U.B. Dörfler, R. Piechatzek, T. Woike, M.K. Imlau, V. Wirth, L. Bohatý, T. Volk, R. Pankrath, and M. Wöhlecke, Appl. Phys. B: Lasers Opt. 68, 843 (1999).

[Du2012] Y. Du, N. G. Petrik, N. A. Deskins, Z. Wang, M. A. Henderson, G. A. Kimmel, and I. Lyubinetsky, Phys. Chem. Chem. Phys., 14 3066 (2012).

[Ebralidze2005] I. Ebralidze, V. Lyahovitskaya, I. Zon, E. Wachtel, and I. Lubomirsky, J. Mater. Chem. 15, 4258 (2005).

[Ehre2007] D. Ehre, V. Lyahovitskaya, A. Tagantsev, and I. Lubomirsky, Adv. Mater. 19, 1515 (2007).

[EhreD2007] D. Ehre, H. Cohen, V. Lyahovitskaya, A. Tagantsev, and I. Lubomirsky, Adv. Funct. Mater. 17, 1204 (2007).

[Ehre2008] D. Ehre, H. Cohen, V. Lyahovitskaya, and I. Lubomirsky, Phys. Rev. B 77, 184106 (2008).

[Ehrlich1963] G. Ehrlich, Adv. Catal., 14, 255 (1963).

[Einstein1905] A. Einstein, Annalen der Physik, 17, 132 (1905).

[Elder1947] F. R. Elder, A. M. Gurewitsch, R. V. Langmuir, and H. C. Pollock, Phys. Rev. 71, 829 (1947).

[Eng1999] L. M. Eng, H. -J. Güntherodt, G. A. Schneider, U. Köpke, and J. Muñoz Saldaña, App. Phys. Lett. 74, 233 (1999).

[Esswein2007] A. J. Esswein, and D. G. Nocera, Chem. Rev. 107, 4022 (2007).

[Evarestov2007] R. A. Evarestov, A. V. Bandura, and V. E. Alexandrov, Surf. Sci. 601, 1844 (2007).

[Ewbank1987] M.D. Ewbank, R.R. Neurgaonkar, W.K. Cory, and J. Feinberg, J. Appl. Phys. 62, 374 (1987).

[Fadley1984] C.S. Fadley, Prog. Surf. Sci. 16, 275 (1984).

[Fadley1993] C. S. Fadley, Surf. Sci. Rep. 19, 231 (1993).

[Fadley1994] C. S. Fadley, S. Thevuthasan, A. P. Kaduwela, C. Westphal, Y. J. Kim, R. Ynzunza, P. Len, E. Tober, F. Zhang, Z. Wang, S. Ruebush, A. Budge, and M. A. Van Hove, J. Electron Spectrosc. Relat. Phenom. 68, 19 (1994).

[Fadley1995] C. S. Fadley, M. A. Van Hove, Z. Hussain, and A. P. Kaduwela, J. Electron Spectrosc. Relat. Phenom. 75, 273 (1995).

[Fechner2008] M. Fechner, S. Ostanin and I. Mertig, Phys. Rev. B, 77 094112 (2008).

[Finocchi2000] F. Finocchi, and C. Noguera, Acid-Base Interactions: Relevance to Adhesion Science and Technology, edited by K. L. Mittal, VSP International Science Publishers (2000).

[Fong2006] D. D. Fong, A. M. Kolpak, J. A. Eastman, S. K. Streiffer, P. H. Fuoss, G. B. Stephenson, Carol Thompson, D. M. Kim, K. J. Choi, C. B. Eom, I. Grinberg, and A. M. Rappe, Phys. Rev. Lett. 96, 127601 (2006).

[Forsbergh1949] P. Forsbergh Jr., Phys. Rev. 76, 1187 (1949).

[Frenkel2005] A. I. Frenkel, Y. Feldman, V. Lyahovitskaya, E. Wachtel, and I. Lubomirsky, Phys. Rev. B 71, 024116 (2005).

[Frenkel2007] A. I. Frenkel, D. Ehre, V. Lyahovitskaya, L. Kanner, E. Wachtel, and I. Lubomirsky, Phys. Rev. Lett. 99, 215502 (2007).

[Fuenzalida1999] V.M. Fuenzalida, M.E. Pilleux, and I. Eisele, Vacuum, 55, 81 (1999).

[Fujisawa2005] H. Fujisawa, M. Shimizu, H. Niu, H. Nonomura, and K. Honda, Appl. Phys. Lett. 86, 012903 (2005).

[Fujishima1972] A. Fujishima, and K. Honda, Nature 238, 37 (1972).

[Garcia2009] V. Garcia, S. Fusil, K. Bouzehouane, S. Enouz-Vedrenne, N. D. Mathur, A. Barthélémy, and M. Bibes, Nature (London) 460, 81 (2009).

[Garra2009] J. Garra, J. M. Vohs, and D. A. Bonnell, Surf. Sci. 603, 1106 (2009).

[Geneste2009] G. Geneste, and B. Dkhil, Phys. Rev. B 79, 235420 (2009).

[Ghosez1998] Ph. Ghosez, J.-P.Michenaud, and X. Gonze, Phys. Rev. B 58, 6224 (1998).

[Giocondi2001] J. L. Giocondi, and G. S. Rohrer, J. Phys. Chem. B 105, 8275 (2001).

[Girschberg1997] Y. Girschberg, and Y. Yacoby, Solid State Commun. 103, 425 (1997).

[Gnecco2001] E. Gnecco, R. Bennewitz, T. Gyalog, and E. Meyer, J. Phys.: Condens. Matter 13, R619 (2001).

[Goniakowski2008] J. Goniakowski, F. Finocchi, and C. Noguera, Rep. Prog. Phys. 71, 016501 (2008).

[Gruverman2001] A. Gruverman, B. J. Rodriguez, R. J. Nemanich, and A. I. Kingon, J. Appl. Phys. 92, 2734 (2002).

[Habenschaden1984] E. Habenschaden, and J. Küppers, Surf. Sci. 138, L147 (1984).

[Harada1970] J. Harada, T. Pedersen, and Z. Barnea, Acta Crystallogr., Sect. A: Cryst. Phys., Diffr., Theor. Gen. Crystallogr. 26, 336 (1970).

[Henderson2002] M. A. Henderson, Surf. Sci. Rep. 46, 1 (2002).

[Henderson2011] M. A. Henderson, Surf. Sci. Rep. 66, 185 (2011).

[Hirata1994] A. Hirata, A. Ando, K. Saiki, and A. Koma, Surf. Sci. 310, 89 (1994).

[Hodgson2009]A. Hodgson, and S. Haq, Surf. Sci. Rep. 64, 381 (2009).

[Hofmann2007] A. Hofmann, The Physics of Synchrotron Radiation, Cambridge University Press (2007).

[Horowitz1993] M. Horowitz, A. Bekker, and B. Fischer, Appl. Phys. Lett. 62, 2619 (1993).

[Hudson1993] L. T. Hudson, R. L. Kurtz, S. W. Robey, D. Temple, and R. L. Stockbauer, Phys. Rev. B 47, 1174 (1993).

[Hüfner2003] S. Hüfner, Photoelectron Spectroscopy: Principles and Applications, Springer (2003).

[Hüfner2005] S. Hüfner, S. Schmidt, and F. Reinert, Nucl. Instrum. Methods Phys. Res. A 547, 8 (2005).

[Iwazaki2012] Y. Iwazaki, T. Suzuki, Y. Mizuno, and S. Tsuneyuki, Phys. Rev. B 86, 214103 (2012).

[Jamieson1968] P.B. Jamieson, S. C. Abrahams, and J. L. Bernstein, J. Chem. Phys. 48, 5048 (1968).

[Jaworowski2002] A. J. Jaworowski, R. Asmundsson, P. Uvdal, and A. Sandell, Surf. Sci. 501, 74 (2002).

[Jia2004] C. L. Jia, and K. Urban, Science 303, 2001 (2004).

[Jo2006] J. Y. Jo, Y. S. Kim, T. W. Noh, J.-G. Yoon, and T. K. Song, Appl. Phys. Lett. 89, 232909 (2006).

[Joly2000] J. P. Joly, F. Gaillard, E. Peillex, and M. Romand, Vacuum 59, 854 (2000).

[Juarez-Reyes2001] A. Juarez-Reyes, Some basic principles of synchrotron radiation, AMLM group, (2001).

[Jung2011] J. Jung, and D. D. Edwards, J. Solid State Chem.184, 2238 (2011).

[Kalinin2001] S. V. Kalinin, and D. A. Bonnell, Phys. Rev. B 63, 125411 (2001).

[Kalinin2002] S. V. Kalinin, and D. A. Bonnell, Phys. Rev. B 65, 125408 (2002).

[Kalinin2004] S. V. Kalinin, E. Karapetian, and M. Kachanov, Phys. Rev. B 70, 184101 (2004).

[Kalinin2006] S. V. Kalinin, B. J. Rodriguez, S. Jesse, S. Shin, A. P. Baddorf, P. Gupta, H. Jain, D. B. Williams, and A. Gruverman, Microscopy and Microanalysis 12, 206 (2006).

[Kawasaki1994] M. Kawasaki, K. Takahashi, T. Maeda, R. Tsuchiya, M. Shinohara, O. Ishiyama, T. Yonezawa, M. Yoshimoto, and H. Koinuma, Science 266, 1540 (1994).

[Kevan1980] S. D. Kevan, Phys. Rev. B 28, 2268 (1983).

[Kim1999] H. G. Kim, D. W. Hwang, J. Kim, Y. G. Kim, and J. S. Lee, Chem. Comm. 1077 (1999).

[Kim2002] M. -S. Kim, P. Wang, J. -H. Lee, J. -J. Kim, H. Y. Lee, and S. -H. Cho, Jpn. J. Appl. Phys. 41, 7042(2002).

[Kim2004] H. G. Kim, D. W. Hwang, and J. S. Lee, J. Am. Chem. Soc. 126 8912 (2004).

[Kim2005] D. J. Kim, J. Y. Jo, Y. S. Kim, Y. J. Chang, J. S. Lee, J.-G. Yoon, T. K. Song, and T.W. Noh, Phys. Rev. Lett. 95, 237602 (2005).

[Klein2001] J. Klein, Epitaktische Heterostrukturen aus dotierten Manganaten, PhD Thesis, University of Cologne (2001).

[Kobayashi2012] Y. Kobayashi, O. J. Hernandez, T. Sakaguchi, T. Yajima, T. Roisnel, Y. Tsujimoto, Ma. Morita, Y. Noda, Y. Mogami, A. Kitada, M. Ohkura, S. Hosokawa, Z. Li, K. Hayashi, Y. Kusano, J. E. Kim, N. Tsuji, A. Fujiwara, Y.

Matsushita, K. Yoshimura, K. Takegoshi, M. Inoue, M. Takano, and H. Kageyama, Nat. Mater. 11, 507 (2012).

[Kohno1997] M. Kohno, S. Ogura, K. Sato, and Y. Inoue, J. Chem. Soc., Faraday Trans., 93, 2433 (1997).

[Kolosov1995] O. Kolosov, A. Gruverman, J. Hatano, K. Takahashi, and H. Tokumoto, Phys. Rev. Lett. 74, 4309 (1995).

[Kolpak2008] A. M. Kolpak, D. Li, R. Shao, A. Rappe, and D. Bonnell, Phys. Rev. Lett. 101, 036102 (2008).

[Königstein1999] M. Königstein, A. A. Sokol, and C. R. A. Catlow, Phys. Rev. B 60, 4594 (1999).

[Krug2010]I. Krug, N. Barrett, A. Petraru, A. Locatelli, T. O. Mentes, M. A. Niño, K. Rahmanizadeh, G. Bihlmayer, and C. M. Schneider, Appl. Phys. Lett. 97, 222903 (2010).

[Kudo2000] A. Kudo, H. Kato, and S. Nakagawa, J. Phys. Chem. B 104, 571 (2000).

[Kudo2009] A. Kudo, and Y. Miseki, Chem. Soc. Rev. 38, 253 (2009).

[Kuwabara1997] M. Kuwabara, H. Matsuda, N. Kurata, and E. Matsuyama, J. Am. Ceram. Soc. 80, 2590 (1997).

[Kwei1993] G. H. Kwei, A. C. Lawson, S. J. L. Billinge, and S.-W. Cbeong, J. Phys. Chem. 97, 2368 (1993).

[Lenzo1967] P. V. Lenzo, E. G. Spencer, and A. A. Ballman, Appl. Phys. Lett. 11,

23 (1967).

[Li2005] X. L. Li, B. Chen, H. Y. Jing, H. B. Lu, B. R. Zhao, Z. H. Mai, and Q. J.

Jia, Appl. Phys. Lett. 87, 222905 (2005).

[Li2008] D. Li, M. H. Zhao, J. Garra, A. M. Kolpak, A. M. Rappe, D. A. Bonnell, and J. M. Vohs, Nat. Mater. 7, 473 (2008).

[Lines1977] M. E. Lines, and A. M. Glass, Principles and applications of ferroelectrics and related materials, Oxford University Press (1977).

[LiX2008] X. L. Li, H. B. Lu, Ming Li, Z. H. Mai, H. J. Kim, and Q. J. Jia, Appl. Phys. Lett. 92, 012902 (2008).

[Lohokare1998] S. P. Lohokare, E. L. Crane, L. H. Dubois, and R. G. Nuzzo, J. Chem. Phys. 108, 8640 (1998).

[Luspin1980] Y. Luspin, J. L. Servoin, and F. Gervais, J. Phys. C 13, 3761 (1980).

[Lyahovitskaya2003] V. Lyahovitskaya, I. Zon, Y. Feldman, S. R. Cohen, A. K. Tagantsev, and I. Lubomirsky, Adv. Mater. 15, 1826 (2003).

[Lyahovitskaya2005] V. Lyahovitskaya, Y. Feldman, I. Zon, E. Wachtel, K. Gartsman, A. K. Tagantsev, and I. Lubomirsky, Phys. Rev. B 71, 94205 (2005)

[Merz1954] W. J. Merz, Phys. Rev. 95, 690 (1954).

[Meyer2001] B. Meyer, and D. Vanderbilt, Phys. Rev. B 63, 205426 (2001).

[Mi2012] Y. Mi, G. Geneste, J. E. Rault, C. Mathieu, A. Pancotti, and N. Barrett, J. Phys.: Condens. Matter 24, 275901 (2012).

[Mitchell2000] R. H. Mitchell, A. R. Chakhmouradian, and P. M. Woodward, Phys. Chem. Miner. 27, 583 (2000).

[Mitsui1981] T. Mitsui, E. Nakamura, and K. Gesi, Landolt-Börnstein: Numerical Data and Functional Relationships in Science and Technology, edited by K.-H. Hellwege, and A. Hellwege, Springer-Verlag, Berlin, (1981).

[Miura2002] K. Miura, Appl. Phys. Lett. 80, 2967 (2002).

[Morita1996] S. Morita, S. Fujisawab, and Y. Sugawara, Surf. Sci. Rep. 23, 1 (1996).

[Morrison1980] S. R. Morrison, Electrochemistry at semiconductor and oxidized metal electrodes, Plenum Press: New York, (1980).

[Nascimento2007] V. Nascimento, R. Moore, J. Rundgren, J. Zhang, L. Cai, R. Jin, D. Mandrus, and E. Plummer, Phys. Rev. B 75, 035408 (2007).

[Navarro2007] R. M. Navarro, M. A. Peña, and J. L. G. Fierro, Chem. Rev.107, 3952 (2007).

[Ni2007] M. Ni, M. K. H. Leung, D. Y. C. Leung, and K. Sumathy, Renewable and Sustainable Energy Reviews 11, 401 (2007).

[NIST] NIST Electron Inelastic-Mean-Free-Path Database, version 1.2; C. J. Powell, A. Jablonski, Eds.; National Institute of Standards and Technology: Gaithersburg, MD, (2010).

[Niu2010] G. Niu, PhD thesis, Ecole centrale de Lyon, (2010)

[Niu2011] G. Niu, S. Yin, G. Saint-Girons, B. Gautier, P. Lecoeur, V. Pillard, G. Hollinger, and B. Vilquin, Microelectronic Engineering 88, 1232 (2011).

[Niu2012] G. Niu, B. Gautier, S. Yin, G. Saint-Girons, P. Lecoeur, V. Pillard, G. Hollinger, and B. Vilquin, Thin Solid Films 520, 4595 (2012).

[Noguera2000] C. Noguera, J. Phys.: Condens. Matter 12, R367 (2000).

[Noguera2004] C. Noguera, F. Finocchi, and J. Goniakowski, J. Phys.: Condens. Matter 16, S2509 (2004).

[Nordling1957] C. Nordling, E. Sokolowski, and K. Siegbahn, Phys. Rev. 105, 1676 (1957).

[Nyholm1991] R. Nyholm, J. N. Andersen, J. F. van Acker, and M. Qvarford, Phys. Rev. B 44, 10987 (1991).

[Omicron] http://www.omicron.de

[Osterloh2008] F. E. Osterloh, Chemistry of Materials 20, 35 (2008).

[Osterwalder1991] J. Osterwalder, T. Greber, A. Stuck, and L. Schlapbach, Phys. Rev. B 44, 13764 (1991).

[Osterwalder1995] J. Osterwalder, P. Aebi, R. Fasel, D. Naumovic, P. Schwaller, T. Treutz, L. Schlapbach, T. Abukawa, and S. Kono, Surf. Sci. 331, 1002 (1995).

[Padilla1997] J. Padilla, and D. Vanderbilt, Phys. Rev. B 56, 1625 (1997).

[Palo2007] D. Palo, R. Dagle, and J. Holladay, Chem. Rev. 107, 3992 (2007).

[Pancotti2009] A. Pancotti, N. Barrett, L. F. Zagonel, and G.M. Vanacore, J. Appl. Phys. 106, 034104 (2009).

[PancottiA2009] A. Pancotti, PhD thesis, Universidade Estadual de Campinas, (2009).

[Pancotti2013] A. Pancotti, J. L. Wang, P. Chen, L. Tortech, C. -M. Teodorescu, E. Frantzeskakis, and N. Barrett, Phys. Rev. B 87, 184116 (2013).

[Papageorgiou2010] A. C. Papageorgiou, N. S. Beglitis, C. L. Pang, G. Teobaldi, G. Cabailh, Q. Chen, A. J. Fisher, W. A. Hofer, and G. Thornton, Proc. Natl. Acad. Sci. U.S.A. 107, 2391 (2010).

[Park2000] C. H. Park, and D. J. Chadi, Phys. Rev. Lett. 84, 4717 (2000).

[Peillex1995] E. Peillex, F. Gaillard, M. Romand, J. P. Joly, and D. Verchere, J. Adhesion, 50, 59 (1995).

[Pendry1980] J. B. Pendry, J. Phys. C 13, 937 (1980).

[Pertsev1998] N. A. Pertsev, A. G. Zembilgotov, and A. K. Tagantsev, Phys. Rev. Lett. 80, 1988 (1998).

[Pertsev2007] N. Pertsev, and H. Kohlstedt, Phys. Rev. Lett. 98, 257603 (2007).

[Pintilie2001] L. Pintilie, I. Pintilie, Mater. Sci. Eng. B 80, 388 (2001).

[Podlozhenov2006] S. Podlozhenov, H. A. Graetsch, J. Schneider, M Ulex, M.

Wohlecke, and K. Betzler, Acta Cryst. B 62, 960 (2006).

[Powell1999] C. J. Powell, and A. Jablonski, J. Phys. Chem. Ref. Data 28, 19 (1999).

[Powell2009] C. J. Powell, and A. Jablonski, Nucl. Instrum.Methods Phys. Res., Sect. A 601, 54 (2009).

[Proksch] R. Proksch, and S. Kalinin, Piezoresponse Force Microscopy with Asylum Research AFMs, Asylum Research.

[Qu2002] Y. -Q. Qu, A. -D. Li, Q. -Y. Shao, Y. -F. Tang, D. Wu, C. L. Mak, K. H.

Wong, and N. -B. Ming, Materials Research Bulletin 37, 503 (2002).

[Rabe2007] K. M. Rabe, C. H. Ahn, and J. M. Triscone, Physics of Ferroelectrics:

A Modern Perspective, Springer, (2007).

[Ravel1998] B. Ravel, E. A. Stern, R. I. Vedrinskii, and V. Kraizman, Ferroelectrics 206, 407 (1998).

[Redhead1962] P.A. Redhead, Vacuum 12, 203 (1962).

[Sacha2006] G. M. Sacha, A. Verdaguer, and M. Salmeron, J. Phys. Chem. B 110, 14870 (2006).

[Sai2005] N. Sai, A. M. Kolpak, and A. M. Rappe, Phys. Rev. B 72, 020101 (2005).
[Shao2006] R. Shao, M. P. Nikiforov, and D. A. Bonnella, Appl. Phys. Lett. 89, 112904 (2006).

[Scales1992] J. A. Scales, M. L. Smith, and T. L. Fischer, J. Comput. Phys. 103, 258 (1992).

[Schlom2008] D. G. Schlom, L. -Q. Chen, X. Q. Pan, A. Schmehl, and M. A. Zurbuchen, J. Am. Ceram. Soc., 91, 2429 (2008).

[Schneider1998] B. Schneider, R. Niemann, C. Kuper, H. Hesse, and M. Neumann, J. Electron Spectrosc. Relat. Phenom. 96, 37 (1998).

[Shimada2010] T. Shimada, S. Tomoda, and T. Kitamura, Phys. Rev. B 81, 144116 (2010).

[Shin2008] J. Shin, V. Nascimento, A. Borisevich, E. Plummer, S. Kalinin, and A. Baddorf, Phys. Rev. B 77, 245437 (2008).

[Shin2009] J. Shin, V. B. Nascimento, G. Geneste, J. Rundgren, E. W. Plummer, B. Dkhil, S. V. Kalinin, and A. P. Baddorf, Nano. Lett. 9, 3720 (2009).

[Shirley1994] D. A. Shirley, Y. Zhang, B. L. Petersen, Z. Hussain, W. A. Huff, J. J. Barton, and L. J. Terminello, J. Electron Spectrosc. Relat. Phenom. 68, 49 (1994).

[Singh2008] P. Singh, B. J. Brandenburg, C. P. Sebastian, D. Kumar, and O. Parkash, Materials Research Bulletin 43, 2078 (2008).

[Smutek1975] M. Smutek, S. Cerny, and F. Buzek, Adv. Catal. 24, 343 (1975).

[Spanier2006] J. E. Spanier, A. M. Kolpak, J. J. Urban, I. Grinberg, L. Ouyang, W. S. Yun, A. M. Rappe, and H. Park, Nano Lett. 6, 735 (2006).

[Spivak1959] G. V. Spivak, and S. Zheludev, Kristallografiya 4, 115 (1959).

[Tanaka1998] K. Tanaka, O. Nakagawara, M. Nakano, T. Shimuta, H. Tabata, and T. Kawai, Jpn. J. Appl. Phys. 37, 6142 (1998).

[Tanner1976] B. K. Tanner, X-Ray Diffraction topography Oxford: Pergamonn Press, (1976).

[Tanuma1994] S. Tanuma, C. J. Powell, and D. R. Penn, Surf. Interface Anal. 21, 165 (1994).

[Tanuma2005] S. Tanuma, C. J. Powell, D. R. Penn, Surf. Interface Anal. 37, 1 (2005).

[Tanuma2011] S. Tanuma, C. J. Powell, D. R. Penn, Surf. Interface Anal. 43, 689 (2011).

[Telieps1985] W. Telieps, and E. Bauer, Ultramicroscopy 17, 57 (1985).

[Thiel1987] P.A. Thiel, and T.E. Madey, Surf. Sci. Rep. 7, 211 (1987).

[Tiwari2009] D. Tiwari, and S. Dunn, J. Mater. Sci. 44, 5063 (2009).

[Tromp2010] R. M. Tromp, J. B. Hannon, A. W. Ellis, W. Wan, A. Berghaus, and O. Schaff, Ultramicroscopy 110, 852 (2010).

[Turner1998] S. Turner, CERN Accelerator School: Synchrotron Radiation and Free Electron Lasers: proceedings (1998).

[VanHove1986] M. A. Van Hove, W. H. Weinberg, and C. -M. Chan, Low Energy Electron Diffraction: Experiment, Theory and Surface Structure Determination; Springer Series in Surface Sciences 6; Springer-Verlag: New York, (1986).

[VanHove1993] M. Van Hove, W. Moritz, H. Over, P. Rous, A. Wander, A. Barbieri, N. Materer, U. Starke, and G. Somorjai, Surf. Sci. Rep. 19, 191 (1993).

[VanUitert1968] L. G. Van Uitert, J. J. Rubin, and W. A. Bonner, IEEE J. Quantum

Electron. 4, 622 (1968).

[Vanacore2010] G. M. Vanacore, L. F. Zagonel, and N. Barrett, Surf. Sci. 604, 1674 (2010).

[Veeco] http://www.veeco.com.cn

[Verdaguer2006] A. Verdaguer, G. M. Sacha, H. Bluhm, and M. Salmeron, Chem. Rev. 106, 1478 (2006).

[Viana2007] M. L. Viana, R. Diez Muino, E. A. Soares, M. A. Van Hove, and V. E. de Carvalho, J. Phys.: Condens. Matter 19, 446002(2007).

[Vilquin2009] B. Vilquin, B. Gautier, A. Brugère, and J. S. Moulet, AIP Conf. Proc. 1173, 129 (2009).

[Vogt1982] H. Vogt, J. A. Sanjurjo, and G. Rossbroich, Phys. Rev. B 26, 5904 (1982).

[Wachtel2010] E. Wachtel, and I. Lubomirsky, Adv. Mater. 22, 2485 (2010).

[Wadati2009] H. Wadati, A. Maniwa, A. Chikamatsu, H. Kumigashira, M. Oshima, T. Mizokawa, A. Fujimori, and G. A. Sawatzky, Phys. Rev. B 80, 125107 (2009).

[Wagner1979] C. Wagner, W. Riggs, L. Davis, and J. Moulder, Handbook of X-Ray Photoelectron Spectroscopy, edited by G. Muilenberg (Perkin-Elmer Corporation, Eden Prairie, 1979).

[Wang2011] J. L. Wang, A. Pancotti, P. Jégou, G. Niu, B. Gautier, Y. Y. Mi, L. Tortech, S. Yin, B. Vilquin, and N. Barrett, Phys. Rev. B 84, 205426 (2011).

[Wang2012] J. L. Wang, F. Gaillard, A. Pancotti, B. Gautier, G. Niu, B. Vilquin, V. Pillard, G. L. M. P. Rodrigues, and N. Barrett, J. Phys. Chem. C 116, 21802 (2012).

[WangJ2012] J. L. Wang, B. Vilquin, and N. Barrett, Appl. Phys. Lett. 101, 092902

(2012).

[Wendt2005] S. Wendt, R. Schaub, J. Matthiesen, E.K. Vestergaard, E. Wahlström, M.D. Ramussen, P. Thostrup, L.M. Molina, E. Laegsgaard, I. Stensgaard, B. Hammer, and F. Besenbacher, Surf. Sci. 598 226 (2005).

[Wendt2006] S. Wendt, J. Matthiesen, R. Schaub, E.K. Vestergaard, E. Laegsgaard, F. Besenbacher, and B. Hammer, Phys. Rev. Lett. 96 066107 (2006).

[Winkelmann2008] A. Winkelmann, C. S. Fadley, and F. J. Garcia de Abajo, New J. Phys. 10, 113002 (2008).

[Wu2011] C. -L. Wu, P. -W. Lee, Y. -C. Chen, L. -Y. Chang, C. -H. Chen, C. -W. Liang, P. Yu, Q. He, R. Ramesh, and Y. -H. Chu, Phys. Rev. B 83, 020103 (2011).

[Yoo2003] Y. Z. Yoo, P. Ahmet, Z. Jin, K. Nakajima, T. Chikyow, M. Kawasaki, Y. Konishi, Y. Yonezawa, J. H. Song, and H. Koinuma, Appl. Phys. Lett. 82, 4125 (2003).

[Zhang2006] Q. Zhang, T. Cagin, and W. A. Goddard III, Proc. Natl. Acad. Sci. USA 103, 14695 (2006).

[Zhang2013] J. Zhang, G. Wang, F. Gao, C. Mao, F. Cao, and X. Dong, Ceramics

International 39, 1971 (2013).

[Zhao2008] M. H. Zhao, D. A. Bonnell, and J. M. Vohs, Surf. Sci. 602, 2849 (2008).

[Zhou1997] C. Zhou, and D. M. Newns, J. Appl. Phys. 82, 3081 (1997).

# Publications

**Peer-reviewed Journals:**

1. J. L. Wang, F. Gaillard, A. Pancotti, B. Gautier, G. Niu, B. Vilquin, V. Pillard, G. L. M. Rodrigues, and N. Barrett, "Chemistry and atomic distortion at the surface of an epitaxial $BaTiO_3$ thin film after dissociative adsorption of water" J. Phys. Chem. C 116, 21802 (2012).
2. J. L. Wang, B. Vilquin, and N. Barrett, "Screening of ferroelectric domains on $BaTiO_3$ (001) surface by ultraviolet photo-induced charge and dissociative water adsorption" Appl. Phys. Lett. 101, 092902 (2012) .
3. J. L. Wang, A. Pancotti, P. Jégou, G. Niu, B. Gautier, Y. Y. Mi, L. Tortech, S. Yin. B. Vilquin, and N. Barrett, "Ferroelectricity in a quasiamorphous ultrathin $BaTiO_3$ film" Phys. Rev. B 84, 205426 (2011).
4. A. Pancotti, J. L. Wang, P. Chen, L. Tortech, C. M. Teodorescu, and N. Barrett, "X-ray photoelectron diffraction study of relaxation and rumpling of ferroelectric domains in $BaTiO_3$ (001) " Phys. Rev. B 87, 184116 (2013).
5. N. Barrett, J. E. Rault, J. L. Wang, C. Mathieu, A. Locatelli, T. O. Mentes, M. A. Niño, S. Fusi, M. Bibes, A. Barthélémy, D. Sando, W. Ren, S. Prosandeev, L. Bellaiche, A. Petraru, I. Krug, and C. M. Schneider, "Full field electron spectromicroscopy applied to ferroelectric materials" J. Appl. Phys. 113, 187217 (2013).

**Under preparation:**

1. J. L. Wang, N. Barrett, B. Vilquin, and G. Dezanneau, "Surface atomic and chemical structure of $Sr_{0.67}Ba_{0.33}Nb_2O_6$ (001) single crystal"
2. J. L. Wang, N. Barrett, F. Gaillard, G. Niu, and B. Vilquin, "Dissociative adsorption of $H_2O$ on epitaxially strained, out-of-plane polarized, $BaTiO_3$ (001) thin films"
3. J. L. Wang, N. Barrett, G. Niu, and B. Vilquin, "Investigation on structural and ferroelectric properties of $BaTiO_3$ thin films grown by different $O_2$ plasma power"

**Conference Contributions:**

1. Jiale Wang, Alexandre Pancotti, Pascale Jegou, Gang Niu, Brice Gautier, Yanyu

Mi, Ludovic Tortech, Shi Yin, Bertrand Vilquin, and Nick Barrett, "Ferroelectricity in quasi-amorphous $BaTiO_3$ ultra-thin film" MRS2013, April 1-5, 2013 San Francisco, California, USA

2. Jiale Wang, Francois Gaillard, Alexandre Pancotti, Brice Gautier, Gang Niu, Bertrand Vilquin, Valerie Pillard, Gustavo Rodrigues, and Nick Barrett, "Chemistry and atomic distortion at the surface of an epitaxial $BaTiO_3$ thin film after dissociative adsorption of Water" MRS2013, April 1-5, 2013 San Francisco, California, USA
3. J. L. Wang, A. Pancotti, P. Jégou, G. Niu, B. Gautier, Y. Y. Mi, L. Tortech, S. Yin, B. Vilquin, and N. Barrett, "Ferroelectricity in Quasi-Amorphous $BaTiO_3$ Ultra-thin Film" ISAF-ECAPD-PFM 2012, July 9-13, Aveiro, Portugal
4. J. L. Wang, A. Pancotti, M. Alaaeddine, L. Tortech, B. Vilquin, and N. Barrett "Investigation of relaxation and rumpling of ferroelectric domains on $BaTiO_3$ (001) surface by LEED I-V and valence band XPD" ISAF-ECAPD-PFM 2012, July 9-13, Aveiro, Portugal
5. J. L. Wang, A. Pancotti, F. Gaillard, G. Niu, B. Vilquin, J. Leroy, and N. Barrett "Adsorption and dissociation of H2O on compressively strain $TiO_2$-terminated $BaTiO_3$ film" ISAF-ECAPD-PFM 2012, July 9-13, Aveiro, Portugal

**Honors:**

1. 2012 Chinese Government Award for Outstanding Self-financed Students Abroad
2. Best Poster Award 3rd Prize, International Symposium on Applications of Ferroelectrics - European Conference on the Applications of Polar Dielectrics - International Symposium Piezoresponse Force Microscopy and Nanoscale Phenomena in Polar Materials (ISAF-ECAPD-PFM) 2012
3. 2013 MRS Spring Meeting 'Best Poster' Nominees

# Acknowledgements

First and foremost, I am deeply grateful to my advisors Dr. Nick Barrett and Dr. Bertrand Vilquin, for their extremely valuable experience at XPS measurement and MBE oxide growth. Under their patient guidance, my work moves forward with progress all the time.

I am thankful to the defense committee members, Andrei Kholkin, Mario Maglione, Pascale Roy, Yves Dumont and William Sacks for their valuable suggestions and comments.

I am grateful to Dr. Alexandre Pancotti. With his kind help of LEED I-V and XPD simulation, I can make a quick progress for my research. From him I knew the kindness and friendliness of Brazilian people.

I want to thank Serge Palacin, head of the Service de Physique Chimie des Surfaces et Interfaces for giving me the opportunity to work 3 years here as a PhD student.

I would also like to thank Dr. Brice Gautier at INSA Lyon and Dr. François Gaillard at Université Lyon 1, for their generous collaboration and supports during my PhD work. I also thank Dr. Gang Niu who prepared the BTO films used during the thesis.

I am very grateful to Jocelyne Leroy and Bruno Delomez, two kind engineers in our group. When I need help, they are always beside me. Additionally, I want to thank Catherine Julien and Dominique Martinotti in SPCSI Service for their great helps and kindness during my Ph.D. in CEA.

I would like to thank furthermore all those that, not directly involved with my project, have always been available for discussion and help: Julien Rault, Claire Mathieu, Jelle Dionot, Ingo Krug, Shi Yin. Thanks to all my friends, as they share with me many happy moments during these years.

I want to acknowledge the financial support to my project from French National Research Agency (ANR) project Surf-FER, ANR-10-BLAN-1012, without which this work could not have been possible.

Finally, I thank my parents, Jinzhang Wang and Canhua Jiang, with their love and support to finish my Ph.D. thesis.

Jiale WANG

# Modifications of the chemical and electronic ferroelectric surface structure under water adsorption


## Résumé

Le principal objectif de notre recherche est de comprendre comment la polarisation ferroélectrique affecte la chimi/physisorption des molécules de $H_2O$ sur une surface ferroélectrique et comment cette adsorption peut en retour affecter la structure atomique et chimique de la surface, et ainsi des propriétés ferroélectriques. Ces connaissances peuvent être utiles pour mieux comprendre la photo-production d'hydrogène à la surface d'un ferroélectrique, afin d'améliorer la réaction de photolyse de l'eau, en favorisant la séparation électron-trou ainsi que la réactivité de surface. Nous avons tout d'abord étudié la structure atomique et chimique de la surface du matériau ferroélectrique $BaTiO_3$ (001) sous forme de couches minces épitaxiées et de monocristaux, avant et après des expositions contrôlées à l'eau. Le champ dépolarisant, produit par les discontinuités de surface, conduit à des modifications de la structure atomique, chimique et électronique. Nous avons ensuite démontré l'existence d'un film quasi-amorphe ultra-mince et ferroélectrique de $BaTiO_3$. Enfin, la structure de surface du ferroélectrique uniaxial $Sr_{0.67}Ba_{0.33}Nb_2O_6$ (001) a été caractérisée, constituant ainsi la première étape pour l'amélioration de la photolyse de l'eau.


Mots-clés : ferroélectricité, $BaTiO_3$, $Sr_{0.67}Ba_{0.33}Nb_2O_6$, chimisorption, quasi-amorphe, spectroscopie des photoélectrons stimulée par les rayons X


## Abstract

The main objective of our research is to understand how the ferroelectric polarization affects the chemi/physisorption of $H_2O$ molecules on a ferroelectric surface and how this adsorption may in return affect the chemical and the atomic surface structure and hence the ferroelectric properties. The acquired knowledge may be used to obtain a deeper understanding of light enhanced hydrogen production at a ferroelectric surface, to promote the water photolysis reaction, by favoring the electron-hole separation and the surface reactivity. We have first studied the surface atomic and chemical structure of the model ferroelectric $BaTiO_3$ (001) in the form of epitaxial thin films and single crystals before and after controlled exposure to water. The depolarizing field produced by the surface discontinuity leads to changes in the atomic, chemical and electronic structural changes and reordering. We have also demonstrated the existence of a ferroelectric, quasiamorphous, ultrathin $BaTiO_3$ film. Finally, the surface structure of the uniaxial ferroelectric $Sr_{0.67}Ba_{0.33}Nb_2O_6$ (001) has been characterized in a first step towards use for photolysis enhancement.


Keywords: ferroelectricity, $BaTiO_3$, $Sr_{0.67}Ba_{0.33}Nb_2O_6$, chemisorption, quasi-amorphous, X-ray photoelectron spectroscopy